

HI INTENSITY MAPPING AS A TEST FOR DARK ENERGY

A THESIS SUBMITTED TO THE UNIVERSITY OF MANCHESTER
FOR THE DEGREE OF MASTER OF PHILOSOPHY
IN THE FACULTY OF ENGINEERING AND PHYSICAL SCIENCES

2014

Kate Voller

School of Physics and Astronomy

Contents

Abstract	10
Declaration	11
Copyright Statement	12
Acknowledgements	14
1 Introduction	15
1.1 Dark Energy	15
1.1.1 Probing Dark Energy	17
1.1.2 Structure Growth	19
1.2 Baryonic Acoustic Oscillations	21
1.2.1 How BAOs Form	22
1.2.2 BAOs and the Dark Energy Equation of State	26
1.3 Using Hydrogen Intensity Mapping to Detect BAOs	27
1.3.1 How Intensity Mapping Works	28
1.3.2 HI Temperature Signal	30
1.4 Single Dish versus Interferometer	31
1.4.1 Optical versus Radio	34
1.5 This Thesis	35

2	Simulating the HI Sky	37
2.1	Extracting HI Signal	39
2.2	Generating Spectral Line Cubes	43
2.3	Foregrounds	44
2.3.1	Galactic Foregrounds	46
2.3.1.1	Synchrotron Emission	48
2.3.1.2	Extending the 408 MHz map	51
2.3.2	Extragalactic Foregrounds	53
2.3.2.1	Discrete Sources	53
2.3.2.2	Modelling Point Sources	54
2.3.3	Foregrounds Removal Methods	56
3	Radio Interferometry	60
3.1	Current HI Intensity Mapping Experiments	62
3.2	Interferometers of Interest	64
3.3	Simulating Interferometric Observations	70
3.3.1	Millennium Simulation Dirty Maps	72
4	Power Spectrum Estimation	77
4.1	Error on Power Spectrum	80
4.2	Binning Visibilities	81
4.2.1	Expected Power Spectrum and Variance	82
4.3	Testing the Incoherent Estimator	87
4.4	Bias Correction	92
4.5	Autocorrelation versus Cross Correlation	94
4.5.1	Autocorrelation	94
4.5.2	Cross Correlation	98

5	Measuring the HI Power Spectrum	105
5.1	Input Power Spectrum	106
5.2	Finding F_ℓ for the HI Angular Power Spectrum	107
5.3	Recovering the HI Angular Power Spectrum	109
5.3.1	Changing Bin Widths	111
5.3.2	Error Bar Estimation	113
5.4	Results for Tianlai, MeerKAT and ASKAP	116
5.4.1	Recovered HI Angular Power Spectrum	122
6	Conclusions and Future Work	133
6.1	Future Work	135
	Appendices	138
A	AIPS Tcl Script	138
B	21 cm Angular Power Spectrum	146

Word count

List of Tables

2.1	Foreground contributions	47
2.2	Foreground removal methods	58
3.1	Array properties	68
5.1	SNR values for dirty maps	117
5.2	Optimal number of pointings	131
5.3	Peak SNR values	131
B.1	List of variables.	150

List of Figures

1.1	Evolution of a baryonic acoustic oscillation.	23
1.2	Baryonic acoustic oscillation signatures	24
1.3	Sensitivity of power spectrum to cosmological parameters	26
2.1	Illustration of the construction of a mock observing cone from a chain of replicated boxes.	38
2.2	Relationship between maximal comoving distance and opening angle of observing cone.	39
2.3	Temperature versus frequency for Milli- and full Millennium simulation.	41
2.4	Temperature versus frequency for Millennium simulation (smaller beam size).	43
2.5	Millennium simulation FITS cube slices.	45
2.6	Millennium simulation FITS cube slices.	46
2.7	Power spectra of various foregrounds.	48
2.8	Haslam 408 MHz sky maps.	50
2.9	Haslam 408 MHz map before and after small scale fluctuations added.	52
2.10	Power spectra of 408 MHz map before and after small scale fluctuations added.	53
2.11	Point source count data.	55

2.12	Source counts	56
3.1	Dish Positions for Tianlai, MeerKAT and ASKAP.	66
3.2	UV-coverage for Tianlai, MeerKAT and ASKAP.	68
3.3	Histogram of baselines	69
3.4	Dirty maps for Tianlai, MeerKAT and ASKAP.	74
3.5	Dirty maps for Tianlai, MeerKAT and ASKAP.	75
3.6	Dirty maps for Tianlai, MeerKAT and ASKAP.	76
4.1	Comparing the effects of different Δu on the power spectrum.	85
4.2	Comparing power spectrum estimators for signal and noise inputs.	86
4.3	Input temperature maps used for testing.	88
4.4	Input temperature maps used for testing.	89
4.5	Recovered power spectra for various input maps.	90
4.6	Comparing UV maps.	91
4.7	UV map and recovered power spectra after correction has been applied.	92
4.8	Calculating F_ℓ	93
4.9	Recovered power spectra using Tianlai-like array including noise.	95
4.10	Recovered power spectra for Tianlai-like array reducing noise.	96
4.11	Recovered power spectra for Tianlai-like array reducing noise further.	97
4.12	Recovered power spectra for noise only using cross correlation estimator before averaging in uv cells.	100
4.13	Recovered power spectra for noise only using cross correlation estimator after averaging in uv cells.	101
4.14	Recovered power spectra for noise only using cross correlation estimator within ℓ bins.	102

4.15	Computed power spectra for constant T_ℓ^2 input using different estimators.	103
4.16	Constant T_ℓ^2 power spectrum corrected using F_ℓ with noise added.	104
5.1	HI power spectra.	107
5.2	HI power spectra computed using different estimators.	108
5.3	F_ℓ for HI power spectrum.	108
5.4	How HI power spectrum changes with frequency.	109
5.5	Recovered HI power spectra using cross correlation estimator, corrected with F_ℓ and including noise.	110
5.6	Recovered HI power spectrum using cross correlation estimator, corrected with F_ℓ and including noise.	111
5.7	Comparing the effect of bin width on the HI power spectrum.	112
5.8	Comparing bin width methods.	113
5.9	Histogram of visibilities.	114
5.10	Errors on the power spectrum with theoretical fit.	115
5.11	Errors on the power spectrum with theoretical fit corrected.	116
5.12	Dirty maps for Tianlai, MeerKAT and ASKAP	119
5.13	Dirty maps for Tianlai, MeerKAT and ASKAP	120
5.14	Dirty maps for Tianlai, MeerKAT and ASKAP	121
5.15	Recovered HI angular power spectra for Tianlai	122
5.16	Recovered HI angular power spectra for MeerKAT	123
5.17	Recovered HI angular power spectra for ASKAP	124
5.18	Recovered HI angular power spectra for Tianlai, including sample variance	125
5.19	Recovered HI angular power spectra for MeerKAT, including sample variance	126

5.20 Recovered HI angular power spectra for ASKAP, including sample variance	127
5.21 Optimal SNR values for Tianlai, MeerKAT and ASKAP	130
6.1 Foreground power spectrum	135

The University of Manchester

Kate Voller

Master of Philosophy

HI Intensity Mapping as a Test for Dark Energy

November 20, 2014

The purpose of this thesis is to find out how successfully intensity mapping can be used to measure the HI signal with upcoming interferometers. This technique is an alternative to mapping the galaxy distribution with optical redshift surveys, using the 21 cm neutral hydrogen line instead to trace the matter. It relies on detecting the combined emission from galaxies rather than being able to detect individual galaxies. In this thesis a bespoke intensity mapping instrument ‘Tianlai’ will be compared with two interferometers not specifically designed for this purpose, namely MeerKAT and ASKAP.

Several different power spectrum estimators are investigated, settling on a cross-correlation estimator. Despite needing a correction factor F_ℓ , this estimator has the lowest noise bias at high ℓ . A theoretical HI angular power spectrum is then used as the simulation input and the potential ability of each interferometer to recover the power spectrum is analysed.

We find that integrated HI signal is able to be detected by all three interferometers after 120 hours, with good detections being made after 1200 hours. At 800 MHz ($z \sim 0.8$) ideal ‘Tianlai’ and ASKAP instruments require 15 and 20 pointings while MeerKAT requires 125 pointings. This gives peak SNR values, after 120 hours, of 36 and 30 for ‘Tianlai’ and ASKAP and 20 for MeerKAT. Moving to higher frequencies ($z \sim 0.4$) these SNR values increase to 47, 36 and 23 for ‘Tianlai’, ASKAP and MeerKAT respectively. As the observation time is increased, the SNR values also increase for each instrument.

‘Tianlai’ performs best due to its many short baselines giving it improved sensitivity to the angular scales of interest. Although ASKAP and MeerKAT both have few short baselines, ASKAP’s PAFs give it a very large field-of-view, resulting in it out-performing MeerKAT and having similar potential to the bespoke instrument ‘Tianlai’.

We conclude that all three instruments would be able to make a very good detection of the integrated HI signal after 1200 hours in an ideal experiment so it would be possible to design intensity mapping experiments for all three interferometers.

Declaration

No portion of the work referred to in the thesis has been submitted in support of an application for another degree or qualification of this or any other university or other institute of learning.

Copyright Statement

- i. The author of this thesis (including any appendices and/or schedules to this thesis) owns certain copyright or related rights in it (the “Copyright”) and s/he has given The University of Manchester certain rights to use such Copyright, including for administrative purposes.
- ii. Copies of this thesis, either in full or in extracts and whether in hard or electronic copy, may be made **only** in accordance with the Copyright, Designs and Patents Act 1988 (as amended) and regulations issued under it or, where appropriate, in accordance with licensing agreements which the University has from time to time. This page must form part of any such copies made.
- iii. The ownership of certain Copyright, patents, designs, trade marks and other intellectual property (the “Intellectual Property”) and any reproductions of copyright works in the thesis, for example graphs and tables (“Reproductions”), which may be described in this thesis, may not be owned by the author and may be owned by third parties. Such Intellectual Property and Reproductions cannot and must not be made available for use without the prior written permission of the owner(s) of the relevant Intellectual Property and/or Reproductions.
- iv. Further information on the conditions under which disclosure, publication and commercialisation of this thesis, the Copyright and any Intellectual Property

and/or Reproductions described in it may take place is available in the University IP Policy (see <http://documents.manchester.ac.uk/DocuInfo.aspx?DocID=487>), in any relevant Thesis restriction declarations deposited in the University Library, The University Library's regulations (see <http://www.manchester.ac.uk/library/aboutus/regulations>) and in The University's Policy on Presentation of Theses.

Acknowledgements

I would like to thank my supervisor Richard Battye for his help throughout. Many thanks go to Clive Dickinson for constantly being around to answer questions and help with various problems. I would also like to thank Minh Huynh of the International Centre for Radio Astronomy Research for providing the ASKAP configuration files.

Chapter 1

Introduction

1.1 Dark Energy

For years cosmologists around the world have been building up a description of what is responsible for the accelerated expansion of the Universe (dark energy). So far we know that it accounts for approximately 3/4 of the total energy density, it does not seem to cluster, it causes space-time to stretch and must have a strong negative pressure (also known as gravitationally repulsive) in order to cause the acceleration (Huterer and Turner, 1999).

Dark energy can be thought of as the energy density of a vacuum as it is the energy associated with the continuous production and annihilation of particle-antiparticle pairs. This implies the dark energy density is constant in both space and time so has become synonymous with the cosmological constant, Λ , with $w = -1$, forming the standard model of cosmology, the Λ CDM model. Although the cosmological constant seems to fit much of the observational data well it has a few major problems.

One outstanding drawback is the fine-tuning problem which arises due to the

huge discrepancy between the size of the cosmological constant predicted by quantum field theory (QFT) and that inferred cosmologically. QFT predicts a cosmological constant which is 120 orders of magnitude larger than what is observed (Carroll and Press, 1992). A second problem is the coincidence problem which arises due to the fact that the time at which dark energy becomes dominant happens to be the time we live in. The fact that the density of dark energy and matter are coincidentally the same is strange since both densities evolve differently throughout the history of the Universe, implying the unlikely condition of an infinitesimally small initial ratio between the two. A final problem arises due to the inclusion of the cosmological constant in the standard model which gives rise to solutions which, at low matter densities, have regions of discontinuities (Oztaş and Smith, 2006).

In an attempt to solve these problems, quintessence models were developed which have an equation of state parameter $w > -1$ and can vary with time. w just greater than -1 means that the dark energy density slowly decreases as the universe expands. Radiation, pressureless matter and a quintessence scalar field, φ , are the main components of the quintessence models. In these models, it is the potential energy of the dynamic field φ which causes the accelerated expansion. The quintessence field is very light and unlike the cosmological constant, it can vary in both space and time. Over time, its average energy density and pressure slowly decay, a feature which can help solve the tuning problem and rapid beginning of cosmic acceleration (Caldwell et al., 1998; Steinhardt et al., 1999; Ferreira and Joyce, 1998). The field is required to be light in order that it does not clump together and begin to form structure like matter. Two main classes of quintessence models have been developed; the first uses the idea of tracker fields (Steinhardt et al., 1999) while the second is known as a scaling solution (Wetterich, 1988). The former works on the basis that the fields track the background density by

adapting their behaviour to match the scale factor, while the latter uses the idea that the energy density ratio ρ_φ/ρ_B remains constant, where ρ_B is the density of the background.

The equation of state parameter provides a simple phenomenological description of dark energy. The equation of state relates the density and pressure of a fluid and takes the form $w = p/\rho c^2$. Pressureless material or dust has $w = 0$, while radiation or relativistic particles have $w = 1/3$. By combining the results from 4 different data sets, tight constraints on w can be imposed. The results come from observations of high redshift type 1a supernovae, observations of the evolution of the galaxy cluster mass function with redshift, the *Wilkinson Microwave Anisotropy Probe* (*WMAP*) and baryonic acoustic oscillations. This data has allowed bounds to be placed on the equation of state parameter giving $w = -1 \pm 0.2$ (Turner and Huterer, 2007; Kowalski et al., 2008; Vikhlinin et al., 2009; Hicken et al., 2009).

In recent years baryonic acoustic oscillations (BAOs) have become of increasing interest to cosmologists as they provide a robust probe of dark energy. Dark energy in the recent Universe ($z < 1$) can be studied using weak lensing while supernovae can be used to study dark energy within redshifts $0 < z < 2$. BAOs have the advantage of being able to probe dark energy up to redshifts of $z \sim 3$, which is important in distinguishing between different dark energy models where accelerated expansion may have begun at different times.

1.1.1 Probing Dark Energy

It is a well established idea in cosmology that dark energy is the driving force behind the accelerating expansion of the Universe. The first evidence of dark energy came in 1998 from supernovae observations (Riess et al., 1998; Perlmutter et al., 1999) with further evidence being collected by many other studies e.g. Perlmutter

(2003); Kowalski et al. (2008). Data from the WMAP seven-year analysis estimates the Universe is composed of 73% dark energy, 23% dark matter and 4.6% baryonic matter. However, despite the dark energy density being measured to an accuracy of a few percent, (Frieman et al., 2008), and relatively tight limits on w now, little is known about the time evolution of w .

Dark energy affects the expansion rate, $H(z)$, where z is the redshift, however this quantity cannot be measured directly. Instead it must be inferred through its effects on structure growth. Once $H(z)$ is sufficiently constrained the following equation can be solved to determine the equation of state parameter, w ,

$$H^2(z) = H_0^2[\Omega_r(1+z)^4 + \Omega_m(1+z)^3 + \Omega_k(1+z)^2 + \Omega_{de}f(z)], \quad (1.1.1)$$

where H_0 is the Hubble constant, Ω (the dimensionless density parameter) represents the ratio of the mean observed density to that of a flat Universe with subscripts ‘r’, ‘m’, ‘k’ and ‘de’ representing radiation, matter, curvature and dark energy respectively. The function $f(z)$ is determined by solving the dark energy conservation of energy equation giving,

$$f(z) = \exp \left[3 \int_0^z [1 + w(z')] d \ln(1 + z') \right]. \quad (1.1.2)$$

If w is constant, as in the case for the cosmological constant, $f(z) = (1+z)^{3(1+w)}$. The nature of dark energy is contained within w , therefore precise measurements need to be made in order to distinguish between various dark energy models.

Since the Universe is expanding, it is not possible to measure proper distances as objects are constantly moving away from each other. Instead we use measures such as luminosity distance and angular diameter distance, both of which can be measured using standard candles and rulers. Standard candles and standard rulers are used to calibrate cosmic distances using objects with a known intrinsic

luminosity or length. Luminosity distance, d_L and angular diameter distance, d_A are given by

$$d_L(z) = (1+z)r(z), \quad (1.1.3)$$

$$d_A(z) = \frac{r(z)}{(1+z)}, \quad (1.1.4)$$

where $r(z)$ is the comoving distance given by

$$r(z) = c \int_0^z \frac{dz'}{H(z')}. \quad (1.1.5)$$

It is easy to see that measurements of d_L and d_A allow $H(z)$ to be determined, which can then be combined with equation 1.1.1 to determine w . Type 1a supernovae make very good standard candles while baryonic acoustic oscillations make good standard rulers (see chapter 1.2 later).

1.1.2 Structure Growth

Structures in the Universe originated from primordial density fluctuations at the time of inflation. Over time these fluctuations grew under gravity eventually forming the large scale structure that can be seen today. Since the initial fluctuations are small and the background is effectively smooth, linear Newtonian perturbation theory for a perfect fluid can be used to describe the evolution. By embedding the fluid in an expanding background with comoving coordinates $\mathbf{x} = a(t)\mathbf{r}$, where a is the scale factor and \mathbf{r} is the comoving position, the expansion of the Universe can be introduced. The growth equation governing the gravitational evolution of matter perturbations in a perfect fluid can be derived from the continuity, Euler and Poisson equations and expressed in terms of independent Fourier modes as

$$\ddot{\delta}_k + 2H\dot{\delta}_k = \delta_k \left(4\pi G\rho - \frac{c_s^2 k^2}{a^2} \right), \quad (1.1.6)$$

where $\delta_k = \delta\rho/\rho$ is the density contrast, dots denote derivatives with respect to time, $k = 2\pi/\lambda$ is the wavenumber of a particular Fourier mode and $c_s = \sqrt{\partial P/\partial\rho}$ is the sound speed, where P is the pressure of the fluid.

This growth equation can be interpreted as the balance between gravitational instability causing growth (first term on the right) and the restriction to growth by the fluid pressure (second term on the right). The cosmic expansion appears in the growth equation as a Hubble drag term (the second term on the left). This drag reduces exponential growth to power law growth, further opposing the growth of perturbations. As the cosmic expansion is directly affected by dark energy, its effect on structure growth is expected to be seen in this term.

The growth equation can be solved for various epochs with solutions for the radiation, matter and dark energy dominated epochs shown below

$$\delta_m \propto \begin{cases} \text{constant} & \text{radiation dominated,} \\ t^{2/3} \propto a & \text{matter dominated,} \\ \text{constant} & \text{dark energy dominated.} \end{cases} \quad (1.1.7)$$

It is therefore clear that dark energy ultimately forces an end to structure formation due to the cosmic expansion outweighing any gravitational instability. Predictions about how the form of the dark energy equation of state might affect the amount of large scale structure as a function of redshift can then be made. For example, a larger value of w for a given Ω_{de} decreases the rate at which structure grows and so requires larger initial perturbations throughout all redshifts to produce the same large scale structure seen today. Therefore measuring the amount of structure seen as a function of redshift and comparing results with different w models will allow the nature of dark energy to be investigated.

Weak gravitational lensing is also a good way to probe dark energy since information regarding the distance-redshift relation and growth of structure are provided. Other possible probes include counts of galaxies and clusters, the Alcock-Paczyński test applied to small scale galaxy correlations and the CMB, as described in Blake and Glazebrook, 2003.

1.2 Baryonic Acoustic Oscillations

Baryonic acoustic oscillations (BAOs) are features imprinted in the distribution of galaxies as a result of frozen sound waves present in the photon-baryon fluid before recombination at $z \sim 1100$. The young universe was much hotter and filled with hydrogen plasma. As the Universe expanded it cooled; once it had cooled sufficiently, protons and electrons formed neutral atoms and could no longer absorb thermal radiation. Photons therefore travelled freely through space rather than being scattered off the protons and electrons (a process known as decoupling), which left behind a pattern of acoustic peaks in the CMB anisotropies and a series of wiggles in the galaxy angular power spectrum (Eisenstein and Hu, 1988). Peaks in the correlation function occur at comoving distance $s \sim 105h^{-1}\text{Mpc}$, which is equivalent to peaks in the matter power spectrum at comoving wavenumbers $k = (n + 1/2)\pi/s$ for $n = 2, 4, \dots$. The position of these peaks is known to a precision of order 1%, making them reliable standard rulers (Ansari et al., 2008).

As the wavelength of the BAO spectral peak was imprinted at a particular comoving wavelength in the Universe, they have a fixed comoving angular size and so can be used as a standard ruler (Peterson et al., 2006). The value of the BAO wavelength (related to the sound horizon scale at recombination) depends on $H(z)$, Ω_m and Ω_b but not on the amount or nature of dark energy (Wyithe et al., 2007). Measurements of $H(z)$ and the angular diameter distance can therefore be

used to probe how dark energy varies with time.

1.2.1 How BAOs Form

To see how a BAO forms, consider a point-like initial overdensity. The overdensity is assumed to be adiabatic and present in all species (dark matter, baryons, photons and neutrinos). The neutrinos are non-interacting so play no part in the formation process. Since the baryons and photons are coupled at this time, the growing matter perturbation causes the photon perturbation to grow meaning the region is over-pressurized relative to its surroundings. In an attempt to equalise this, a spherical sound wave is driven outwards through the baryon-photon fluid. The dark matter perturbation is left to grow at the centre of the perturbation while the sound waves travels out at the speed of sound. When the baryons and photons decouple, the photons escape so the pressure and sound speed starts to drop. The wave stops once the pressure and sound speed reach zero leaving behind a matter overdensity in the centre surrounded by a baryon overdensity shell, where the surrounding shell is the BAO. Up until recombination, the wave was travelling at the speed of sound so its final radius is equal to the sound horizon scale at this epoch, ≈ 150 Mpc (Eisenstein et al., 2007). This evolution of a BAO can be seen in Fig. 1.1.

At late times galaxies form in the overdensities. As the universe evolves the BAOs are imprinted from the matter distribution to the galaxy distribution, so they can be measured today.

Fig. 1.2 shows the BAO signatures. The top plot shows a peak in the correlation function of galaxies, which is a measure of the degree of clustering in the spatial distribution of galaxies. The power spectrum is obtained by Fourier transforming the correlation function. This peak indicates that there is a 1% chance of finding galaxies within a particular comoving separation from each other.

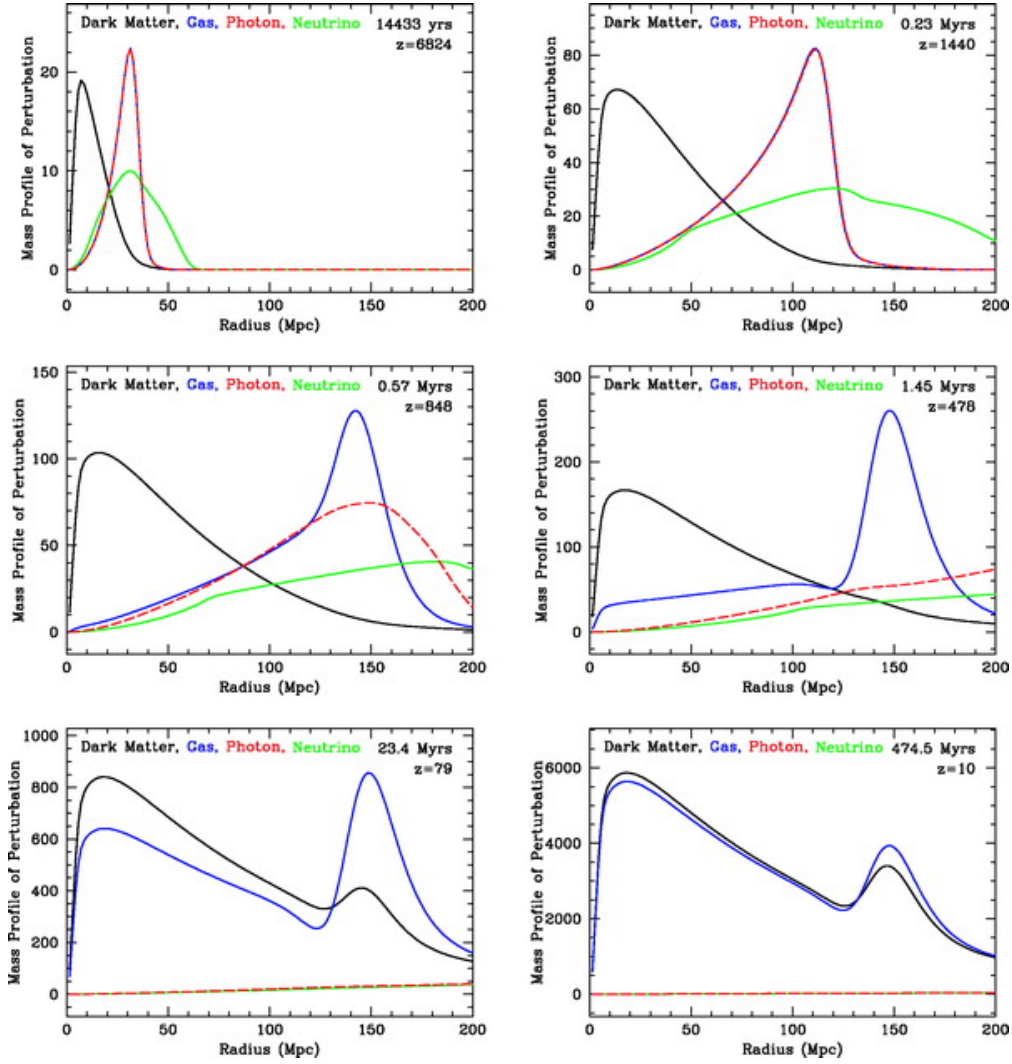


Figure 1.1: Snapshots of the evolution of the mass profile versus the radius of an initially point-like density perturbation located at the origin. Perturbations are fractional for that species and the perturbations for the relativistic species (photons and neutrinos) have been divided by $4/3$ so they are on the same scale. The black, blue, red and green lines correspond to CDM, baryons, photons and neutrinos respectively. Figure from Eisenstein et al. (2007)

The bottom plot of Fig. 1.2 shows the typical wiggles in the power spectrum. The power spectrum observed today contains information about what the Universe looks like and what has happened since last scattering. The features of the power spectrum can be easily explained in terms of cosmological parameters.

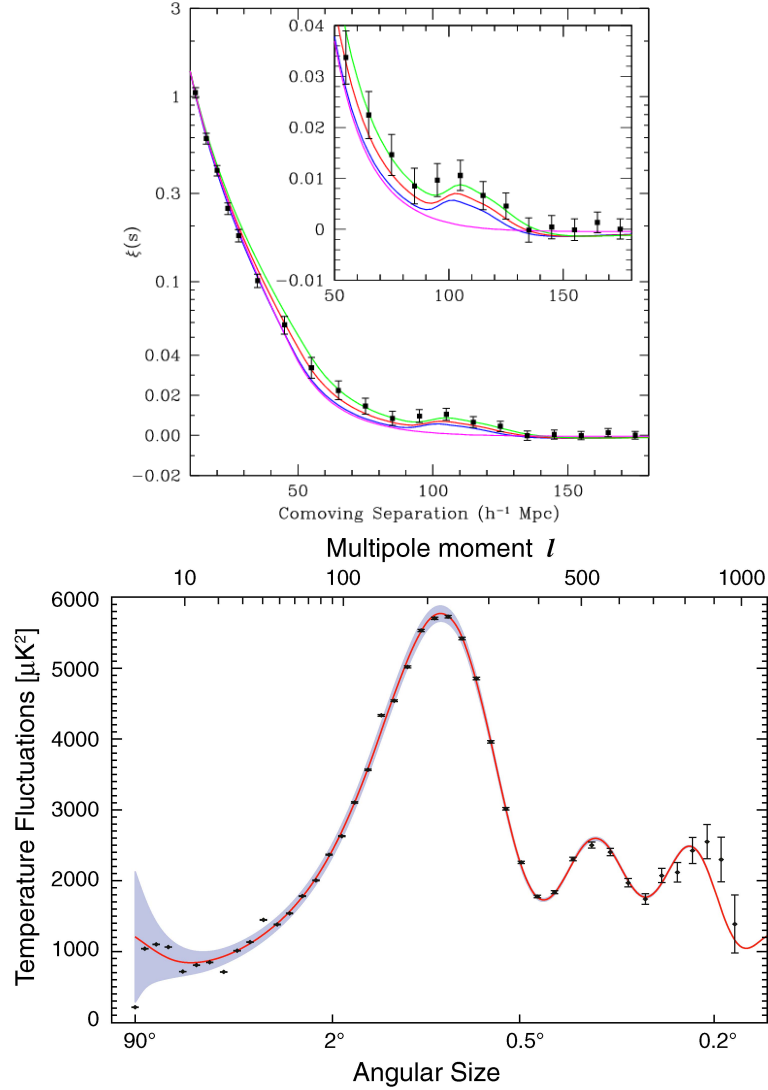


Figure 1.2: *The top plot shows the correlation function of galaxies for various cosmological models ($\Omega_m h^2 = 0.12, 0.13, 0.14$ for green, red and blue lines respectively) and the peak at $100 h^{-1} \text{ Mpc}$. The magenta line shows a pure CDM model ($\Omega_m h^2 = 0.105$) which lacks the acoustic peak (Eisenstein et al., 2005). The plot below shows the WMAP 5-year temperature angular power spectrum. Results from other experiments are also included. The red curve represents the best fit CDM model to the data. Figure from Freedman and Madore, 2010.*

The first peak, close to $\ell = 200$ is due to sound waves present at the time of last scattering. The physical scale of the acoustic mode is well understood, meaning

the angle we see only depends on the angular diameter distance to the surface of last scattering. The amount by which light rays converge or diverge determines the angular diameter distance. This means in a closed universe they will converge and give a larger apparent angle, while an open universe will have diverging rays and a smaller apparent angle. The geometry of the Universe can therefore be determined from the position of the first peak.

The second peak is smaller than the first peak and can be explained in terms of radiation pressure and massive baryons in a potential well. At the bottom of the well, the maximum compression achieved by the baryons depends on the radiation pressure and baryon mass. This will be larger for larger masses. The rarefaction does not depend on mass meaning that if all quantities were fixed but the baryon density was increased, the relative height of compression peaks (odd peaks) to rarefaction peaks (even) would increase. It is therefore possible to deduce the ratio of the baryon density to critical density using the ratio of the second to the first peak. More baryons also reduce the frequency of oscillations at all scales meaning that the first peak shifts to the right with a higher baryon mass.

Since the dark matter content of the Universe affects the way it expands, the shape of the power spectrum seen today will depend on the dark matter fraction. The amount of dark matter present affects the relative power of the even and odd peaks to each other. An increase in the amount of dark matter would decrease the power of the even peaks relative to the odd ones. The cosmological constant affects the position of the first peak so changing this value would shift the peak to the left or right.

Fig 1.3 illustrates how the power spectrum observed depends on the various cosmological parameters that have been discussed.

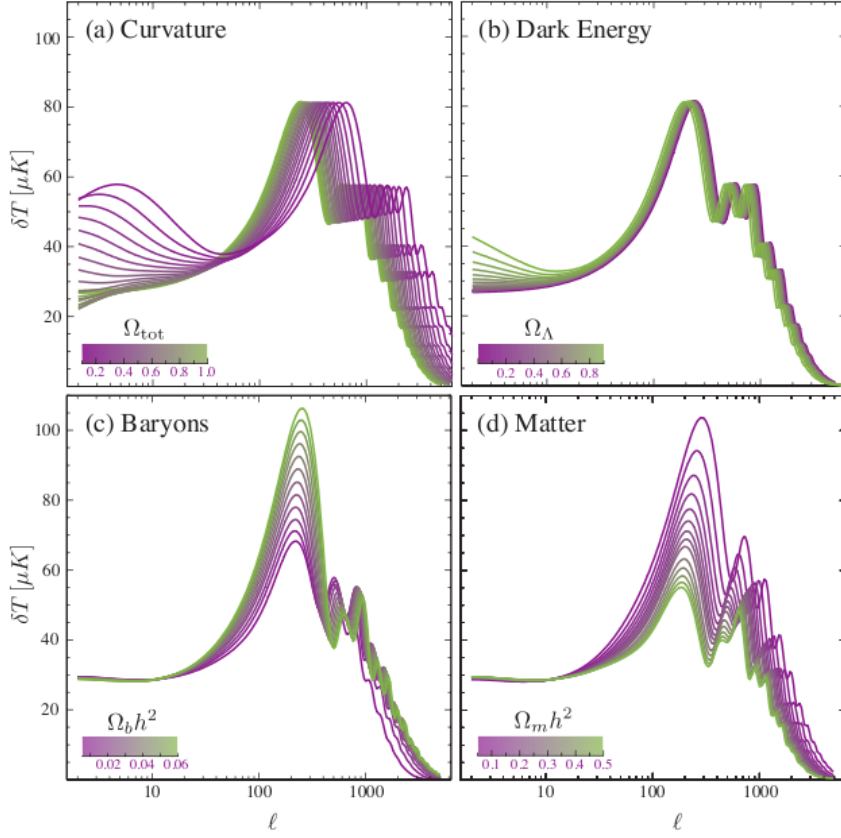


Figure 1.3: *Sensitivity of CMB angular power spectrum to 4 different cosmological parameters: curvature, dark energy, baryon density, matter density. Taken from <http://background.uchicago.edu/~whu/araa/node15.html>*

1.2.2 BAOs and the Dark Energy Equation of State

BAOs are usually detected in galaxy clustering and by mapping their 3D distribution in space the BAO scale can be found from the galaxy angular power spectrum, where the power spectrum describes the amplitude of galaxy density fluctuations as a function of angular separation. Measuring the BAO scale as a function of redshift allows two useful parameters to be found. Measurement of the angular scale of acoustic oscillations (i.e. apparent BAO size transverse to the line of sight) allows the angular diameter distance, d_A , to be determined at a particular redshift. Measurement of the redshift scale of acoustic oscillations (i.e. apparent BAO size

parallel to the line of sight) allows the Hubble parameter, $H(z)$, to be measured which gives an indication of how much the BAO have grown since recombination (Wyithe et al., 2007).

Angular diameter distance, d_A , and Hubble parameter, $H(z)$, can be written respectively as

$$d_A(z) = \frac{r_{\perp}}{(1+z)\Delta\theta}, \quad (1.2.1)$$

$$H(z) = \frac{c\Delta z}{r_{\parallel}}, \quad (1.2.2)$$

where $\Delta\theta$ and Δz are the BAO scale transverse to and along the line of sight and r_{\perp} and r_{\parallel} are the initial size of the oscillations (~ 150 Mpc) transverse to and along the line of sight. With sufficient measurements of the angular diameter distance and the Hubble parameter, the observed values can be compared with theoretical values for different cosmological models, thus constraining w .

1.3 Using Hydrogen Intensity Mapping to Detect BAOs

Previously, detections of the BAO signal have used photometry or spectroscopy in optical surveys to measure the clustering signal of large numbers of individual galaxies (Cole et al., 2005; Eisenstein et al., 2005; Huetsi, 2006). This technique required large observation times, high resolution and many corrections to data to account for problems such as extinction. Hydrogen intensity mapping has been proposed as a new, fast method to detect the BAO signal (Battye et al., 2004; Peterson et al., 2006; Chang et al., 2008; Loeb and Wyithe, 2008).

Optical galaxy surveys assume galaxies trace the underlying matter distribution, which can then be used to map the 3D matter distribution. It is clear that the more galaxies surveyed, the better the representation of the underlying matter

will be as there will be less shot noise. A major limiting factor is therefore the number of galaxies that a particular instrument is able to detect. At high redshift the volume of the universe being surveyed increases but the number of galaxies per unit volume decreases as the majority become too faint to detect. Flux limited photometric surveys mean there is a cutoff beyond which galaxies are hard to detect. This will obviously limit the accuracy to which BAOs can be detected, motivating the need for new techniques.

In order to obtain a measurement of the large scale structure (LSS) power spectrum with small enough uncertainties (cosmic and sample variance) a large volume of the universe should be sampled (typically a few Gpc). Large survey depths ($\Delta z \geq 1$) are also required as constraints on dark energy parameters can only be obtained when distance measurements are compared with dark energy models as a function of redshift. Being able to map the matter distribution without having to detect large numbers of individual galaxies would be highly beneficial, and this leads on to the idea of intensity mapping.

1.3.1 How Intensity Mapping Works

The idea is that intensity mapping will be able to detect the BAO signal of the combined emission of galaxies. This gets rid of the need for high resolution and long survey times, which are the main drawbacks for optical surveys. Neutral hydrogen (HI) is chosen as a suitable tracer of matter as the majority of HI resides in galaxies and its 21 cm transition line is the dominant spectral line at frequencies less than 1420 MHz (Pritchard and Loeb, 2011).

The 21 cm line of hydrogen arises from the hyperfine splitting of the 1s ground state due to the interaction between the magnetic moments of the proton and the electron. The resulting two energy levels are separated by $\Delta E = 5.9 \times 10^{-6}$ eV, corresponding to a wavelength of 21.1 cm and a frequency of 1420 MHz. The 21 cm

line produced from gas during the first billion years after the Big Bang redshifts to radio frequencies 30-200 MHz which is particularly appealing for new generation interferometers. New instruments are being built to detect the radio fluctuations in the 21 cm background resulting from variations in the amount of neutral hydrogen. The density field is traced by the 21 cm signal, giving information about the early Universe in the form of a power spectrum (Pritchard and Loeb, 2011).

This transition is ideal for 3D surveying as not only is it an isolated transition, but the observed frequency of a source can be directly translated into a redshift (Ansari et al., 2011),

$$z(\nu) = \frac{\nu_{21} - \nu}{\nu}; \quad \nu(z) = \frac{\nu_{21}}{(1+z)}, \quad (1.3.1)$$

$$z(\lambda) = \frac{\lambda - \lambda_{21}}{\lambda_{21}}; \quad \lambda(z) = \lambda_{21}(1+z). \quad (1.3.2)$$

Using HI emission means only the variation in HI mass on large scales needs to be measured rather than individual galaxies. Above the third BAO peak, non linear evolution washes out the BAO structure completely meaning that the third peak represents a minimum spatial scale that needs to be considered. The third peak has a wavelength of $35h^{-1}$ Mpc, so a Nyquist sampled map needs a pixel size of $18h^{-1}$ Mpc which, at $z = 1.5$, corresponds to an angular wavelength of 20 arcminutes. This would require a telescope of ~ 100 m to resolve (Chang et al., 2008). Intensity mapping is cheaper and requires less time to map large volumes of the sky than optical surveys, as well as having the added benefit of operating at lower resolutions. Intensity mapping provides a useful tool for studying large scale structure at a variety of redshifts; the pre-ionization and reionization epoch are being mapped at high redshift ($z > 6$) along with BAO studies at low redshift.

1.3.2 HI Temperature Signal

Assuming the density parameter of HI, Ω_{HI} , is known, the average brightness temperature of the 21 cm signal can easily be calculated using (Pritchard and Loeb, 2008; Barkana and Loeb, 2007)

$$T_{\text{b}} = 0.3 \left(\frac{\Omega_{\text{HI}}}{10^{-3}} \right) \left(\frac{\Omega_{\text{m}} + a^3 \Omega_{\Lambda}}{0.29} \right)^{-1/2} \left(\frac{1+z}{2.5} \right)^{1/2} \text{ mK}, \quad (1.3.3)$$

where Ω_{m} and Ω_{Λ} are the matter and dark energy density parameters respectively. The average sky brightness temperature due to the 21 cm signal $T_{\text{b}}(z \sim 1.5) = 330 \mu\text{K}$ which is three orders of magnitude smaller than the brightness of extragalactic radio source emission, $T_{\text{rs}} \sim 0.3 \text{ K}$ (Ansari et al., 2008). However, as we shall see later, these radio sources, along with emission from the CMB and Milky Way, have smooth frequency distributions allowing them to be removed, in theory.

Non-uniformities in the distribution of matter result in fluctuations of the signal about a mean value. Since the BAO signal is measured via the galaxy clustering, most sky observations are of the variations of the HI temperature, given by

$$\Delta T_{\text{b}} \sim T_{\text{b}} \delta, \quad (1.3.4)$$

where $1 + \delta = \rho_{\text{g}}/\bar{\rho}_{\text{g}}$ is the normalised neutral gas density (Chang et al., 2008). As these fluctuations are expected to be linearly related to the fluctuations in matter, the two power spectra are related,

$$P_{\text{HI}}(k) = b^2 P_{\text{m}}(k), \quad (1.3.5)$$

where the HI power spectrum is given by the Fourier transform of the brightness temperature

$$P_{\text{HI}}(k) = |\hat{T}(k)|^2. \quad (1.3.6)$$

Variations of the 21 cm brightness temperature in the cosmic web on $18h^{-1}$ Mpc scales give rise to sky noise of the order $150 \mu\text{K}$. Since the large-scale structure fluctuations are much larger than the fluctuations due to BAO, observations of the sky should cover as large an area as possible in order that the BAO signal is detected above the noise. In order to achieve large redshift domains, radio instruments need a large field of view (field of view $\geq 10 \text{ deg}^2$) and a large bandwidth ($\Delta\nu \geq 100 \text{ MHz}$) (Ansari et al., 2011). The sensitivity limit, S_{lim} , of a single dish radio instrument of collecting area, A , and system temperature, T_{sys} is given by

$$S_{\text{lim}} = \frac{\sqrt{2}k_{\text{B}}T_{\text{sys}}}{A\sqrt{t_{\text{int}}\Delta\nu}}, \quad (1.3.7)$$

where t_{int} is the total integration time and $\Delta\nu$ is the detection frequency bandwidth. When detection limits are compared with the expected 21 cm brightness of compact sources, S_{21} , given by (see for example Ansari et al. (2011))

$$S_{21} \simeq 0.021\mu\text{Jy} \frac{M_{\text{HI}}}{M_{\odot}} \times \left(\frac{1\text{Mpc}}{d_L(z)}\right)^2 \times \frac{200\text{kms}^{-1}}{\sigma_{\nu}}(1+z), \quad (1.3.8)$$

it was found that instruments would require a collecting area of 10^6 m^2 in order to detect sources with HI mass of $10^{10} M_{\odot}$ at $z = 1$.

1.4 Single Dish versus Interferometer

Intensity mapping can be done using both single dish telescopes and interferometers. The differences between using these methods will be looked at briefly, providing the motivation for choosing interferometers for the work done in this thesis.

The diffraction limited angular resolution for a telescope of diameter D can be

written as

$$\theta \sim \frac{\lambda}{D}, \quad (1.4.1)$$

where it is clear that increasing the size of the aperture improves the angular resolution. For a single dish, θ is limited by the dish size while the resolution of an interferometer is determined by its longest baseline (distance between components), meaning much higher resolutions can be achieved.

Interferometers are more stable than single dish telescopes because they measure the correlation of signal between pairs of receivers. Over long periods of time, uncorrelated signals average down to zero. This means that interferometers are basically immune to fluctuations in the receiver gain and noise whereas single dishes can be strongly affected by instrumental fluctuations (Emerson, 2002). Interferometers are also blind to the CMB background as they do not measure DC signal, which is a big advantage over single dish experiments.

The synthesized beam and window function are both known to a high degree of accuracy when using an interferometer as they are determined by the uv coverage (which is known exactly) and the Fourier transform of the primary beam (also known) respectively. Finally since an interferometer measures the observed visibilities, a direct measurement of the power spectrum is made (related to the square of the visibilities), see section 3 later for more details.

Interferometers do have some disadvantages, however, when compared to single dish telescopes. Firstly, when measuring extended sources, we are interested in the surface brightness sensitivity not the point source sensitivity. We have seen (see eqn. 1.3.7) that the point source sensitivity of a single dish radio instrument is set by its system temperature. This is the temperature equivalent to the total noise from many contributions including the atmosphere, CMB, antenna temperature

and receiver noise temperature. For an interferometer this equation becomes

$$S_{\text{lim}} = \frac{\sqrt{2}k_{\text{B}}T_{\text{sys}}}{A\sqrt{N(N-1)}\sqrt{t_{\text{int}}\Delta\nu}}, \quad (1.4.2)$$

where N is the number of antennas. As N increases, $\sqrt{N(N-1)} \rightarrow N$ meaning that the point source sensitivity of an interferometer tends towards that of a single dish with the same total area as N antennas.

The brightness temperature sensitivity depends on the beam solid angle given by $\Omega \propto 1/D^2$ for a single dish of diameter D and $\Omega \propto 1/b^2$ for an interferometer with longest baseline b . The beam solid angle is therefore smaller for an interferometer by $(D/b)^2$. The filling factor is given by

$$f = N \left(\frac{D}{b} \right)^2, \quad (1.4.3)$$

which is related to the brightness temperature by

$$T_b = \frac{fS\lambda^2}{2k_{\text{B}}\Omega}. \quad (1.4.4)$$

For single dishes, $f \approx 1$ which is the best that can be achieved highlighting the point that it is the filling factor that is important, not the size of the dishes. Interferometers trade brightness sensitivity for better resolution.

Another major drawback is that it is very difficult to measure the large angular scales with an interferometer which are measured by the shortest baselines. If the baselines are too short then shadowing occurs making scales larger than the primary beam very difficult to measure. Interferometers are typically more expensive to build than single dishes due to the cost of the correlation electronics. Despite this, the benefits of using interferometers to observe the HI signal outweigh the few negatives and so interferometers shall be used for this thesis work.

1.4.1 Optical versus Radio

Optical and radio wavelengths can be used to perform all sky galaxy surveys, each with its own advantages and disadvantages, which will be looked at briefly. The optical spectra of galaxies contains much more information than the radio spectra. The optical spectra contains both absorption features and strong emission lines, including Ly α and H α (Abdalla et al., 2009). In contrast, the radio spectrum is relatively featureless with the only strong line being the 21 cm line. Although being a prominent feature, the HI signal is very weak so detections of BAOs have mainly focussed on using the optical part of the spectrum with spectroscopy or photometry.

As a result of the weak signal in the radio, large survey volumes are needed. A ground based radio telescope with a large field of view will be able to cover most of the sky area in relatively short times (Seo et al., 2010). This is because radio telescopes rapidly increase their survey speed as the field of view increases. The time needed to detect HI galaxies, t_{map} , follows the relation

$$t_{\text{map}} \propto \left(\frac{A_{\text{eff}}}{T_{\text{sys}}} \right)^2 \text{FOV}, \quad (1.4.5)$$

compared to $1/t_{\text{map}} \propto A_{\text{eff}}\text{FOV}$ for optical telescopes (Abdalla et al., 2009). Future radio surveys will have $\text{FOV} \propto 100 \text{ deg}^2$ which is much larger than that achievable with optical surveys.

Equation 1.4.1 shows that typically the diffraction limited resolution of a radio telescope is not as good as that of an optical telescope. However, as shown above, interferometers are used to improve the resolution. Radio interferometers with a maximum baseline about 100 m give $\theta \sim 15 \text{ arcmin}$ (comoving scale about $10h^{-1} \text{ Mpc}$) at $z \sim 1$. Most baselines would be about half as long, corresponding to scales twice as large which is sufficient to observe the BAO peaks in the power

spectrum (Chen, 2012).

Foreground sources, especially Galactic synchrotron, remain the main disadvantage to radio surveys as they strongly contaminate the HI signal. Despite this, the different tracers used in optical surveys (luminous galaxies) and radio surveys (neutral hydrogen) mean that new radio surveys should produce results that compliment those from optical surveys.

1.5 This Thesis

The dark energy problem has been outlined previously in this Chapter along with a popular new method, intensity mapping, that aims to help solve the problem.

Chapter 2 describes how to simulate various signals in the sky. The first part describes how the HI signal is simulated and extracted from a catalogue of galaxies. The Milli-Millennium and full Millennium simulations are compared. Methods used to construct spectral line cubes to be used in simulations will also be discussed. The second part of Chapter 2 looks briefly at the problem of foregrounds with synchrotron emission and point sources are looked at in a bit more detail. Basic simulations of both these foreground sources are discussed along with some popular methods of removing foregrounds.

Chapter 3 describes the principles of radio interferometry. Some proposed HI intensity mapping experiments are described briefly before looking at some other proposed interferometers, namely Tianlai, MeerKAT and ASKAP, in more detail. The process of simulating interferometric observations is described and the Millennium simulation is used as a preliminary comparison of the performance of the three interferometers.

Chapter 4 explains how we are going to estimate the power spectrum from our simulated data. There are several power spectrum estimators that can be used

and these are investigated. Test simulations are done using noise only inputs, and some simple power law inputs before choosing the optimal method to be used in the rest of the thesis.

Chapter 5 describes the HI power spectrum that we will be using in our simulations. Using the power spectrum estimator found in Chapter 4 we shall attempt to recover the HI power spectrum and detect BAOs. The performance of the three interferometers described in Chapter 3 will be compared and an optimal survey strategy will be presented.

Chapter 6 summarises the main conclusions of this thesis and suggests some further work.

Chapter 2

Simulating the HI Sky

Obreschkow et al. (2009) present a simulation of 21 cm emission using a galaxy catalogue based on the Millennium simulation. The sky field has a comoving diameter of $500h^{-1}$ Mpc, which is large enough to probe cosmic structure. The overall simulation is made up of four steps in order to progress from the evolution of cosmic structure to a simulation of the static sky.

The first step produced a catalogue of $\sim 3 \times 10^7$ evolving galaxies and was made up of three individual simulation layers: *(i)* simulation of the dark matter evolution; *(ii)* semi-analytic evolution of galaxy evolution of the dark matter skeleton; and *(iii)* splitting the neutral hydrogen mass associated with each galaxy into HI and H₂ via post-processing.

The second step involved transforming the simulation box into an observation cone. Firstly, a chain of replicated simulation boxes was built along the line of sight (see Fig. 2.1). These boxes were then populated with galaxies chosen from the simulation box based on the lookback time seen by the observer. The simulation used 64 discrete time steps so each galaxy in the simulation is described by the properties at the closest timestep available. This will define spherical shells of identical cosmic time, represented as dashed lines in Fig. 2.1. An observing cone

was extracted from the chain of boxes, represented as the shaded region in Fig. 2.1.

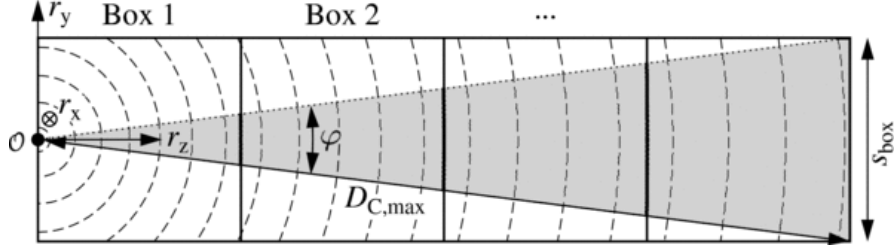


Figure 2.1: A schematic illustration of the construction of a mock observing cone (shaded region) from a chain of replicated simulation boxes (solid squares). The observer, \mathcal{O} , is surrounded by spherical shells containing galaxies from the same time step, indicated by dashed lines. $D_{C,max}$ is the maximal comoving distance and φ is the cone opening angle. Figure from Obreschkow et al. (2009).

From Fig. 2.1 it is clear that the cone opening angle, φ , is given by

$$\varphi = 2 \arcsin \frac{s_{\text{box}}}{D_{C,max}}, \quad (2.0.1)$$

where s_{box} is the comoving side of the simulation box and $D_{C,max}$ is the maximal comoving distance. The relationship between φ , s_{box} and z_{max} is shown in Fig. 2.2 where the cosmological parameters of the Millennium simulation have been used, along with three different box lengths. For the Millennium simulation $s_{\text{box}} = 500 \text{ h}^{-1} \text{ Mpc}$ (solid line), while the Milli-Millennium simulation has a box length of $s_{\text{box}} = 62.5 \text{ h}^{-1} \text{ Mpc}$ (dashed line). The Horizon- 4π simulation is a dark matter simulation with 10 times less mass resolution than the Millennium simulation (Obreschkow et al., 2009) and $s_{\text{box}} = 2 \text{ h}^{-1} \text{ Gpc}$ (dot-dashed line).

The remaining two steps in simulating 21 cm emission involved converting the HI mass into HI-line luminosities using the well known relation (Obreschkow et al., 2009),

$$\frac{L_{\text{HI}}}{L_{\odot}} = 6.27 \times 10^{-9} \frac{M_{\text{HI}}}{M_{\odot}}, \quad (2.0.2)$$

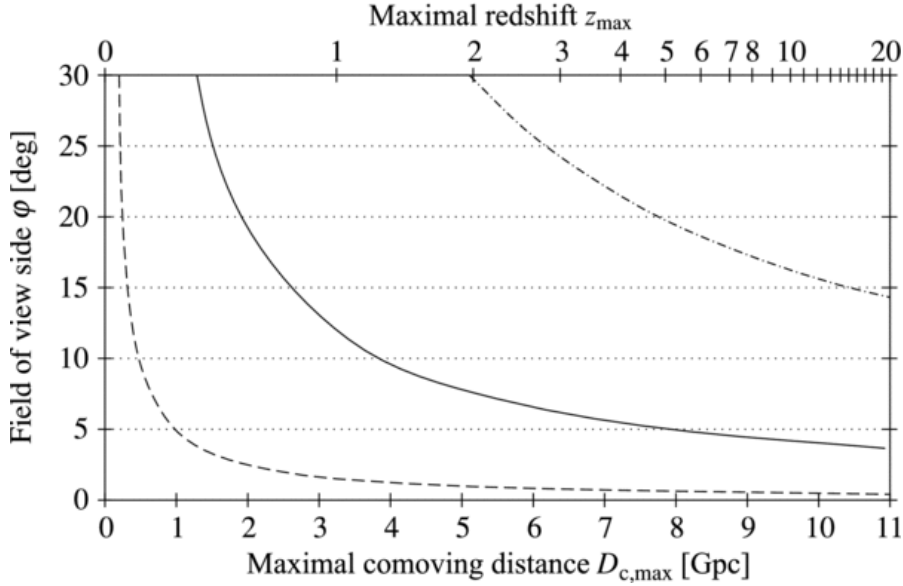


Figure 2.2: Relationship between the maximal comoving distance or maximal redshift and the opening angle of the observing cone. Different lines correspond to the box sizes of the Millennium (solid), Milli-Millennium (dashed) and the Horizon- 4π (dash-dotted) Simulations. Taken from Obreschkow et al. (2009).

and finally characterizing each line with a profile. This can then be analysed to predict characteristics of the HI signal.

2.1 Extracting HI Signal

The mean HI brightness temperature can be calculated using eq. 1.3.3, but for BAO surveys the fluctuations about the mean are of interest. A FORTRAN code was written to extract the HI signal as it would be observed by a telescope beam. Both the Milli- and full Millennium simulations were used initially and compared, with the full Millennium simulation being chosen for further work.

The full Millennium simulation was the largest simulation of its kind, using more than 10 billion particles to trace the evolution of the matter distribution in

the universe¹. The region simulated is over 2 billion light years across, contained in a cube of sides $500h^{-1}$ Mpc. The Milli-Millennium simulation has a volume 1/512 that of the full simulation.

The basic idea of the code is to read in galaxy properties from a simulation catalogue, namely position coordinates, redshift, HI mass, integrated HI flux and HI line width. It was then possible to calculate the HI temperature from each galaxy in a range Δf observed by a telescope with beam full-width half max θ_{FWHM} using

$$S = \frac{2k_{\text{B}}T}{\lambda^2}\Omega_{\text{pix}}, \quad (2.1.1)$$

where S is the flux density, λ is the wavelength, T is brightness the temperature and Ω_{pix} is the pixel area, given by $\theta_{\text{FWHM}} \times \theta_{\text{FWHM}}$. The signal was binned in frequency and plotted as temperature vs. frequency with the analytical formula for calculating the temperature was also been plotted for comparison. Fig. 2.3 shows the temperature fluctuations for the Milli- and full Millennium simulations using $\theta_{\text{FWHM}} = 1^\circ$ and $\Delta f = 10$ MHz.

Fig. 2.3 illustrates that generally the temperature calculated using the flux density follows that of the analytic formula. At low frequencies the temperature seems to fall away sharply from the theoretical curve which is an artefact of the observing cone (see Fig. 2.1). If the cone is extrapolated beyond the last simulation box, the box size is no longer sufficient to fill the cone. This results in a lack of galaxies at the edge of the cone, and this loss of galaxies causes a drop off in the signal at high redshift (low frequency). The maximal available redshift before galaxies start being lost is therefore determined by the opening angle of the observing cone, illustrated by Fig. 2.2.

At high frequencies Fig. 2.3 shows that temperature fluctuations are much larger as a result of shot noise. Shot noise is the error that occurs when observing

¹<http://www.mpa-garching.mpg.de/galform/virgo/millennium/>

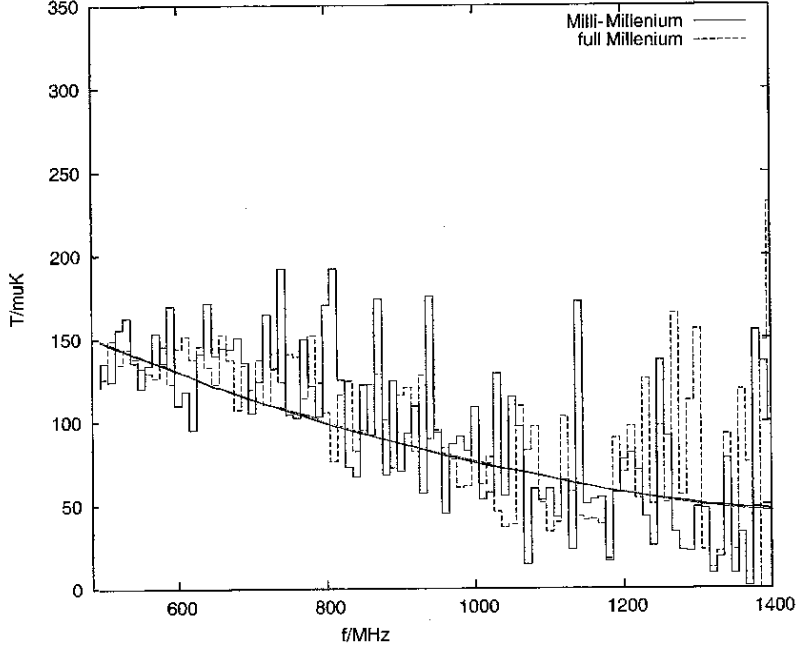


Figure 2.3: *Temperature against frequency for Milli- and full Millennium simulations with $\theta_{\text{FWHM}} = 1^\circ$ and $\Delta f = 10 \text{ MHz}$ with theoretical average signal curve for comparison.*

an incomplete view of the Universe. The comoving sky volume per unit solid angle decreases with decreasing redshift. This means that fewer galaxies are contributing so high frequencies are not a good representation of how the overall universe behaves. With such a low number of galaxies contributing to the HI signal, the bin-to-bin fluctuation in temperature is large. At lower frequencies the universe is represented better as more galaxies are contributing as the number of galaxies per bin is high.

Fig. 2.3 shows that generally both simulations follow the same trend. At low frequencies there are fewer fluctuations in the full simulation compared to the Milli-Millennium simulation. This means there is less shot noise as the survey volume was bigger so more galaxies will be contributing.

Both the telescope resolution and frequency bin size are variables in the code

so it is possible to investigate what effect they have on the HI signal. Instead of having a large θ_{FWHM} to make up the required area of sky, smaller pixels can be used and built up to make the total larger area. For example a 6×6 box with each pixel having a beam FWHM of $1/6$ deg would give a total of 1 deg^2 . This was achieved by reading in the catalogue as before but changing the centre position of the beam and cycling through all the pixels, gradually building up the area of sky.

Although studying a 1 deg^2 patch of sky is interesting because it allows general trends to be seen, it is more useful to look at larger areas of the sky as this will give a better picture of the properties of the universe as a whole and can be used to look for HI signals later.

Using 12×12 pixels with individual pixels $1/3 \text{ deg} \times 1/3 \text{ deg}$ gives a total area of 16 deg^2 . The results are illustrated in Fig. 2.4.

The main difference between Fig. 2.4 and Fig. 2.3 is that the fluctuations are smaller throughout the frequency range because of the larger field of view. By building up a series of smaller pixels, overall a larger portion of the sky is being looked at and so the HI temperature signal is closer to the mean value.

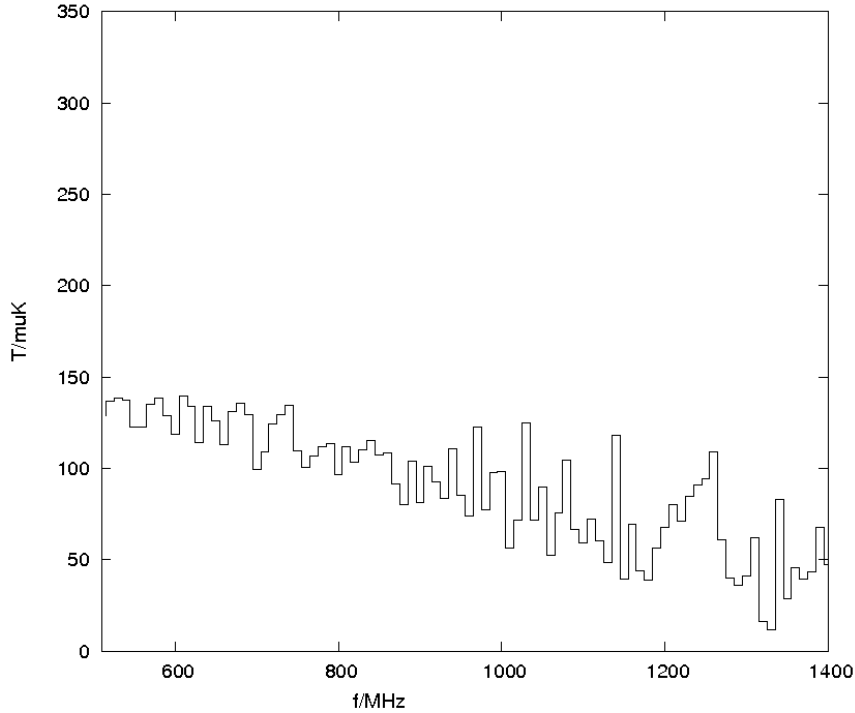


Figure 2.4: *Temperature as a function of frequency for the full Millennium simulation using a 12×12 box with a beam size of $1/3$ deg (total sky area of 16 deg^2) and bin size of 10 MHz.*

2.2 Generating Spectral Line Cubes

The main goal is to compute the power spectrum of HI. In order to do this, a FITS cube containing the HI signal was made. The cube is made up of two spatial dimensions and one in frequency. The FITS format was chosen as it is the preferred astronomical data format for storing images and spectra. In order to construct the cube, a catalogue of galaxies was read in from the full Millennium simulation from which it was possible to calculate the temperature as a function of frequency using the method described previously. At $z = 1.5$ the third BAO peak has an angular size of approximately 20 arcminutes (Chang et al., 2008). We therefore need a higher resolution than this so as to detect the peaks sufficiently. Since we are only interested in the combined emission of galaxies rather than detecting individual

galaxies we eliminate the need for very high resolution. For the purpose of this work we chose $\theta_{\text{FWHM}} = 5'$ and $\Delta f = 1$ MHz. Our patch of sky is therefore made up of 48×48 pixels with each pixel $5' \times 5'$ giving a total area of 16 deg^2 . The cube was then rescaled so that each side is comprised of 2^n pixels to help with FFTs later (see section 3.3). The cube was resized from 48×48 to 256×256 pixels by re-binning the galaxies, giving a new pixel size of $1/64 \times 1/64 \text{ deg}^2 = 56.25'' \times 56.25''$ and $\Delta f = 5$ MHz. To obtain different channel widths, the galaxies were re-binned in the frequency direction.

Figs. 2.5 and 2.6 show slices from FITS cubes at a variety of frequencies using two different channel widths ($\Delta f = 5$ MHz and $\Delta f = 50$ MHz), based on the full Millennium simulation as described above. At the very high frequencies galaxies can be seen clearly but there is no large scale structure visible. As the slices get further away (lower frequencies) the large scale structure in HI starts to become more prominent, until individual galaxies cannot be seen and the large scale structure dominates the image. These cubes will be used as the input to simulations done later in (see section 3.3).

2.3 Foregrounds

The observed sky brightness temperature, T_{sky} consists of several components and can be written as

$$T_{\text{sky}}(\nu, \theta, \phi) = T_{\text{CMB}}(\nu, \theta, \phi) + T_{\text{Gal}}(\nu, \theta, \phi) + T_{\text{ERS}}(\nu, \theta, \phi) + T_{\text{HI}}(\nu, \theta, \phi), \quad (2.3.1)$$

where T_{CMB} is the cosmic microwave background, T_{Gal} is our Galaxy's emission, T_{ERS} is extragalactic emission from radio sources and T_{HI} is the 21 cm signal to be detected. In the above notation ν denotes frequency dependence and θ, ϕ denote dependence in space. Although radio telescopes have the sensitivity to

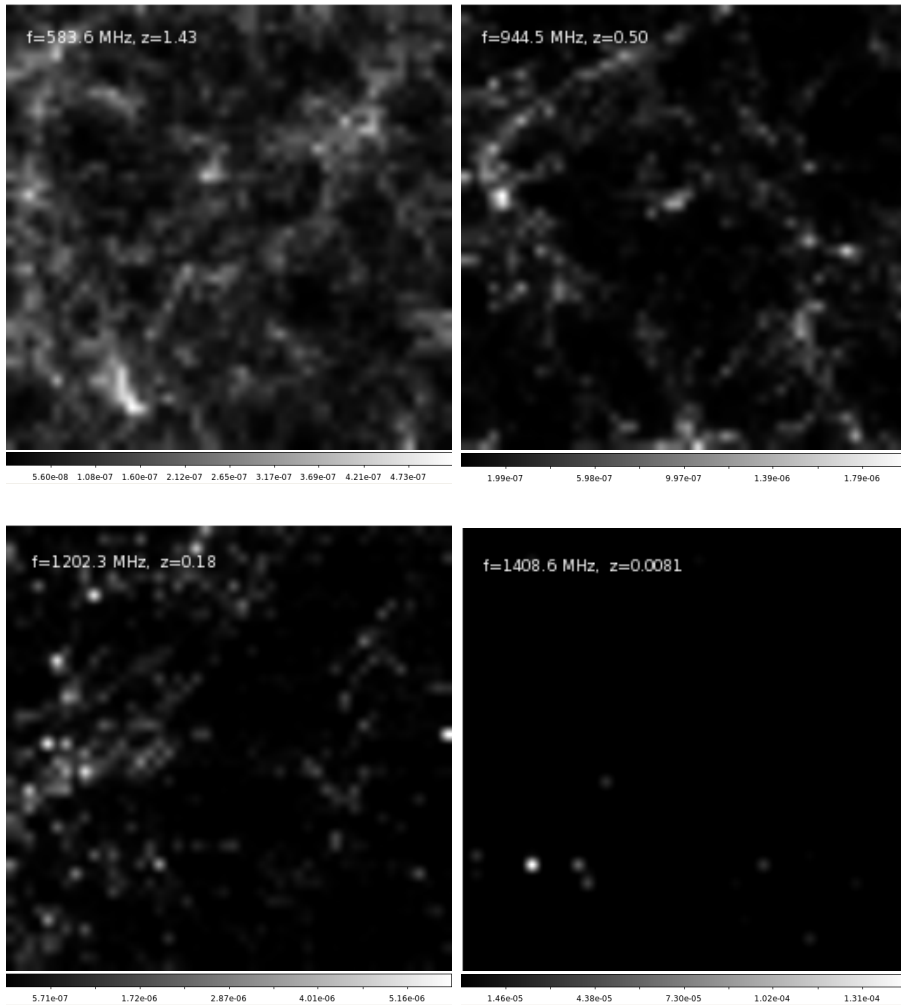


Figure 2.5: *Slices from the FITS cube made from the full Millennium simulation using $\Delta f = 5$ MHz at different frequencies: $f = 583.6$ MHz, 944.5 MHz, 1202.3 MHz and 1408.6 MHz. The images shown are a 4×4 deg² area of sky with the scale representing Jy/pixel.*

detect a BAO signal, in reality the 21 cm signal is swamped by foregrounds which can reach brightness temperatures larger than the 21 cm signal by 4 orders of magnitude (McQuinn et al., 2006). At $f = 1$ GHz, the foreground contribution is ~ 5 K while the 21 cm brightness temperature is ~ 0.1 mK (Battye et al., 2013).

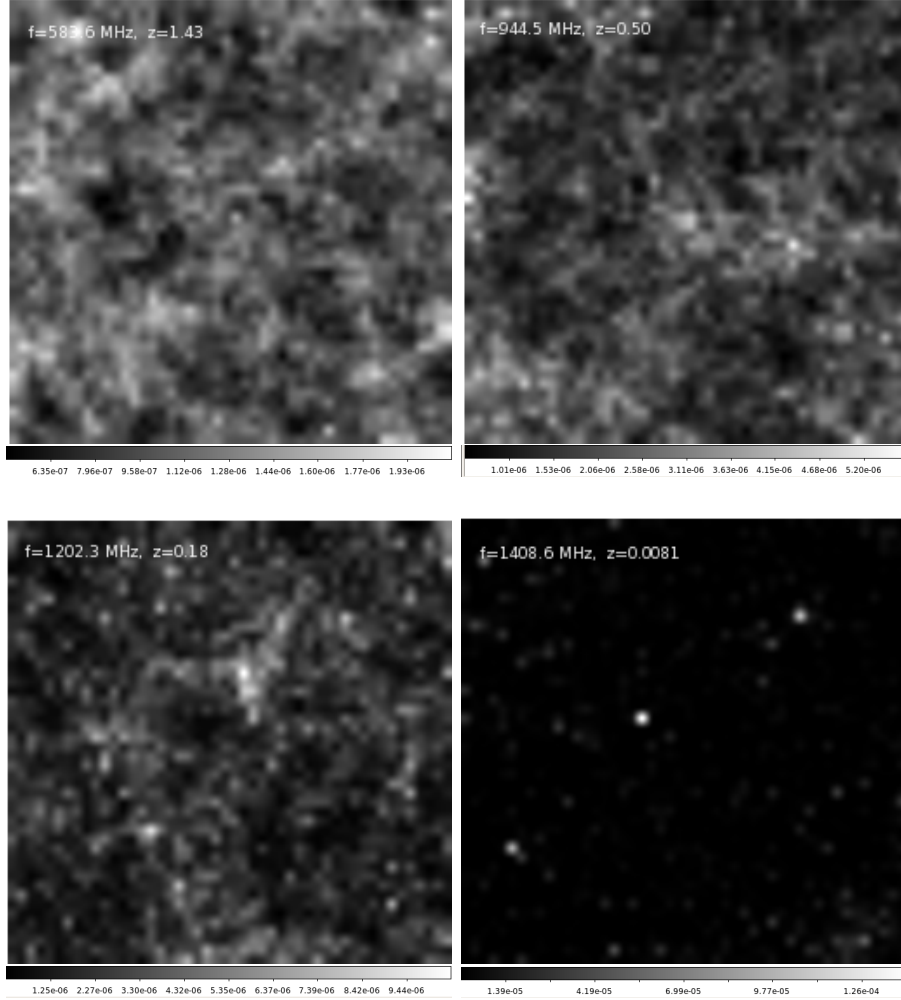


Figure 2.6: Slices from the FITS cube made from the full Millennium simulation using $\Delta f = 50 \text{ MHz}$ at different frequencies: $f = 583.6 \text{ MHz}$, 944.5 MHz , 1202.3 MHz and 1408.6 MHz . The images shown are a $4 \times 4 \text{ deg}^2$ area of sky with the scale representing Jy/pixel .

2.3.1 Galactic Foregrounds

The Milky Way’s ISM consists of cold atomic and molecular clouds, a warm and partially ionised inter-cloud medium and a hot ionised medium. Cosmic rays and magnetic fields also make up part of the ISM, which is where diffuse Galactic emission comes from. This Galactic emission can be divided into different components

Foreground	\bar{T} [mK]	δT [mK]
Synchrotron	1700	67
Free-free	5.0	0.25
Radio sources (Poisson)	-	5.5
Radio sources (clustered)	-	47.6
Extragalactic sources (total)	205	48
CMB	2726	0.07
Thermal dust	-	$\sim 2 \times 10^{-6}$
Spinning dust	-	$\sim 2^{-3}$
RRL	0.05	3×10^{-3}
Total foregrounds	~ 4600	~ 82
HI	~ 0.1	~ 0.1

Table 2.1: *Summary of foreground contributions, estimated by Battye et al. (2013). Estimates were made at 1 GHz for an angular scale of $\sim 1^\circ$ using a 10° wide strip at declination 45° and Galactic latitudes $< 30^\circ$.*

depending on the emission process: synchrotron radiation as a result of relativistic electrons travelling through the magnetic field; free-free emission resulting from the interacting of free electrons charged nuclei in warm ionised medium; thermal emission from warm interstellar dust; spinning dust emission from rotating dust grains; and line emission from atoms and molecules. The diffuse emission decreases with Galactic latitude as most of it is concentrated in the Galactic plane.

Each foreground contribution can be decomposed into a smooth component, \bar{T} , and a fluctuation, δT . A summary of the main foregrounds for HI intensity mapping and the size of their contribution is given in Table 2.1.

The intensity of the Galactic foregrounds reaches a minimum around 70 GHz where there is a complex superposition of the various emission components, shown in Fig. 2.7.

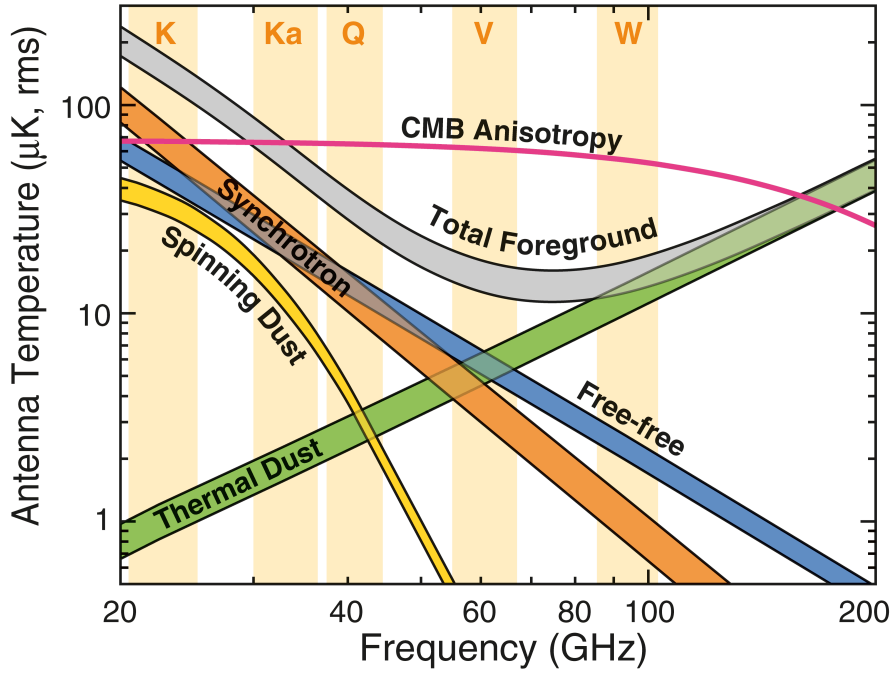


Figure 2.7: *Power spectra of diffuse Galactic foreground contributions over a range of frequencies. Taken from Bennett et al. (2013)*

2.3.1.1 Synchrotron Emission

We have seen that at the low frequencies that are relevant to BAO intensity mapping surveys ($\lesssim 10$ GHz), Galactic foregrounds are dominated by synchrotron emission (Wang et al., 2010).

The strength of the magnetic field perpendicular to the line of sight (B_{\perp}) and the cosmic ray electron density (n_e) determine the intensity of the synchrotron emission. Assuming the cosmic ray distribution follows a power law, $N(E) \propto E^{-s}$, the intensity of synchrotron emission at frequency ν can be written as

$$S(\nu) = \epsilon_s(\nu) \int_z n_e B_{\perp}^{(1+s)/2} dz, \quad (2.3.2)$$

A power law describing the synchrotron intensity can be written as

$$S(\nu) = S(\nu_0) \left(\frac{\nu}{\nu_0} \right)^{\beta_s}, \quad (2.3.3)$$

where

$$\beta_s = -(s + 3)/2. \quad (2.3.4)$$

A typical value for the cosmic ray spectrum $s = 3$, gives $\beta_s = -3$.

It has been shown that inhomogeneous spatial distributions in the magnetic field causes synchrotron emission to display visible substructures in the total intensity map (e.g. Gaensler et al. (2001)). These features are much smaller than those of the BAO meaning that the 3D 21 cm intensity signal should still stand out once it has been subtracted.

Although the synchrotron spectrum is relatively smooth, the synchrotron sources are not distributed uniformly and the slope can vary from source to source. The amplitude of the 21 cm signal is exceeded by the pixel-to-pixel variation in sky brightness by a factor of 1000.

To date, the most reliable estimate of the full-sky Galactic synchrotron emission is the 408 MHz all-sky survey of Haslam et al. (1982). At frequencies this low, the Galactic diffuse emission is dominated by synchrotron emission. The original map has been reprojected on a HEALPix grid in Galactic coordinates with $N_{\text{side}} = 512$. A Fourier filtering technique has also been applied to suppress residual stripes and point sources. This map can be obtained from the LAMBDA website² and is shown in Fig. 2.8.

The angular resolution of the 408 MHz map is 0.85° , which is worse than the angular resolution of any interferometer that we will be using to simulate observations (see Section 3.2 later). It is therefore necessary to superimpose artificial

²<http://lambda.gsfc.nasa.gov/>

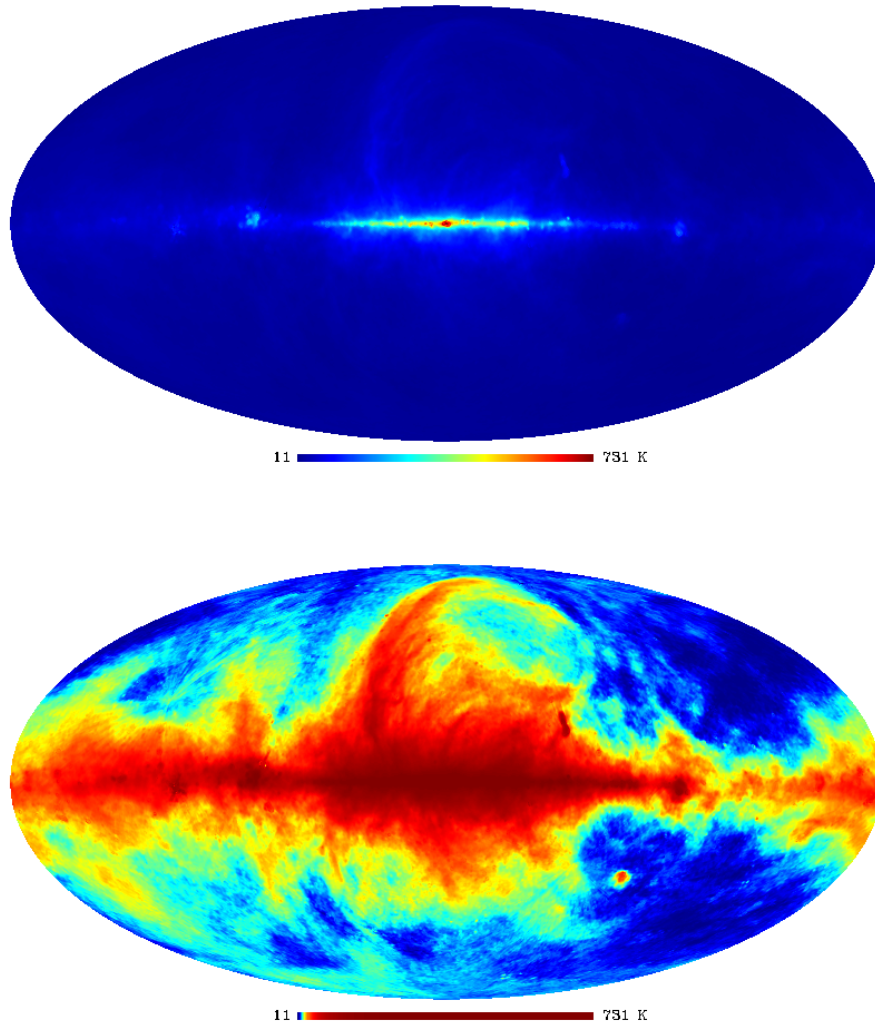


Figure 2.8: *Mollweide projection of the Haslam et al. (1982) template map at 408 MHz, in Galactic coordinates, used to model the synchrotron intensity. The top map uses a linear colour scale while the bottom has been histogram equalised.*

fluctuations at small angular scales on the original map. This will then provide a realistic image of the total synchrotron emission across the sky at 408 MHz up to the degree scale and an estimate of what it looks like at the smaller scales.

2.3.1.2 Extending the 408 MHz map

The method by which small scale fluctuations are added is described in Miville-Deschênes et al. (2007) and Delabrouille et al. (2012) and is similar to the technique used by Giardino et al. (2002). Firstly a Gaussian random field is generated at the correct N_{side} with the following power spectrum;

$$C_\ell = \ell^\gamma [\exp^{-\ell^2 \sigma_{\text{sim}}^2}] - C_\ell^{\text{tem}}, \quad (2.3.5)$$

where σ_{sim} is the resolution in radians of the simulation, C_ℓ^{tem} is the power spectrum of the template map with resolution $\sigma_{\text{tem}} = 56'$, and $\gamma = -2.7$. The Gaussian random field, G_{ss} , is then normalised by the rms and the average is subtracted so that fluctuations which are a fractional amount of the original are being added. To modulate small-scale fluctuations by large scale intensity the template map is exponentiated to the power β as shown in the following equation;

$$I'_{\text{tem}} = I_{\text{tem}} + \alpha G_{\text{ss}} I_{\text{tem}}^\beta, \quad (2.3.6)$$

where the PSM values $\alpha = 0.05$ and $\beta = 1.0$ were chosen (see Delabrouille et al. (2012)). This ensures that the power spectra of the small scales being added and the large scales in the template are continuous with each other.

The small scale fluctuation sky map is then added to the 408 MHz map to produce the final extended map. To see the effects of adding the small scale fluctuations, identical sections of each map can be looked at more closely and the differences seen in Fig. 2.9. It is clear that the large scales have been preserved while fluctuations at small scales can be seen in the right plot.

Fig. 2.10 shows the comparison between the power spectra before and after the map has been extended. It can be seen that the drop off in the original 408

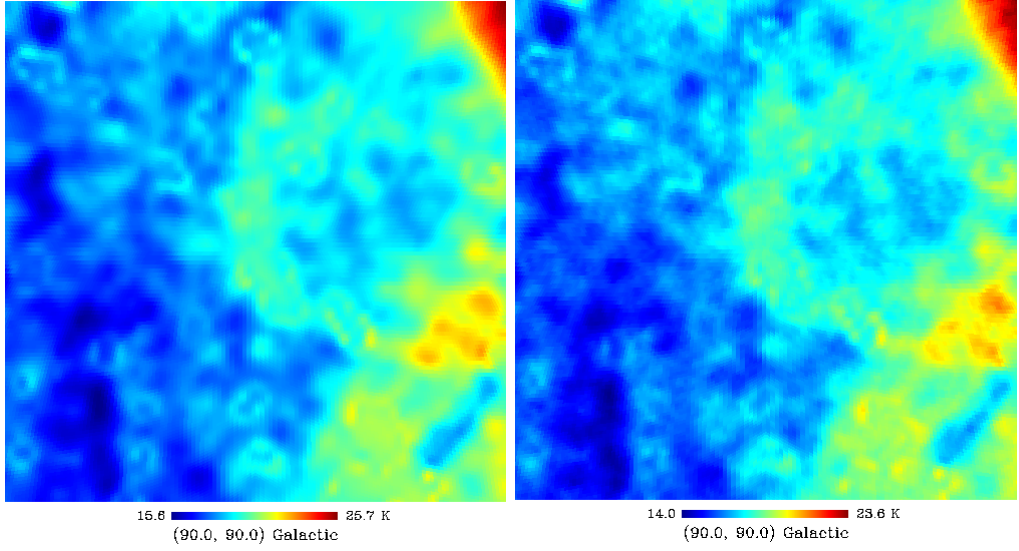


Figure 2.9: *Left hand panel shows a section of the original Haslam 408 MHz map and the right hand panel shows the same section but with small scales structure added.*

MHz power spectrum as a result of the beam has been corrected by the addition of fluctuations on small angular scales, described by eq. 2.3.5.

By extrapolating the 408 MHz map the synchrotron emission can be estimated at any frequency using,

$$T_{\nu}^{\text{Gsyn}}(\mathbf{r}) = T_{408}^{\text{Gsyn}}(\mathbf{r}) \left(\frac{\nu}{408 \text{ MHz}} \right)^{\beta_s(\mathbf{r})}. \quad (2.3.7)$$

It is clear from eq 2.3.7 that the extrapolation of the 408 MHz map relies on estimates of the spectral index. As this can vary both spatially and with frequency, there are a range of different models which can be implemented.

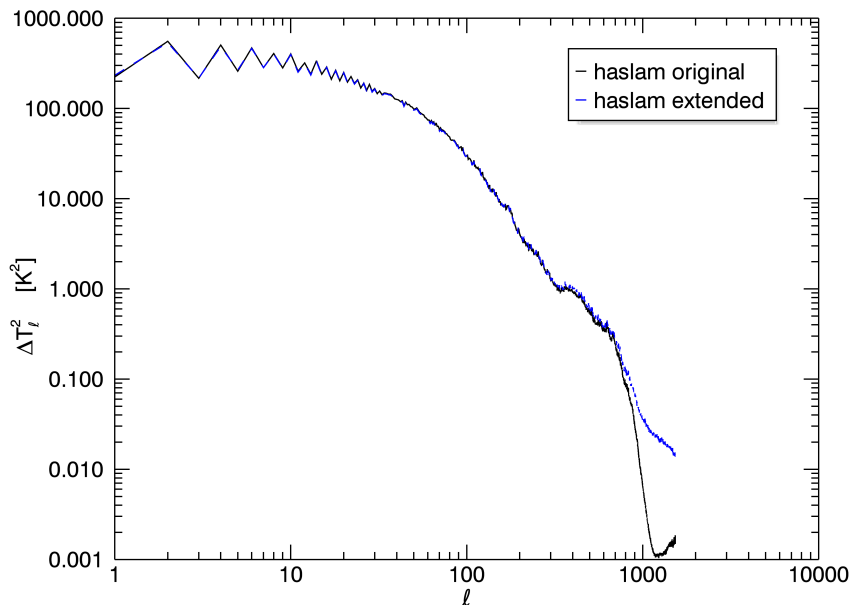


Figure 2.10: Plot showing the power spectra of the original 408 MHz Haslam map (solid black line) and the extended 408 MHz map with small scale fluctuations added (dashed black line)

2.3.2 Extragalactic Foregrounds

2.3.2.1 Discrete Sources

Discrete sources consist of radio galaxies, quasars and other objects that manifest themselves as point sources and contribute to the foreground. Contributions to point source foregrounds come from randomly (Poisson) distributed sources and clustered sources. Clustered sources have a non-trivial two-point correlation function while Poisson sources are uncorrelated. Many compilations of source counts have been done over the past decade (e.g. Fomalont et al., 2002; Bondi et al., 2003; Hopkins et al., 2003; Prandoni et al., 2006) and the effect these sources have on observations can be predicted by modelling their differential source count, dN/dS (number of sources per steradian per unit flux). The source counts are usually

Euclidean-normalised, meaning they are divided by the count one would expect in a static Euclidean universe, i.e. $dN/dS \propto S^{-2.5}$, (Vernstrom et al., 2011).

A variety of different fits to the source count data have been tried including a third order polynomial in $\log S$ by Katgert et al. (1988), a sixth order polynomial in $\log S$ by Hopkins et al. (2003), a simple power law in $\log S$ by Gervasi et al. (2008) and a fifth order polynomial in $\log S$ by Vernstrom et al. (2011). Although polynomials may be a simpler method of fitting than other functions, they remain a good choice as they are still able to fit distinctive features in the data. For example in Fig. 2.11 at low flux densities the source count flattens out, with a possible upturn at very low flux densities. Vernstrom et al. (2011) found that a fifth order polynomial was of high enough order to account for all the features in the data while higher orders just lead to unnecessary extra parameters and no significant improvement in the χ^2 so this will be used for the remainder of the section. The polynomial can be written as

$$\log \left(\frac{S^{2.5} dN/dS}{N_0} \right) = \sum_{i=0}^5 a_i \left[\log \left(\frac{S}{S_0} \right) \right]^i, \quad (2.3.8)$$

where $a_0 = 2.593$, $a_1 = 0.093$, $a_2 = -0.0004$, $a_3 = 0.249$, $a_4 = 0.090$, $a_5 = 0.009$, $N_0 = 1 \text{ Jy sr}^{-1}$ and $S_0 = 1 \text{ Jy}$.

2.3.2.2 Modelling Point Sources

In order to model point sources, a catalogue of point sources first needs to be generated. To do this eq. 2.3.8 was rearranged to give dN/dS and then integrated over a desired range of S_{\min} to S_{\max} . This would give the total number of sources per steradian, from which it is then possible to work out the number of sources in any given area of sky. Once the total number of sources was known point sources were randomly generated within the given area of sky where the fluxes of each

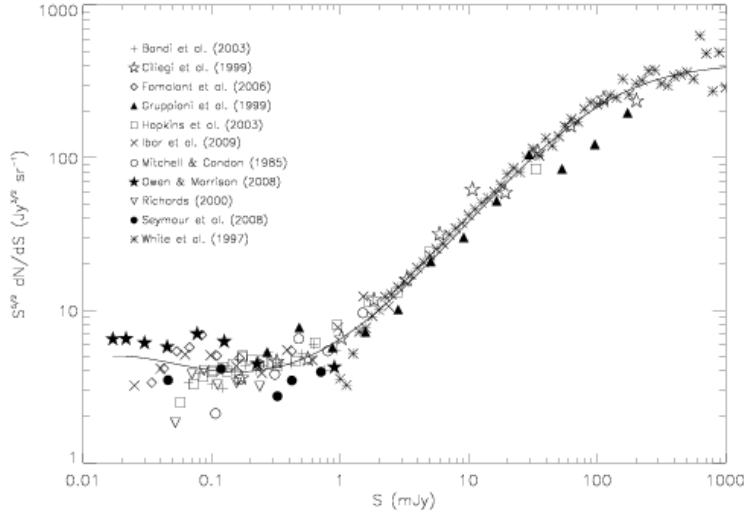


Figure 2.11: *Differential source count data at 1.4 GHz, taken from Battye et al. (2013). The thin solid line represents the best fit to the data, eq. 2.3.8.*

position were distributed according to eq. 2.3.8. Fig. 2.12 shows the equation that was used to generate the point sources within a particular area (solid black line) and the data points represent the differential source count of the randomly generated points. It was found that for a $4 \times 4 \text{ deg}^2$ area of sky with $S_{\min} = 0.1 \text{ mJy}$ and $S_{\max} = 10 \text{ Jy}$ the total number of sources was 14248.

The fluxes for each point source were generated at 1.4 GHz so in order to do observations at different frequencies, the fluxes need to be scaled accordingly using

$$S(\nu) = S_0 \left(\frac{\nu}{1.4 \text{ GHz}} \right)^\alpha, \quad (2.3.9)$$

where $S(\nu)$ and S_0 represent the flux at frequency ν and at 1.4 GHz respectively, and α is the average spectral index across the frequency range which takes the value ≈ -0.7 .

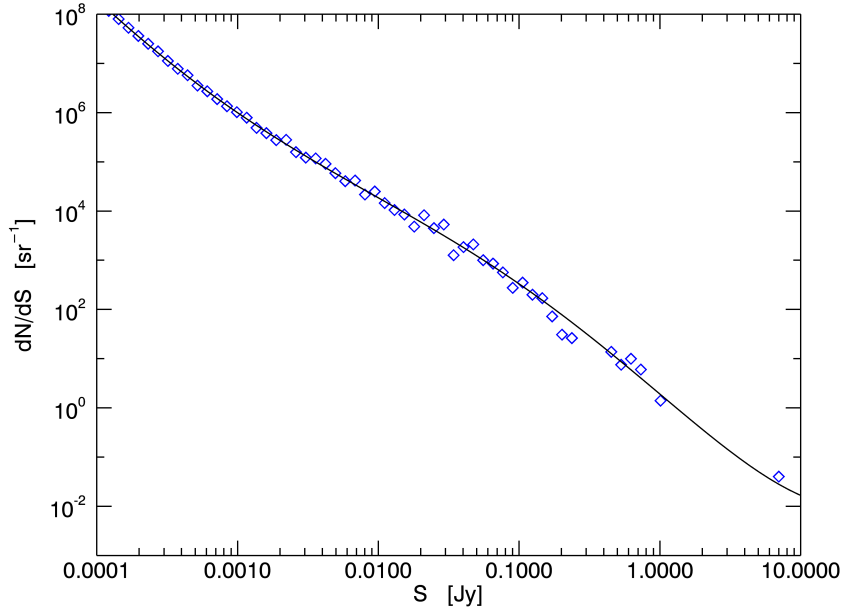


Figure 2.12: *Plot showing the source counts as a function of flux density at 1.4 GHz (\diamond) and the fit that was used to generate them (solid black line).*

2.3.3 Foregrounds Removal Methods

21 cm emission should exhibit both angular fluctuations and structure in redshift space at high z . These are caused by spatial variations in hydrogen density, spin temperature and ionization fraction. It was thought that these angular fluctuations of the 21 cm signal could be exploited and work was done to investigate to what extent the 21 cm fluctuations are impeded by noise from extragalactic foreground radio sources.

It was found that the unresolved extragalactic radio sources are likely to give rise to temperature fluctuations that far exceed the expected signal at all scales and frequencies. In particular, extended cluster radio halos and relics contribute the largest fraction. Di Matteo et al. (2004) have shown that the spatial clustering of bright foreground sources dominates the angular fluctuations at scales $\theta \gtrsim 1$

arcmin. However, if sources above flux levels $S \gtrsim 0.1$ mJy (out to $z \sim 1$ for diffuse sources and $z \sim 2$ for point sources) can be detected and removed then this excess in fluctuations can be removed. This efficient source removal may therefore allow the detection of 21 cm angular fluctuations at $\theta \gtrsim 1$ arcmin. Removal of sources above $S = 0.1$ mJy also reduces foreground fluctuations to roughly the same level as those of the 21 cm signal at scales $\theta \lesssim 1$ arcmin meaning that subtraction of foreground components in frequency space (by comparing maps closely spaced in frequency) will allow the signal to be detected at small scales.

Many authors now make the assumptions that this flux cutting technique developed by Di Matteo et al. (2004) accurately removes bright sources. Since it has been shown that the residuals from this bright source subtraction are below the thermal noise, this is an acceptable assumption to make.

Foregrounds are expected to be correlated in the frequency direction while the 21 cm signal is expected to be uncorrelated, motivating removal methods which focus on the frequency correlation. For example, Zaldarriaga et al. (2004) used the cross-correlation of pairs of maps as a method of cleaning. If foregrounds are perfectly correlated across frequencies then subtracting two maps from each other would completely remove the foregrounds. Any reduction in the foreground correlation means subtraction is not as effective.

Much work has been done to investigate the problem of foreground removal and as a result there are many techniques to choose from, each with its advantages and disadvantages. These methods roughly fall into two categories; ‘blind’ principle component analysis (PCA) based methods where no assumption about the foregrounds is made; and parametric fitting methods where a particular form is assumed for the foregrounds. Some of the popular foreground (FG) removal methods are summarised in Table 2.2.

Method	Notes/assumptions	Author (e.g.)	Pros	Cons
Smoothing/power-law fitting	FGs modelled as power laws, constant beam size in freq.	Santos et al. (2005)	High level of FG cleaning despite conservative FG models	Point sources problematic due to short correlation length
Pixel polynomial fitting	2 nd order log-log polynomial in freq.	Wang et al. (2006)	Unaffected by huge variations of FG spectral index across sky	Fit not as good with noise, not possible fit more than 1 FG well
Wp smoothing	non parametric	Harker et al. (2009)	Can fit in either image or Fourier space	Slow to compute results in Fourier space
SVD decomposition	non parametric	Chang et al. (2010)	Removes smooth FGs	Loss in 21 cm signal needs correcting
Inverse variance FG subtraction in Fourier space	non-blind, depends on knowledge of foreground properties	Liu and Tegmark (2011)	Reduces mode-mixing problem, noise and FG biases removed, small error bars	Inverting large matrices is slow
Power spectrum subtraction	Subtract FG angular power spectrum leaving 21 cm power spectrum	Cho et al. (2012)	FG fit not required	
Polynomial fitting in Fourier space	Uniform weighting, inverse variance weighting	Mao (2012)	Thermal noise power spectrum not required to extract signal	Lower signal to noise in each sub-band degrades fit
FASTICA	FG statistically independent and non-Gaussian	Chapman et al. (2012)	Performs equally well in Fourier and image space	Less robust when large noise levels considered
GMCA	Uses sparsity and morphological diversity to separate FG sources	Chapman et al. (2013)	21 cm phase information well preserved	Currently 21 cm signal only found as residual rather than it's own signal
Wavelet filtering	FG smooth in freq.	Gu et al. (2013)	Can cope with uncorrected instrument response errors	

Table 2.2: Summary of foreground removal methods briefly outlining some advantages and disadvantages. Examples of authors working on each method have also been given for more information.

So far, none of the foreground removal methods are perfect and residual errors from these subtraction methods remain. These errors can be studied and the average fitting errors of these methods can be subtracted from the 3D power spectrum, further reducing the contamination of the signal by residual foregrounds.

For example, errors in the bright source removal stage arise as a result of the slight mis-estimation of the flux of each source. This leads to residual positive and negative sources at the same place where the original source was subtracted, leading to spurious power in the power spectrum. It would be impossible to work out the error on each individual source but an average error for all of the sources can be predicted and removed from the residual foreground contamination. Positive and negative residuals will have the same power spectrum signature as the power spectrum is related to the squared intensity.

Chapter 3

Radio Interferometry

Radio emission, at wavelengths between 10 m ($\nu = 30$ MHz) and 1 mm ($\nu = 300$ GHz), from astronomical objects can be studied using radio telescopes. They can be used to measure spectroscopic features from spectral lines as well as broadband continuum radiation. Although the design of radio telescopes may vary greatly, they all have two basic features: *(i)* large radio antenna and *(ii)* radio receiver to amplify and detect signals. A radio telescope's sensitivity depends on the antenna's area and the sensitivity of the radio receiver. There are several factors which limit the performance of a radio telescope: *(i)* reflecting surface may deviate from ideal shape; *(ii)* thermal deformation causing expansion/contraction; and *(iii)* deflections as a result of the gravitational forces changing when the antenna position is changed. The receiver, which accepts the signal from the antenna and, after processing, outputs an intelligible signal has its own problems associated with it, noise being the main limitation. Noise can either be external from interfering sources or internally generated in, for example, transmission lines and connectors that connect the antenna to the first amplifier stage.

Interferometers use the principle of aperture synthesis to mix signals from several telescopes and produce an image. In the simplest interferometer with two

elements, the rotation of the Earth causes signals to arrive alternatively in and out of phase. This creates a variation of the path difference between the source and the two interferometer components giving rise to interference fringes. This path difference varies across the source, assuming the radio source has finite angular size, meaning that the measured fringes depend on the radio ‘brightness’ distribution.

An interferometer measures $\langle E_1 E_2^* \rangle$, where E_1 and E_2 are electric field vectors measured by two antennas looking at the same point on the sky. The average of the product of electric fields is just the intensity multiplied by a phase factor (White et al., 1998). The phase factor is given by the path difference between the source and the two antennas. We can then take the integral over the source/emitter plane to give the Fourier transform of the observed intensity. Observed intensity is given by the sky intensity times the beam.

The observable measured by an interferometer is called a visibility which is proportional to the Fourier transform of the observed intensity. The observed visibilities are samples of the uv -plane (Fourier plane) and given by the van Cittert Zernike equation (Thompson et al., 1986):

$$V(\mathbf{u}) \propto \int A(\mathbf{x}) \Delta T(\mathbf{x}) e^{2\pi i \mathbf{u} \cdot \mathbf{x}} d\mathbf{x}, \quad (3.0.1)$$

where ΔT is the temperature fluctuation, $A(\mathbf{x})$ is the primary beam, \mathbf{x} is a unit vector, \mathbf{u} is a spatial frequency and the conjugate variable to \mathbf{x} , measured in wavelengths. The omitted constant of proportionality converts from temperature to intensity. Each pair of antennas measures a visibility at a particular point in the uv -plane.

The value of \mathbf{u} measured by a particular pair of antenna is determined by the physical position of the antennas and the position of the beam on the observed

sky (White et al., 1998). When movable antenna and the rotation of the earth are combined, sufficient numbers of Fourier components can be sampled to produce high resolution images of the sky. The visibilities lie on a series of curves in the uv -plane called uv -tracks.

The size of the primary beam determines the field of view while the maximum spacing between antennas determines the resolution (see eqn 1.4.1 in Section 1.4). Sources larger than λ/d_{\min} , where d_{\min} is the minimum spacing between antennas, are resolved out while sources smaller than λ/d_{\max} , where d_{\max} is the maximum baseline, appear as point sources. The interferometer configuration is chosen to match the maximum and minimum scales of the structure in the source that is being observed. Generally the interferometer's FOV is small so the sky can be assumed flat using the small angle approximation.

As the power spectrum, C_ℓ , is basically a FT of the sky, interferometers almost directly measure the power spectrum. Averaging the squared visibilities, $|V(\mathbf{u})|^2$, in shells of constant \mathbf{u} provides an estimate of C_ℓ at $\ell = 2\pi\mathbf{u}$ convolved with a window function, which is determined by the FT of the primary beam (Dickinson, 2012). To obtain images from the interferometer data high speed computers are used to perform fast Fourier transforms. The visibilities get inverted to produce images of the sky convolved with the beam.

3.1 Current HI Intensity Mapping Experiments

There are several current telescopes already trying to do intensity mapping with several others in the process of construction. This section will briefly outline a few of them.

The Green Bank Telescope (GBT) is the world's largest steerable radio telescope. It has a diameter of 100m and a collecting area of $\sim 8000 \text{ m}^2$. It has

an angular resolution of $\sim 0.25^\circ$ at $z \sim 0.8$, when observing HI, which is suitable for intensity mapping. Chang et al. (2010) reported the first detection of the cross-correlation between large scale structure and 21 cm intensity maps using GBT data with the DEEP2 galaxy survey with a measurement of $\Omega_{\text{HI}} b_{\text{HI}} r = [0.66 \pm 0.18(\text{stat.})] \times 10^{-3}$, where Ω_{HI} is the HI fraction, b_{HI} is the HI bias parameter, and r is the galaxy-hydrogen correlation coefficient. Masui et al. (2013) improved on the measurements by cross correlating new GBT intensity map data with the WiggleZ survey. They achieved $\Omega_{\text{HI}} b_{\text{HI}} r = [0.43 \pm 0.07(\text{stat.}) \pm 0.04(\text{sys.})] \times 10^{-3}$ which is the most precise constraint on the HI density fluctuations in the range $0.6 < z < 1$. Switzer et al. (2013) also used GBT data to measure HI fluctuations giving $\Omega_{\text{HI}} b_{\text{HI}} = [0.62^{+0.23}_{-0.15}] \times 10^{-3}$.

Another promising telescope is the Canadian Hydrogen Intensity Mapping Experiment (CHIME). It will be a purpose built telescope to observe BAOs in the redshift range $2.5 \geq z \geq 0.7$ with a collecting area of 10,000 m². The idea is that CHIME will produce data many years before other instruments of comparable sensitivity for a small fraction of the cost. A small scale prototype 1/10th the size of CHIME is being built first which will be used to improve the final CHIME design, details of which can be found in Bandura et al. (2014).

Finally, the BINGO experiment (Baryonic acoustic oscillations In Neutral Gas Observations) is a new project to build a bespoke single dish radio telescope to map neutral hydrogen in the range $0.13 < z < 0.48$. The telescope will not have any moving parts and consist of a primary mirror of 40 m and a smaller secondary mirror. Battye et al. (2013) made sensitivity and uncertainty estimates for a year of observing and found that it would be possible to measure BAOs at $z \sim 0.3$ with an accuracy of $\sim 2.4\%$ and w to an accuracy of 16%.

The projected results from these experiments indicate that trying to measure dark energy using intensity mapping is a promising technique.

3.2 Interferometers of Interest

We have already seen that several 21 cm BAO instruments have been either proposed or are under construction. The aim of this thesis is to investigate whether it would be possible to use any of the up and coming radio interferometers for intensity mapping experiments, even though they have not been designed with this task in mind. The two interferometers being considered are the Australian Square Kilometre Array Pathfinder (ASKAP) and MeerKAT.

ASKAP is a new radio telescope being commissioned at the Murchison Radio-astronomy Observatory (MRO) in Western Australia designed to capture radio images over large areas of the sky with unprecedented sensitivity. ASKAP saw first light on 5 October 2012 and is the world's fastest radio telescope, with a survey speed greater than any other radio telescope. This combination of survey speed and sensitivity will allow astronomers to answer questions about the early universe, test predictions from general relativity and theories of cosmic magnetism¹.

ASKAP will also be an important demonstrator for the Square Kilometre Array (SKA) project, a future international radio telescope that is to be the largest and most sensitive in the world. The MRO has been selected as the central site for major SKA components. The wide field of view, large bandwidth, excellent uv -coverage and very fast survey speed are some of the unique features that make ASKAP an exceptional synoptic telescope¹. The radio quiet site will also help to make substantial advances in important areas of SKA science.

MeerKAT is a radio telescope under construction in South Africa. Once complete it will be the largest and most sensitive radio telescope until SKA is up and running. As well as being a technology demonstrator for the SKA, it will do research into cosmic magnetism, galactic evolution, large-scale structure and dark

¹<http://www.atnf.csiro.au/projects/askap/index.html>

matter².

Tianlai is a proposed interferometer built specifically for 21 cm intensity mapping for $0.3 < z < 3$. It will be based on a dense interferometer idea using either small parabolic antennas (about 5 m diameter) or a packed cylinder array (Chen, 2012).

Although not the primary aim of either MeerKAT or ASKAP, it would be interesting to see whether these instruments could be used to detect baryonic acoustic oscillations (BAOs) in the neutral HI signal through intensity mapping. This thesis will focus on comparing how MeerKAT and ASKAP perform against the more bespoke instrument, Tianlai.

Currently there is no specific Tianlai antenna configuration so we designed our own Tianlai-like array configuration that is based on similar ideas and will therefore give a good idea of what a Tianlai-like interferometer can do. Chen (2012) has proposed that a compact array with maximum baseline of 100 m (corresponding to a resolution of 14 arcmin at $z \sim 1$) would be able to detect the BAOs so this is the model we based our configuration on. We used 100 dishes each with a diameter of 4 m. The dish positions were randomly generated within an area of diameter 100m, requiring a minimum separation of 1 m between the edges of the dishes. The resulting array can be seen in top plot of Fig. 3.1.

The middle row of plots in Fig. 3.1 show the positions of the 64 MeerKAT dishes, provided by Minh Huynh³. The left plot shows all the dishes while the right plot shows just the dishes concentrated in the dark area on the left plot. It is clear that most dishes are centred at the middle and very close to each other with only a few dishes providing the longer baselines (small scales).

The ASKAP configuration, given by the bottom row of plots in Fig. 3.1, was

²<http://www.ska.ac.za/meerkat/>

³minh.huynh@uwa.edu.au

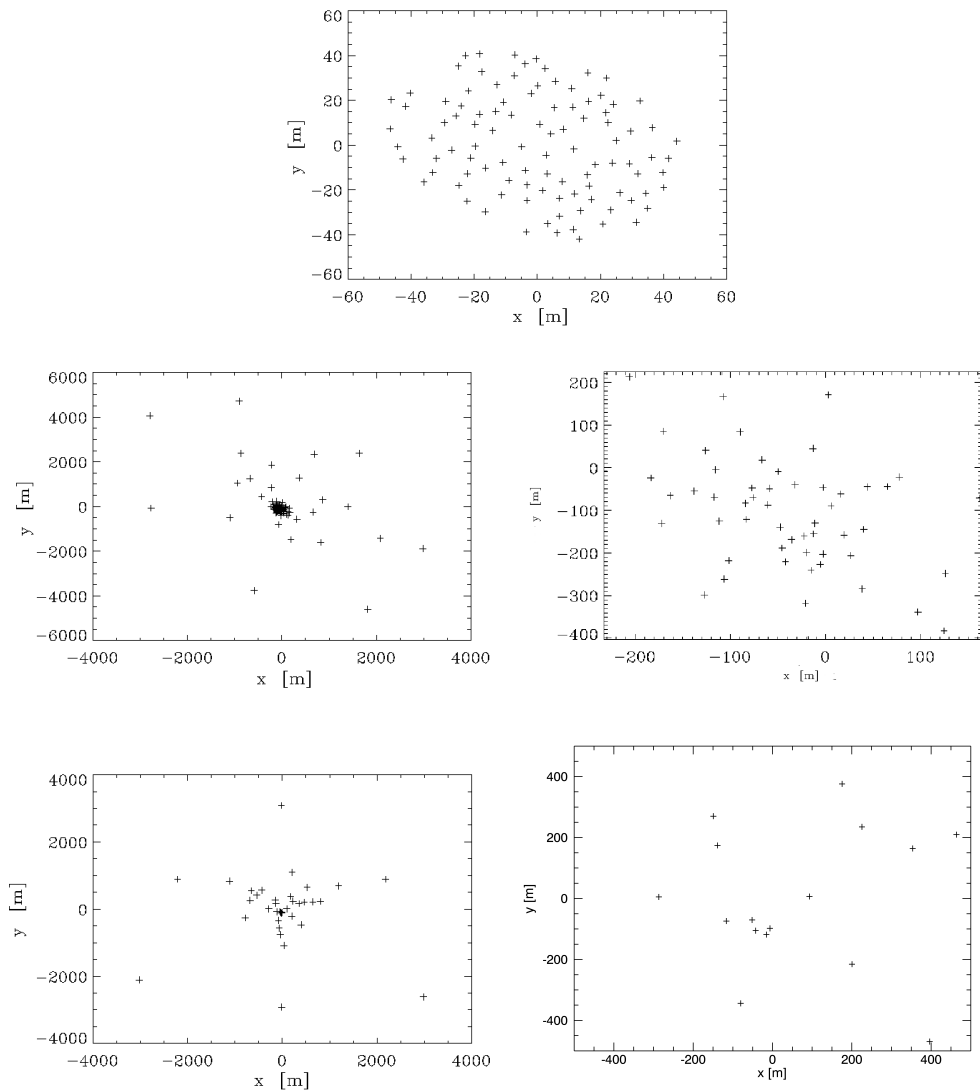


Figure 3.1: *Dish positions for Tianlai-like (top), MeerKAT (middle row) and ASKAP (bottom) array configuration, given in metres. The zoomed in plots for MeerKAT and ASKAP show the central dish positions more clearly.*

also provided by Minh Huynh. A slightly older version can also be found online⁴. It is made up of 36 dishes, each with a diameter of 12 m. Again, most of the dishes are central and fairly close to each other. ASKAP's 36 identical antennas

⁴http://www-astro.physics.ox.ac.uk/~hrk/Array_Simulator.html

each have 1 deg^2 beams. These independent beams will work together as a single instrument to produce a 30 deg^2 field of view at 1.4 GHz with a total collecting area of $\sim 4000 \text{ m}^2$. This is achieved using a phased array feed (PAF) mounted on each antenna. PAFs are a new type of focal plane array being designed for the Westerbork Synthesis Radio Telescope (WSRT) and ASKAP (Landon et al., 2009). It consists of antennas that instead of working independently, act as sensors of the sky's electromagnetic field across the entire focal plane of the telescope. Each of ASKAP's PAF requires 188 individual receivers which are situated near the antennas focus. The receiver outputs are coherently combined in a beamformer to synthesize multiple simultaneous beams on the sky. Complete coverage of the potential field of view is therefore possible without loss of sensitivity in each beam⁵. The frequencies at which ASKAP is designed to operate range from 700 MHz to 1.8 GHz with a 300 MHz instantaneous bandwidth. The maximum baseline will be approximately 6 km ⁶. Instead of simulating 36 individual beams with a total field-of-view of 30 deg^2 , the ASKAP PAFs will be approximated by one large primary beam of 30 deg^2 . Although not strictly correct, this will be computationally quicker and is a reasonable approximation to give an idea of what the instrument can do.

The aperture efficiency is defined as the ratio of the effective collecting area of a dish to its total geometric area. The expected efficiency of the dishes in the three arrays of interest are very similar, as can be seen in Table 3.1 where a summary of the properties of each arrays is given.

It is clear from Fig. 3.1 that the three interferometers are very different. To see how the different configurations effect the performance of the interferometer and its potential for detecting BAOs, the uv -coverage for each array were plotted and compared.

Fig 3.2 compares the uv -coverage for the three different array configurations.

⁵https://science.nrao.edu/science/Decadal%20Survey/tech/Fisher_PhArrayFeed_TEC_RMS.pdf

⁶<http://www.atnf.csiro.au/projects/askap/index.html>

	Tianlai	MeerKAT	ASKAP
Number of Dishes	100	64	36
Dish Diameter (m)	4	13.5	12
Efficiency	0.7	0.7	0.8
T_{sys} (K)	30	30	50
Resolution	15' at $z = 1$	6'' – 80''	optimised for 30''
Field of View	9 deg ²	1 deg ²	30 deg ²

Table 3.1: Summary of properties for the Tianlai-like, MeerKAT and ASKAP array configurations.

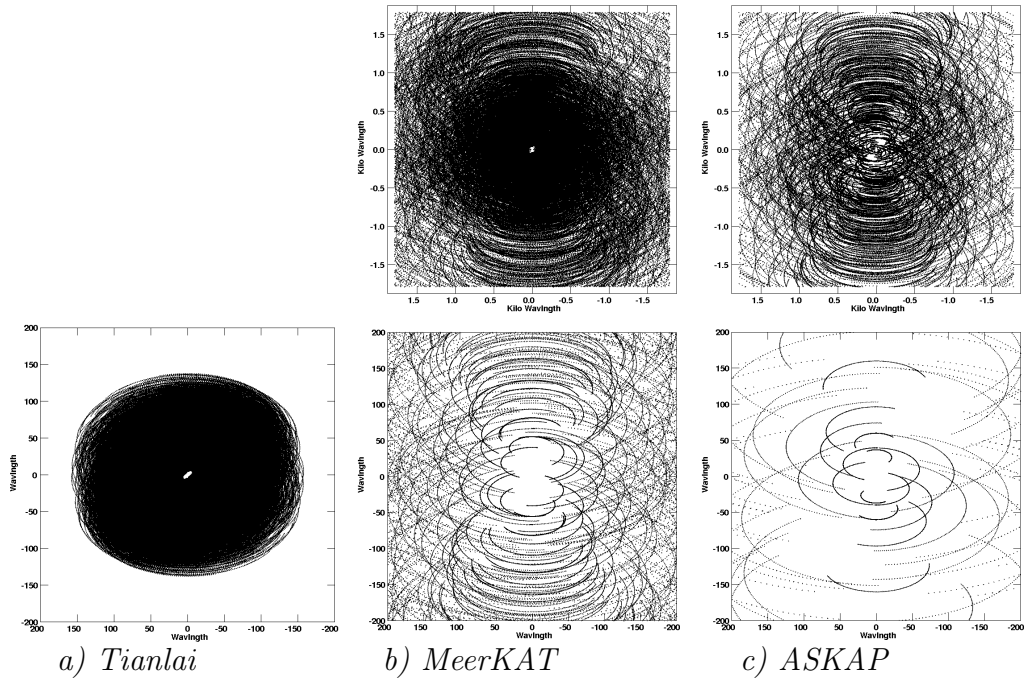


Figure 3.2: UV-coverage for each array configuration. The top row shows the uv plane for MeerKAT and ASKAP whereas the bottom row shows the uv planes on the same scale for each interferometer as the complete uv plane for Tianlai is much smaller than the others. The plots were made for a 12 hour observation at declinations of $+30^\circ$ for Tianlai and -30° for MeerKAT and ASKAP, based on the site location of each interferometer.

The top images for MeerKAT and ASKAP shows the uv -plane while the lower images show the uv -plane on the same scale as the Tianlai array. It is clear from these images that Tianlai is best set up for potentially detecting BAOs through

intensity mapping. This is because the more compact array gives a better filling factor and the best uv -coverage over the large scales relevant to BAOs. Tianlai also has the smallest dishes so it will have a bigger field of view than MeerKAT and ASKAP would have (see Table 3.1). ASKAP gets round this by using the PAFs as described previously. ASKAP and MeerKAT on the other hand have lots of large baselines which will give good coverage at the very small scales but less at the large scales that we are interested in, which can be seen by comparing the lower uv -coverage plots. ASKAP in particular has especially poor coverage on the larger scales indicating that it might be difficult to detect anything with it.

A histogram of the number of baselines at various angular scales was plotted (see Fig. 3.3) for each of the three interferometers to illustrate more clearly the differences between the array configurations.

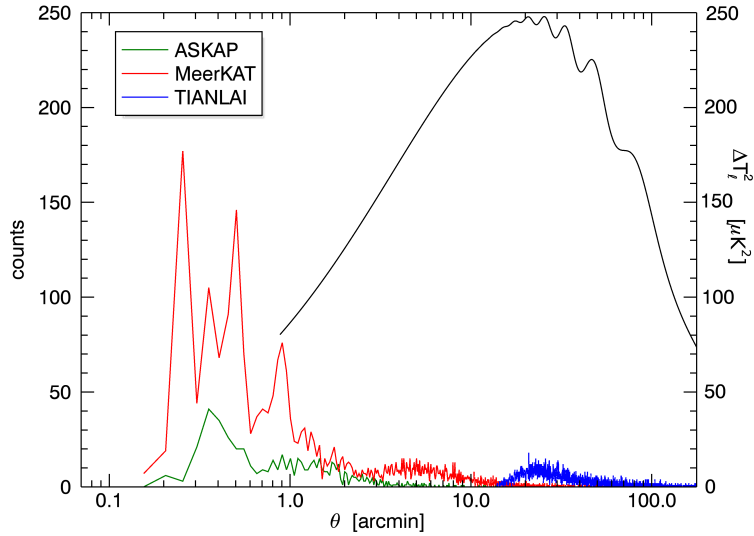


Figure 3.3: *Histogram of baselines for each of the three interferometers at 800 MHz with the HI angular power spectrum plotted for comparison.*

From the histogram in Fig. 3.3 it is clear that both MeerKAT and ASKAP have most of their coverage at small angular scales (less than 1 arcmin). MeerKAT has

a small cluster of baselines at scales around 5 – 10 arcmin while Tianlai’s baselines give coverage on scales greater than 10 arcmin. The HI angular power spectrum has been plotted and it can be seen that the BAO wiggles start at scales around 20 arcmins. These angular scales are covered best by Tianlai indicating that it may be the best interferometer to observe BAO peaks.

3.3 Simulating Interferometric Observations

To simulate interferometer observations a Tcl script was written, initially by Clive Dickinson and modified by myself. An example of this script can be found in Appendix A. We also made extensive use of the Astronomical Image Processing System (AIPS⁷) package. The first step made use of the AIPS task FITLD which read in our model of the sky, in the form of a FITS cube (see section 2.2). The 3D cube is then split up into individual channel maps in the frequency direction using SUBIM. The simulated observations can now be done for each frequency slice.

The observed visibilities were simulated using the AIPS task UVCON, which requires an array model. The properties of the array are read from an antenna file and the uv -coverage of the interferometer is determined. The antenna file consists of a list of antenna locations, antenna diameter, antenna temperature and aperture efficiency. Other inputs required by the task UVCON include the total observation time and the integration time per visibility. It is also possible to set the type of primary beam model used in UVCON. For the work in this thesis the primary beam was modelled as a Gaussian where the FWHM major and minor axes of the primary beam are specified in degrees. At high redshifts (low frequencies) the primary beam widens, resulting in a larger field-of-view. At 1000 MHz, the primary beam is 40% larger than at 1420 MHz and 75% larger at 800 MHz. This effect was

⁷<http://www.aoc.nrao.edu/aips/>

taken into account, otherwise large amounts of data are lost at high redshifts. The visibilities are calculated for each channel from a fast Fourier transform (FFT) of the model image. The uv -data channels are then combined into one big uv -data set using the task `UVGLU` and a uv FITS data file is output. Gaussian noise is calculated and added by `UVCON` based on the specified antenna characteristics and integration times.

The task `IMAGR` can produce dirty or deconvolved images from the uv -data using a FFT. A dirty image is a convolution of the sky brightness (true image) with the dirty beam. The dirty beam (also known as the point spread function) is the Fourier transform of the sampling function, and its shape is determined by the uv -coverage. Any holes in the uv -coverage lead to side lobes in the dirty beam. The synthesized beam is an elliptical Gaussian fitted to the dirty beam and determines the resolution of the interferometer.

Different weighting schemes can be chosen for the simulation including natural weighting (all visibility samples have equal weights), uniform weighting (each cell in the uv -plane has equal weights) and robust weighting (compromise between natural and uniform weighting). Natural weighting has the advantage of minimum noise but often applies too much weight to points near the origin, creating significant side lobes in the beam. On the other hand uniform weighting allows for a higher resolution than natural weighting but tends to be more noisy. For our work a natural weighting scheme was chosen.

Tapering can also be used to downweight high spatial frequencies. This can be useful when the array configuration consists of many long baselines (corresponding to very small scales) which are not of interest to us. Tapering is applied by multiplying by a Gaussian function in the uv -plane. This is equivalent to a convolution by a Gaussian function in the image plane. Tapering gives lower point source sensitivity but better brightness temperature sensitivity. For both the MeerKAT

and ASKAP configurations a uv -taper of $5 \text{ k}\lambda$ was used to throw away some of the long baselines, giving a synthesized beam of about $6'$.

3.3.1 Millennium Simulation Dirty Maps

In order to compare the performance of the interferometers and see the effect of the array configurations more clearly, the Millennium FITS cube (see section 2.2) was used as the input model in AIPS along with array configuration files for each of Tianlai, ASKAP and MeerKAT. The dirty maps for each interferometer were then compared and can be seen in Figs. 3.4, 3.5 and 3.6. Three different frequencies were chosen (1000 MHz, 1200 MHz and 1400 MHz) which show individual galaxies at the very high frequency and diffuse emission at the lower frequency.

Figs 3.4, 3.5 and 3.6 show slices from the output image cubes with each figure showing results for a different frequency. The top row of images in each figure are slices showing the output image that each interferometer would be able to see if no noise was present, i.e. only the signal. This no noise simulation was done by setting $T_{\text{sys}} = 0 \text{ K}$ in the array configuration file so as to only observe the signal in the Millennium input cube. The next row down show the results of a 12 hour observation but for most arrays and most frequencies this is not long enough to start detecting any signal over the noise levels. In an attempt to reduce the noise the observation can be done for a longer time. Instead of running the simulation for longer, which would be more time intensive, the antenna temperature can be reduced to simulate longer observation times since $T_{\text{sys}}^2 t_{\text{obs}} = \text{constant}$ (see Section 1.4 where we saw $T_{\text{sys}} = T_{\text{A}} + T_{\text{CMB}} + \dots$). This effectively corresponds to multiple 12 hour observations. The third, fourth and fifth rows in each figure show slices from the simulated FITS cube for observation times of 120 hrs, 1200 hrs and 12000 hrs, and include the signal and the effect of noise from the array antennas.

Looking at Fig 3.4 first it is clear that Tianlai starts to detect diffuse emission

after 1200 hours while MeerKAT only starts to detect anything after about 12000 hours. ASKAP also just about detects some of the diffuse emission around 12000 hours but it is not as clear as MeerKAT.

Moving to higher frequencies in Fig 3.5 Tianlai, again, performs the best out of the three arrays, detecting signal by 120 hours. MeerKAT performs better than ASKAP with signal being detected after 1200 hours while ASKAP only seems to be able to detect galaxies and diffuse emission after 12000 hours.

Looking at the highest frequency in Fig 3.6 Tianlai is detecting galaxies after only 12 hours. MeerKAT also just about detects galaxies after 12 hrs but better results are achieved by 120 hours. ASKAP on the other hand definitely detects galaxies by 1200 hours with some of the very bright objects being detected after 120 hours.

The reason for these differences in the dirty maps are to do with the arrangement of antennas. Long baselines give a higher resolution which is better for detecting individual galaxies. Short baselines mean a lower resolution which is better for detecting diffuse emission. ‘Tianlai’ will therefore be better at detecting the diffuse emission at lower frequencies than either MeerKAT or ASKAP, which will be able to individual galaxies well at higher frequencies. This is shown in the dirty maps.

Although maps are useful to give a general idea of what each interferometer should be able to detect, using a power spectrum analysis is a cleaner, more quantitative method. This is because the angular information is binned in a statistical manner that can be easily compared to theoretical models and simulations. The power spectrum allows structure to be seen that is not very clear in the maps, so a power spectrum analysis should be an improvement on the dirty maps. The following Chapters will explore this method in more detail.

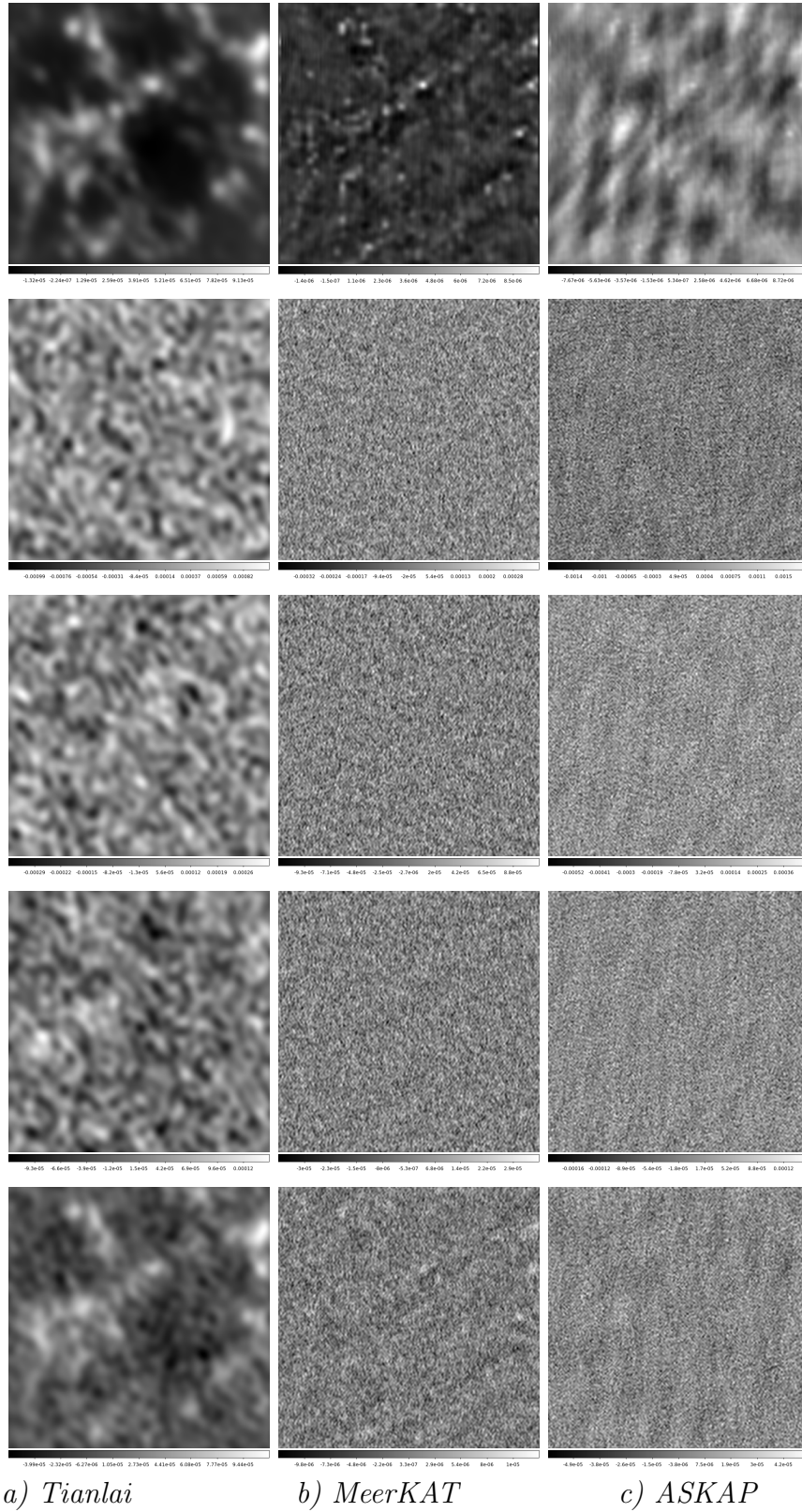


Figure 3.4: *Dirty maps for each array at different observation times. The top row shows dirty maps with no noise while the remaining rows show dirty maps for observation times of 12 hrs, 120 hrs, 1200 hrs and 12000 hrs from second to fifth row. All slices are at $f = 1000$ MHz with $\Delta f = 5$ MHz, showing an area of $5.5 \times 5.5 \text{ deg}^2$. The scale is linear, with maximum and minimum values determined by scanning the image, and in units of Jy/pixel.*

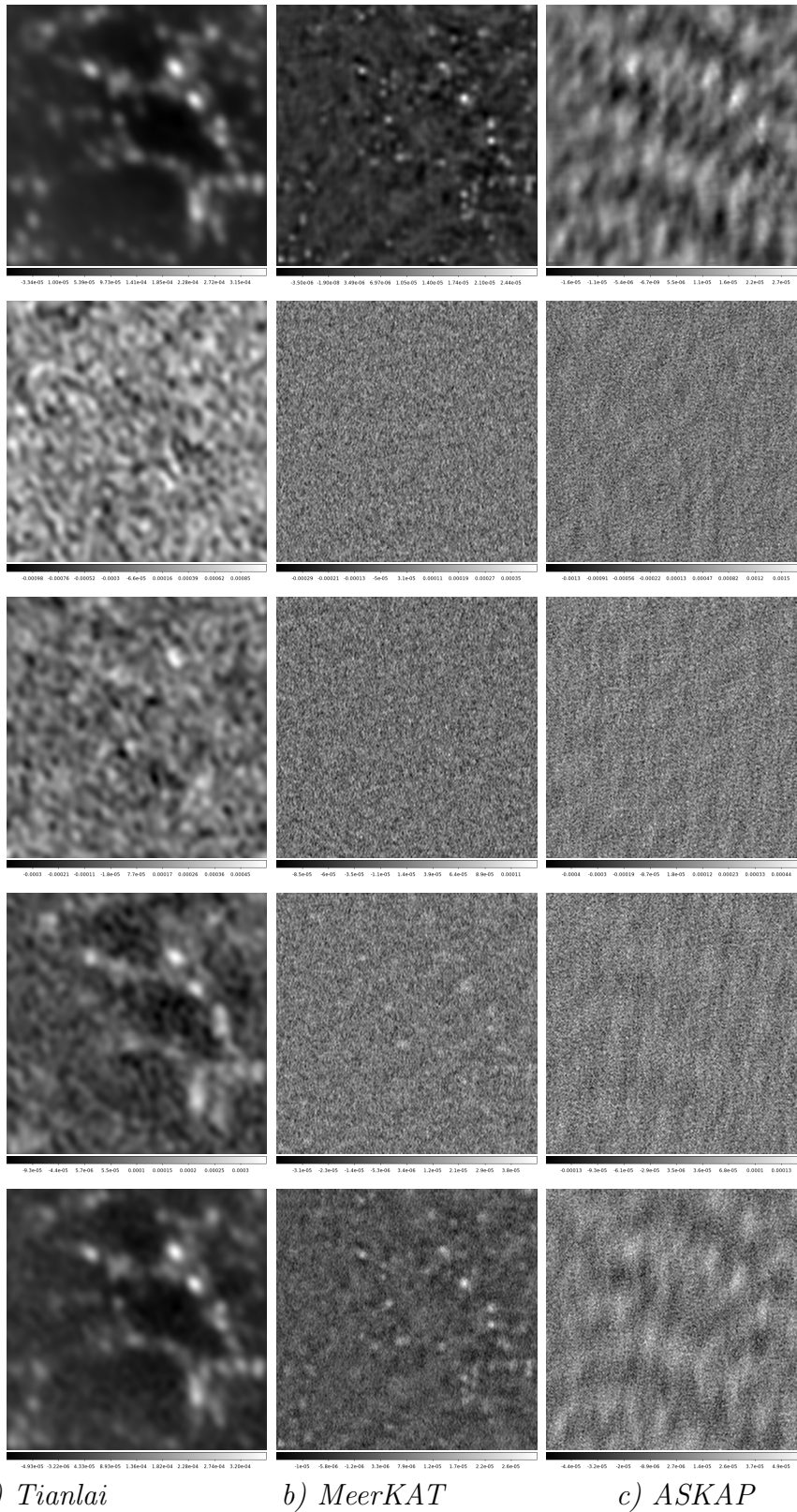


Figure 3.5: *Dirty maps for each array at different observation times. The top row shows dirty maps with no noise while the remaining rows show dirty maps for observation times of 12 hrs, 120 hrs, 1200 hrs and 12000 hrs from second to fifth row. All slices are at $f = 1200$ MHz with $\Delta f = 5$ MHz, showing an area of 5.5×5.5 deg². The scale is linear, with maximum and minimum values determined by scanning the image, and in units of Jy/pixel.*

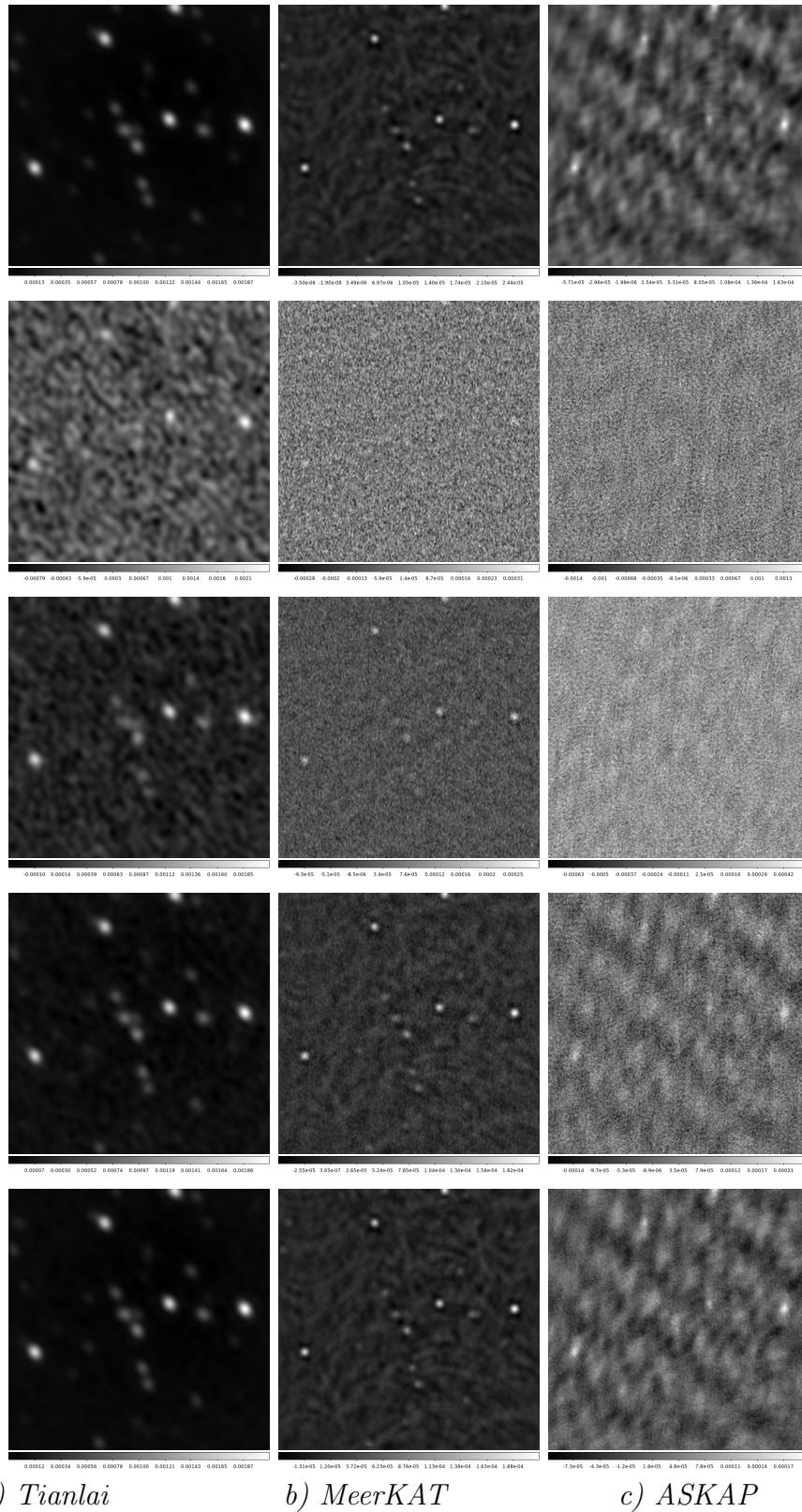


Figure 3.6: *Dirty maps for each array at different observation times. The top row shows dirty maps with no noise while the remaining rows show dirty maps for observation times of 12 hrs, 120 hrs, 1200 hrs and 12000 hrs from second to fifth row. All slices are at $f = 1400$ MHz with $\Delta f = 5$ MHz, showing an area of $5.5 \times 5.5 \text{ deg}^2$. The scale is linear, with maximum and minimum values determined by scanning the image, and in units of Jy/pixel.*

Chapter 4

Power Spectrum Estimation

Temperature fluctuations are usually described as an expansion in spherical harmonics

$$\frac{\Delta T(\mathbf{x})}{T} = \sum_{\ell=0}^{\infty} \sum_{m=-\ell}^{\ell} a_{\ell m} Y_{\ell m}(\mathbf{x}). \quad (4.0.1)$$

The $a_{\ell m}$ s completely describe how the galaxies are distributed in spherical harmonic space. The autocorrelation of the spherical harmonic expansion is used to calculate the power spectrum, C_{ℓ} , which contains information about the preferred correlation length. If the matter distribution is a realisation of a Gaussian random field the mean is $\langle a_{\ell m} \rangle = 0$ and the variance is $\langle a_{\ell m} a_{\ell m}^* \rangle = C_{\ell}$. This gives an estimator of the power spectrum in spherical harmonic space,

$$C_{\ell} = \frac{1}{2\ell + 1} \sum_{m=-\ell}^{\ell} |a_{\ell m}|^2. \quad (4.0.2)$$

The power spectrum is related to the temperature fluctuations by

$$\Delta T_{\ell}^2 = \frac{\ell(\ell + 1)C_{\ell}}{2\pi}, \quad (4.0.3)$$

where T_ℓ^2 is the temperature at a particular value of ℓ and is in units of $(\mu\text{K})^2$ and $\ell = 2\pi|u|$.

When observing small patches of sky, it is more convenient to use Fourier analysis giving

$$\frac{\Delta T(\mathbf{x})}{T} = \int \tilde{T}(\mathbf{u}) e^{2\pi i \mathbf{u} \cdot \mathbf{x}} d^2 \mathbf{u}, \quad (4.0.4)$$

where \tilde{T} is the Fourier transform of the temperature fluctuations and \mathbf{u} , the spatial frequency, is the variable conjugate to \mathbf{x} , measured in wavelengths.

We can define the ensemble averaged power spectrum as (Hobson et al., 1995)

$$\langle \tilde{T}(\mathbf{u}) \tilde{T}^*(\mathbf{u}') \rangle = C(\mathbf{u}) \delta(\mathbf{u} - \mathbf{u}'), \quad (4.0.5)$$

if the emission is statistically isotropic and uncorrelated.

We have seen that an interferometer measures the Fourier transform of the product of the sky temperature fluctuations and the primary beam, $A(\mathbf{x})$ (see Chapter 3), and the visibilities are given by (see also eq. 3.0.1)

$$V(\mathbf{u}) \propto \int A(\mathbf{x}) \frac{\Delta T(\mathbf{x})}{T} e^{2\pi i \mathbf{u} \cdot \mathbf{x}} d^2 \mathbf{x}. \quad (4.0.6)$$

Substituting in eq. 4.0.4, it can be shown that the observed visibilities are given by a convolution of the sky and the aperture:

$$\begin{aligned} V(\mathbf{u}) &\propto \int d^2 \mathbf{u}' \tilde{T}(\mathbf{u}') \int d^2 \hat{\mathbf{x}} A(\mathbf{x}) e^{2\pi i (\mathbf{u}' - \mathbf{u}) \cdot \mathbf{x}} \\ &\propto \int d^2 \mathbf{u}' \tilde{T}(\mathbf{u}') \tilde{A}(\mathbf{u}' - \mathbf{u}) \\ &\propto (\tilde{T} * \tilde{A})(\mathbf{u}') \end{aligned} \quad (4.0.7)$$

where \tilde{A} is the Fourier transform of the primary beam and

$$\tilde{A}(\mathbf{u}) = \int d^2\mathbf{x} A(\mathbf{x}) e^{-2\pi i(\mathbf{u}\cdot\mathbf{x})}. \quad (4.0.8)$$

The squared visibility is usually measured and this, along with eq. 4.0.5, is used to relate the power in the visibilities with the ensemble averaged power spectrum;

$$\begin{aligned} \langle |V(\mathbf{u})|^2 \rangle &\propto \int d^2\mathbf{u}' \int d^2\mathbf{u}'' \langle \tilde{T}(\mathbf{u}') \tilde{T}^*(\mathbf{u}'') \rangle \tilde{A}(\mathbf{u} - \mathbf{u}') \tilde{A}(\mathbf{u}' - \mathbf{u}'') \\ &\propto \int d^2\mathbf{u}' C(\mathbf{u}') |\tilde{A}(\mathbf{u} - \mathbf{u}')|^2 \\ &\propto C(\mathbf{u}') \int d^2\mathbf{u}' |\tilde{A}(\mathbf{u} - \mathbf{u}')|^2, \end{aligned} \quad (4.0.9)$$

where the last line is a reasonable approximation if the power spectrum is smooth and independent of \mathbf{u}' .

The primary beam, A , is often modelled as a Gaussian, so this can be substituted in eq. 4.0.9 and then solved to produce the final relation;

$$\begin{aligned} C^{\text{obs}}(\mathbf{u}) \sim \langle |V(\mathbf{u})|^2 \rangle &\propto C(\mathbf{u}) \int d^2\mathbf{u}' |\tilde{A}(\mathbf{u} - \mathbf{u}')|^2 \\ &\approx C(\mathbf{u}) \int d^2\mathbf{x} |A(\mathbf{x})|^2 \\ &\approx C(\mathbf{u}) \int_0^\infty d^2\mathbf{x} (e^{-\frac{x^2}{2\sigma^2}})^2 \\ &\approx \pi\sigma^2 C(\mathbf{u}) \end{aligned} \quad (4.0.10)$$

This is an exact result when $C(\mathbf{u}')$ is independent of \mathbf{u}' . Modelling the beam as a Gaussian gives

$$\sigma = \frac{\theta_{\text{FWHM}}}{\sqrt{8\ln 2}}. \quad (4.0.11)$$

By dividing the power spectrum obtained from the visibilities, C^{obs} , by the factor $\pi\sigma^2$ we should be able to recover the true power spectrum, C , that was used as

the input.

The C_ℓ s are directly related to the visibilities (see also eq. 4.0.10) via

$$C_\ell = \left(\frac{dB}{dT} \right)^{-2} \frac{\sum_{\text{bin}} |V|^2}{N}, \quad (4.0.12)$$

where the numerator is the sum of the squared visibilities in a bin and the denominator is the number of visibilities in a bin. The factor at the front is used to convert visibilities from Jansky, Jy, to Kelvin, K. Since we are working in the Rayleigh-Jeans limit this is given by

$$\frac{dB}{dT} = \frac{2k_B}{\lambda^2}. \quad (4.0.13)$$

4.1 Error on Power Spectrum

There are several sources of statistical error on a measurement of the power spectrum. The overall error can be written as

$$\Delta C_\ell \sim \sqrt{\frac{2}{2\ell + 1}} (C_\ell + N_\ell). \quad (4.1.1)$$

The first term in eq. 4.1.1 is the cosmic variance due to the fact it is only possible to observe one realisation of the Universe. From eq. 4.0.2 we can see that there are $(2\ell + 1)$ $a_{\ell m}$ s for each ℓ , each having an expected autocorrelation of C_ℓ . This means there are only a finite number of independent modes that can be measured in a given cosmic volume. Cosmic variance is much bigger for small ℓ than large ℓ . Another problem arises when small patches of sky are used to measure C_ℓ , when the spherical harmonics cover the whole sphere (Gawiser and

Silk, 2000). This limited sky coverage leads to sample variance given by

$$\sigma_{sv}^2 \sim \left(\frac{4\pi}{\Omega} \right) \sigma_{cv}^2, \quad (4.1.2)$$

where Ω is the solid angle of sky observed (Scott et al., 1994). This causes errors at low ℓ to be very large if just one field is being observed as only a few fluctuations are being measured.

The second term, N_ℓ in eq. 4.1.1 is made up of shot noise and other sources of error such as telescope noise.

Shot noise is a result of the imperfect sampling of fluctuations due the finite number of galaxies in the given volume. It is equal to the survey area solid angle divided by the number of observed galaxies within that area (Wolz et al., 2013).

The final source of error for radio interferometric observations is the thermal noise. This can be expressed in terms of brightness temperature as (Thompson et al., 1986)

$$\sigma_{th}^2 = \frac{\lambda^2 T_{sys}}{A_{eff} \Omega \sqrt{N(N-1)} \sqrt{\Delta\nu t_{int}}}, \quad (4.1.3)$$

where T_{sys} is the system temperature, A_{eff} is the effective collecting area, Ω is the beam solid angle, N is the number of antennas and t_{int} is the integration time per pixel.

4.2 Binning Visibilities

For interferometers, the total number of visibilities at each frequency can be very large. It is therefore necessary to compress the data by binning the visibilities at each observing frequency into cells in the uv -plane. As the main focus is estimating the power spectrum rather than making accurate maps, the uv -plane can simply be divided up into cells (pixels) of equal area with sides Δu . Within each pixel the

visibility is assumed to be constant. The value of the binned visibility, v_k , in the k th cell is usually associated with the position in the uv -plane \mathbf{u}_k corresponding to the centre of the cell. The choice of Δu is a compromise between accurately representing the original data with the binned data (small Δu) and speeding up the calculation by using fewer data points (large Δu).

The correlation length in the uv -plane is governed by the primary beam so the cells should be of order this size so as not to lose too much information (sampling theorem). Cells of size Δu were then chosen according to

$$\Delta u = \Delta v = \frac{1}{2R_c}, \quad (4.2.1)$$

where R_c is defined as the radius at which the primary beam drops to 1% of its peak value (Hobson et al., 1995). This is about three times the dispersion for a Gaussian beam, where the dispersion is given by $\theta_{FWHM}/\sqrt{8 \ln 2}$.

4.2.1 Expected Power Spectrum and Variance

In order to compute the angular power spectrum, both an incoherent and a coherent addition of visibilities is needed. The relative contribution of incoherent and coherent additions depends on the number of visibilities within each uv -cell and the number of uv -cells within each ℓ -bin. Both extreme cases (completely incoherent or completely coherent) and the intermediate case will be looked at to see how the binning affects the final power spectrum result.

Visibilities can be considered coherent over scales that are of similar size to $1/\text{FOV}$ in the uv -plane. The estimate for the angular power spectrum for mode ℓ is given by

$$C_\ell = \frac{\sum_{(uv) \in \ell} N_{uv} |V_{uv}|^2}{\sum_{(uv) \in \ell} N_{uv}}, \quad (4.2.2)$$

where N_{uv} is the number of visibilities in a given uv -cell and the sum is over the uv -cells contributing to that ℓ -mode (Trott et al., 2012). The visibilities, V_{uv} , are coherently combined (averaged) within each cell but the final estimate associating uv -cells in ℓ -modes is incoherent (the visibilities are combined after squaring).

An entirely coherent estimate of the power spectrum is where a single ℓ -mode consists of a single uv -cell ($N_\ell = N_{uv}$). In this case the summations in eq. 4.2.2 are omitted giving,

$$C_\ell = |V_{uv}|^2, \quad (4.2.3)$$

as the new power spectrum estimate. The mean and variance for complex Gaussian white noise on each visibility can be computed giving,

$$C_\ell \sim \mathcal{N}\left(\frac{\sigma^2}{N_\ell}, \frac{2\sigma^4}{N_\ell^2}\right), \quad (4.2.4)$$

where N_ℓ is the number of visibilities in a given ℓ -mode (Trott et al., 2012). It is clear from eq. 4.2.4 that as the number of visibilities increases the expected noise power and variance decrease, however the ratio of expected noise to standard deviation stays the same.

The opposite case is an entirely incoherent estimate where a single visibility contributes to each uv -cell ($N_{uv} = 1$). The power spectrum estimate is now,

$$C_\ell = \frac{\sum_{i=1}^{N_\ell} |V_i|^2}{N_\ell}, \quad (4.2.5)$$

giving,

$$C_\ell \sim \mathcal{N}\left(\sigma^2, \frac{2\sigma^4}{N_\ell}\right). \quad (4.2.6)$$

A real experiment however will have a large number of visibilities coherently combined with many uv -cells contributing to each ℓ -mode, as described in eq.

4.2.2. For example, consider an experiment with an equal number of visibilities in each uv -cell and ten uv -cells contributing to each ℓ -mode, $N_\ell = 10N_{uv}$, the power spectrum estimate would then be written as,

$$C_\ell = \frac{\sum_{i=1}^{10} N_{uv} |V_{uv}|^2}{\sum_{i=1}^{10} N_{uv}}. \quad (4.2.7)$$

From this we get the following estimates for the expected noise power and variance;

$$C_\ell \sim \mathcal{N} \left(\frac{\sigma^2}{N_{uv}}, \frac{2\sigma^4}{N_\ell N_{uv}} \right). \quad (4.2.8)$$

Some simple noise simulations were used to test eq. 4.2.1, which is theoretically the optimum bin spacing in the uv -plane, and the results can be seen in Fig. 4.1.

Fig. 4.1 shows the recovered power spectrum for various bin widths. The input power spectrum used was the Millennium simulation with some low levels of noise added. To see the effects of the binning more clearly, both the Millennium simulation without noise, and the noise only power spectrum have been calculated using the incoherent estimator. These are represented on the plot by the solid black and blue lines respectively. The noise only gets averaged down in the uv -cells when the real and imaginary values are binned so making the cells bigger means that the noise gets averaged down more, which is seen in Fig. 4.1. The figure shows that $\Delta u = 1\lambda$ has started to average the noise down. The effect is not very big because as Δu gets smaller, the estimator tends towards the incoherent estimate of the noise (solid blue line), which is what is seen. Using $\Delta u = 5\lambda$ has reduced the noise levels quite dramatically but not enough to start seeing the signal through the noise. $\Delta u = 20\lambda$ has reduced the noise levels even further but some signal also seems to have been smoothed out at low ℓ . This is illustrated by the fact that the final power spectrum using $\Delta u = 20\lambda$ is lower than the Millennium signal

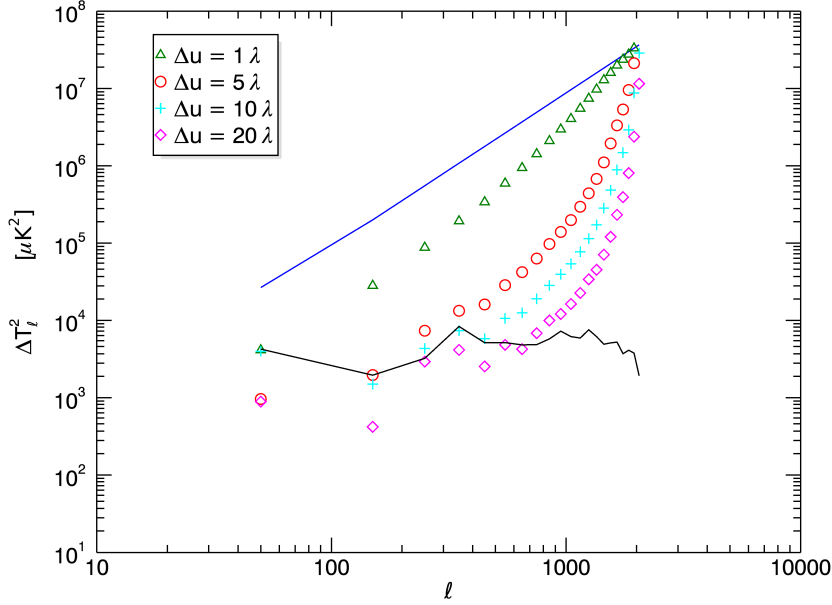


Figure 4.1: *Recovered power spectrum comparing the effect of different values of Δu on the Millennium simulation power spectrum with low levels of noise. The lower and upper lines represent the signal only and noise only power spectra computed using the incoherent estimator for comparison. $T_{sys}^* = 0.94K$ was used in the noise plots and all the power spectra were computed at $f = 1000$ MHz using $\Delta f = 5$ MHz.*

power spectrum (black line) up to $\ell = 1000$. The power spectrum calculated using $\Delta u = 10\lambda$ seems to agree with the signal power spectrum closely up until $\ell \sim 500$ indicating that the noise has been sufficiently averaged down to start revealing the signal. This suggests that using Δu around 10λ is an optimum value to choose, agreeing with eq. 4.2.1. Using $T_{sys}^* = 0.94$ K is equivalent to an observation time of 12000 hours for a Tianlai-like array. The antenna temperature can be increased in future simulations to simulate shorter observation times (see Section 3.3.1).

Fig. 4.2 shows the effect of the different estimators on power spectra consisting of just the Millennium simulation signal (left plot) and for a noise only simulation

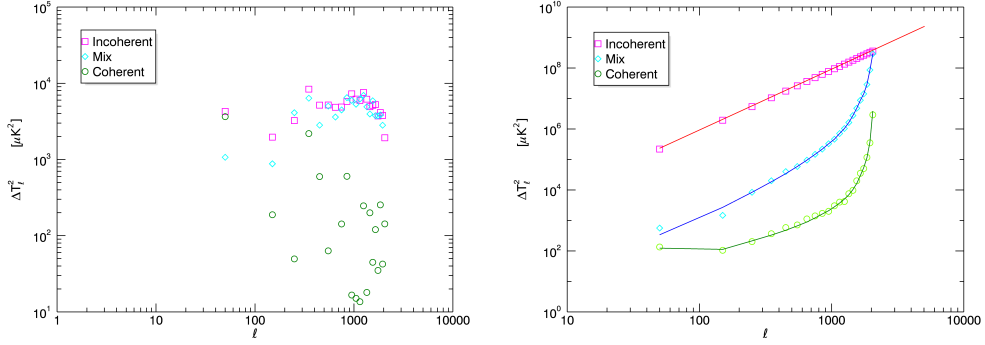


Figure 4.2: Recovered power spectra estimates using the three different estimators described by equations 4.2.5, 4.2.2 and 4.2.3. Left: Millennium simulation. Right: Noise ($T_{sys} = 3$ K). The theoretical power spectra have been plotted for comparison using equations 4.2.6, 4.2.8 and 4.2.4. All power spectra were calculated at $f = 1000$ MHz using $\Delta\ell = 100$. For the mix of coherent and incoherent binning $\Delta u = \Delta v = 10$ was used.

(right plot). Using $\Delta u = 10\lambda$ greatly reduces the noise levels whilst producing a signal power spectrum very similar to that found when using an entirely incoherent estimator, implying this is a reasonable choice of Δu . Although using the fully coherent power spectrum averages down the noise even further, it is obvious that if Δu gets too large then the signal is averaged out by binning and the signal power spectrum is no longer an accurate representation of the input.

Increasing the effective system temperature, T_{sys}^* , increases the overall amplitude of the noise significantly meaning that the signal cannot immediately be seen in the power spectrum for noise plus signal, unlike the case in Fig. 4.1. In order to recover the signal the noise needs to be subtracted. Fig. 4.2 showed that the theoretical noise and recovered noise power spectra agreed well, allowing the theoretical noise power spectra to be used in the noise subtraction later.

4.3 Testing the Incoherent Estimator

It has been shown that the correct estimator for signal only is the incoherent estimator, where a single visibility contributes to each uv -cell i.e. $N_{uv} = 1$ (see section 4.2.1). As this will be used fairly frequently it is important to test that it works for a range of test power spectrum before any real analysis is done using it.

We can use a variety of different power laws to see how well the incoherent estimator works. This takes the general form

$$T_\ell^2 = 100\mu K^2 \left(\frac{\ell}{100} \right)^n, \quad (4.3.1)$$

where $n = \pm 0.5, \pm 1.0$ and ± 2.0 will be the power spectra tested. A power spectrum with $n = +2$ is equivalent to white noise. A `HEALPix` (Górski et al., 2005) subroutine, `synfast`, can then be used to simulate a sky temperature map using a given set of C_ℓ values. The resulting temperature maps are shown in Figs. 4.3 and 4.4. From these maps, an area of 16 deg^2 was chosen and a FITS cube was created to be used by AIPS to produce a set of visibilities which in turn can be used to compute the power spectrum (see Section 3.3 for more information). To build up statistics, many Monte Carlo realisations of the sky were done.

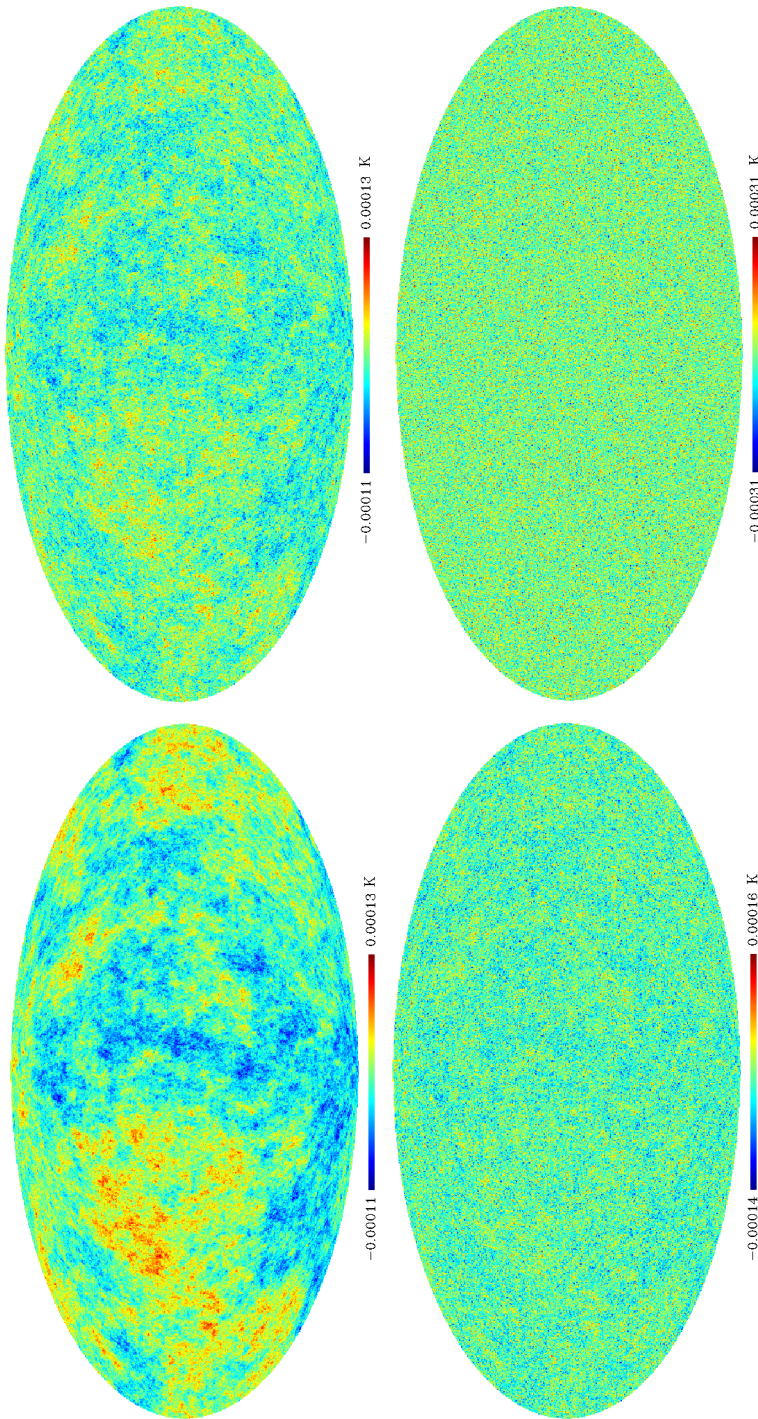


Figure 4.3: Mollweide projection of temperature maps created using $T_\ell^2 = 100(l/100)^n$, where $n = 0, 0.5, 1, 2$ corresponding to top left, top right, bottom left and bottom right. Temperature scale is in units of K.

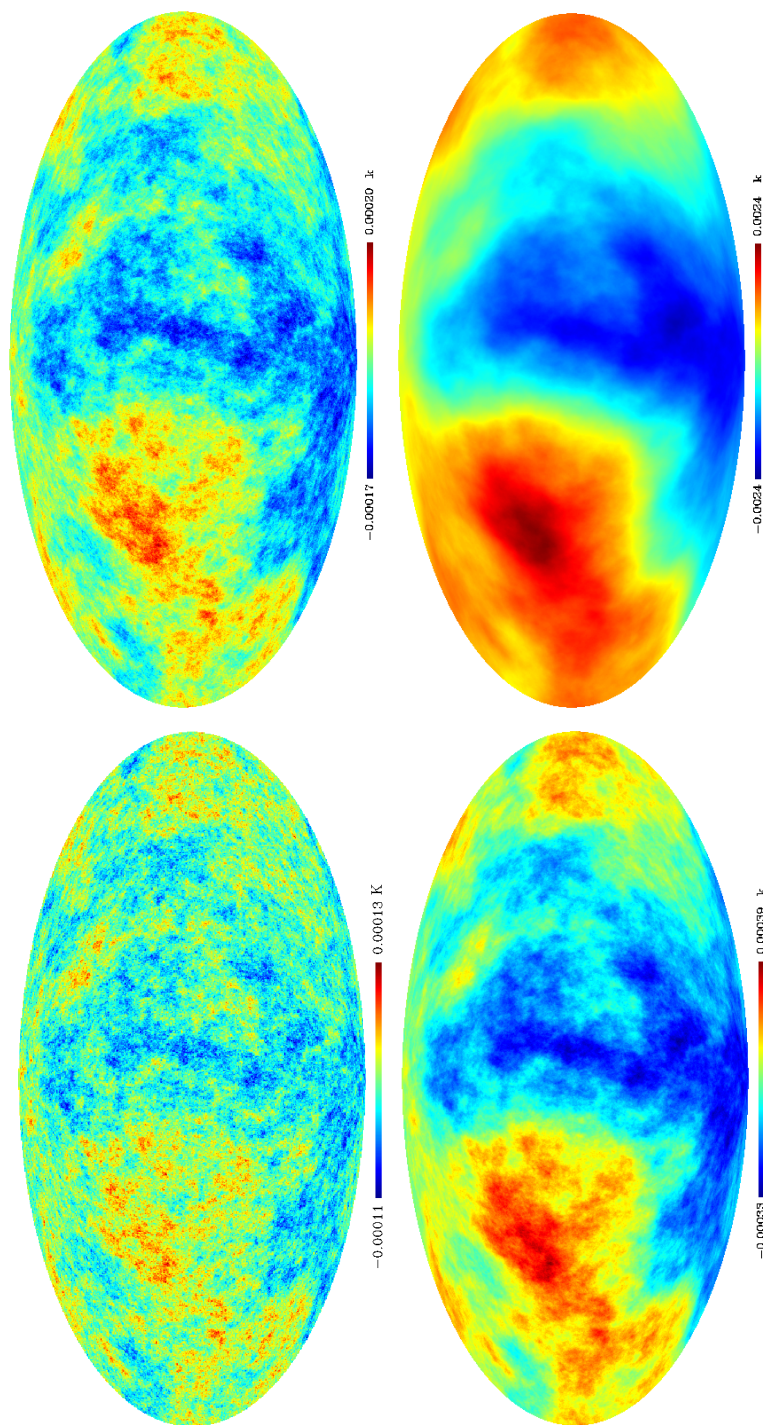


Figure 4.4: Mollweide projection of temperature maps created using $T_l^2 = 100(l/100)^n$, where $n = 0, -0.5, -1, -2$ corresponding to top left, top right, bottom left and bottom right. Temperature scale is in units of K.

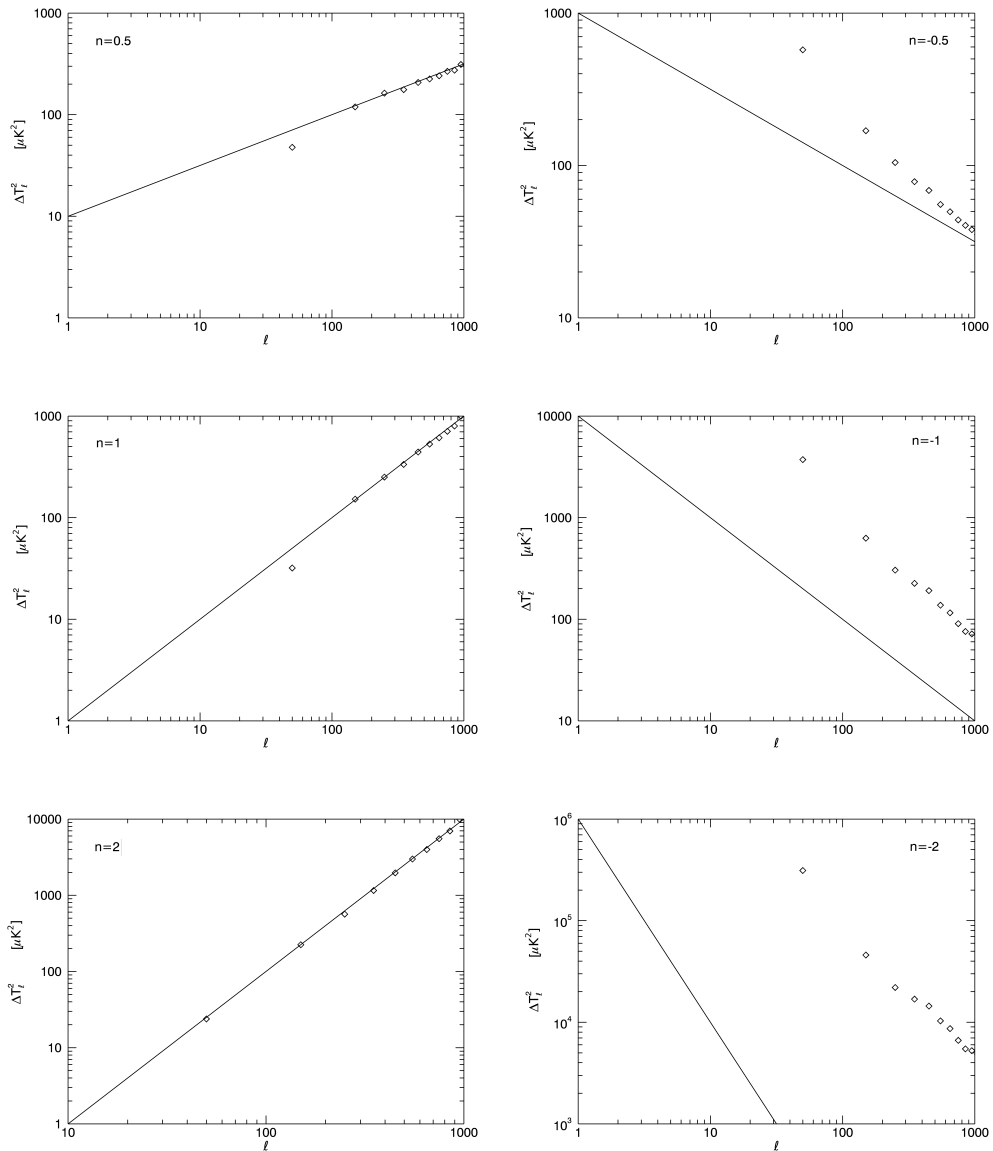


Figure 4.5: *Recovered power spectra for a variety of input power laws using the incoherent estimator. Results for positive power laws are on the left and negative power laws are shown on the right, all centred at $f = 1000$ MHz using $\Delta f = 5$ MHz.*

During the power spectrum analysis, shown in Fig. 4.5, using the incoherent estimator it was noticed that there was some significant bias for $n < 0$, getting

worse the more negative the exponent. To see why, the uv maps of the AIPS data were compared, shown in Fig. 4.6.

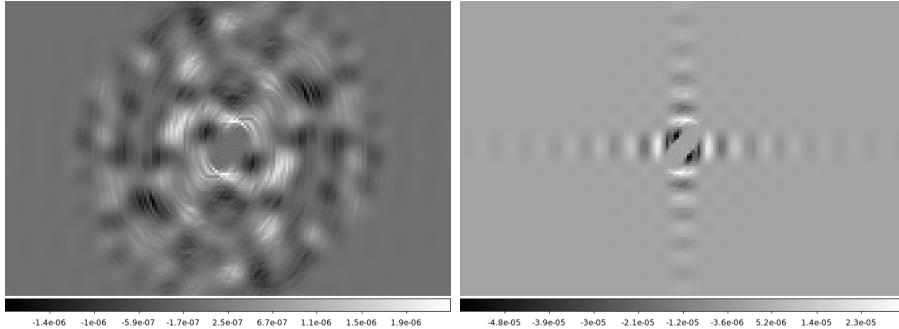


Figure 4.6: UV maps for $n = +2$ and $n = -2$ power laws shown in the left and right plots respectively.

For a Gaussian random field we expect random Gaussian fluctuations with the variance in rings which is seen in the left map in Fig. 4.6. The $n = -2$ map has most of the power concentrated in two vertical and horizontal stripes. A power spectrum with exponent $n = -2$ means that there is lots of power on large scales so removing the largest modes should fix the problem. There is lots of power at the edge of the map because the primary beam does not go to zero. A solution would be to apodize the edge of the map with a cosine function which would force it to go to zero at the edge.

The uv map and power spectrum in Fig. 4.7 show that a wide field of view with a cosine taper has got rid of the two stripes of power that dominated the map previously, giving a better recovery of the input power spectrum. The faint rings visible in the uv map are below the noise levels of any practical interferometer simulation so will not be a problem in future simulations.

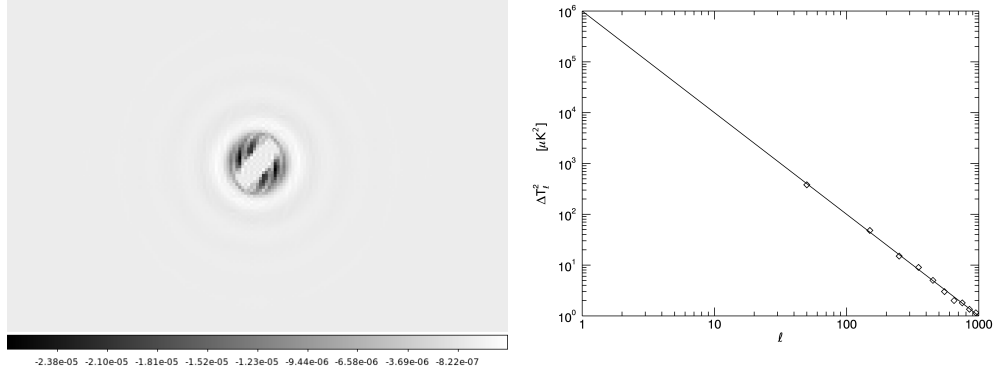


Figure 4.7: *UV map (left) and recovered power spectrum (right) for -2.0 input power law using the incoherent estimator, corrected using a cosine taper, centred at $f = 1000$ MHz using $\Delta f = 5$ MHz.*

4.4 Bias Correction

For any array configuration being used it is unlikely that the power spectrum produced from the visibilities will be exactly the same as the power spectrum that is being observed. For noise only, the correct method is to use an entirely coherent estimate of the power spectrum where a single ℓ -mode consists of a single uv -cell ($N_\ell = N_{uv}$), as seen in eq. 4.2.3. For signal only an entirely incoherent estimate is used where a single visibility contributes to each uv -cell ($N_{uv} = 1$), as seen in eq. 4.2.5. The C_ℓ estimators used for signal only and noise only are therefore different. We have seen that when a simulation combines both signal and noise the estimator used needs to be a compromise between the two methods.

As a result of the compromise there is likely to be some noise bias intrinsic to the model being used and preventing the signal from being recovered perfectly. However, it should be possible to find a function, F_ℓ , for each ℓ -mode to quantify the bias for a particular model;

$$T_\ell^{\text{obs}} = F_\ell T_\ell^{\text{true}} + N_\ell^{\text{true}}, \quad (4.4.1)$$

where T_ℓ^{obs} is the observed power spectrum, and T_ℓ^{true} and N_ℓ^{true} are the true signal and noise power spectra respectively. F_ℓ can be found by observing a known input signal with no noise ($T_{\text{sys}}^* = 0$ K) and dividing the observed output by the input. F_ℓ will then tell us by how much we need to correct the observed output power spectrum in order to reproduce what the original input was for the particular model.

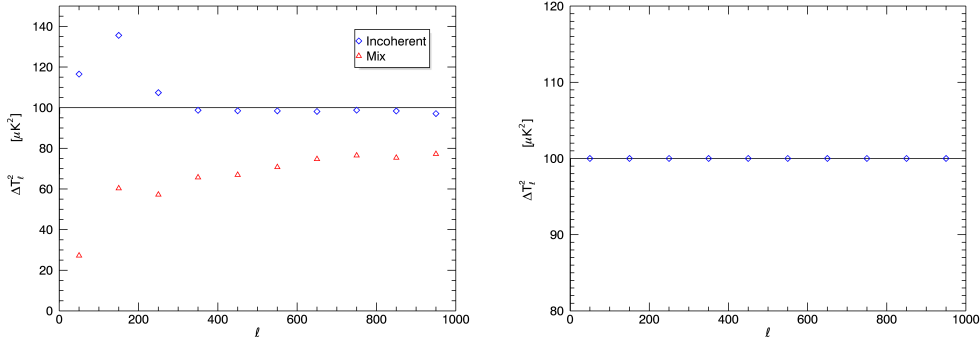


Figure 4.8: *Calculating F_ℓ for a Tianlai-like array configuration. In the left plot, the solid line represents the input power spectrum used, while the data points represent the recovered power spectrum using various estimators. The right plot shows the output power spectrum once the F_ℓ correction has been applied. Power spectra were computed at $f = 1000$ MHz using $\Delta f = 5$ MHz.*

The left plot in Fig 4.8 illustrates the differences between two C_ℓ estimators that can be used to calculate the power spectrum. The solid line represents the input power spectrum that was used which has a constant $T_\ell = 100 \mu\text{K}^2$. The diamonds show the resulting power spectrum using the completely incoherent estimator while the triangles show results for the mix of coherent and incoherent estimators with $\Delta u = 10\lambda$. It is clear that the correct binning method for signal (entirely incoherent) reproduces the input power spectrum fairly well, while much more signal is averaged down when a mix is used. We can divide the resulting power spectrum for the mixed estimator by the input to give F_ℓ which will tell us by how much we need to correct each ℓ -bin in order to get back what we started

with. To check that the F_ℓ found is correct, we can divide the output power spectrum by the correcting F_ℓ factor and we should be able to recover the input. The result of this can be seen in right plot in Fig. 4.8 and illustrates that we can now recover the input power spectrum correctly.

4.5 Autocorrelation versus Cross Correlation

4.5.1 Autocorrelation

It is now clear that in order to recover an accurate signal power spectrum, both an estimate of the noise power spectrum and F_ℓ are needed. We have already seen that

$$T_\ell^{\text{true}} = \frac{1}{F_\ell} (T_\ell^{\text{obs}} - \langle N_\ell^{\text{est}} \rangle), \quad (4.5.1)$$

where the theoretical noise power spectrum seen in Section 4.2.1 can be used for N_ℓ^{est} . Instead of just subtracting off the noise power spectrum we can also correct for the signal lost during binning to leave behind a more accurate recovery of the signal power spectrum. The results of this are illustrated in the following plots.

Fig. 4.9 shows the results of two simulations with different noise levels. It is clear in both plots that there is still some noise bias at high ℓ . In order to check that this bias is a result of the noise in the simulation rather than the code itself some further investigation needs to be done. The noise levels in these plots are relatively high and there are only 80 realisations. By increasing either the number of noise realisations or decreasing the noise levels, the noise bias at high ℓ should go away. This was investigated and the results of these simulations are shown below.

Fig. 4.10 shows the results of increasing the number of realisations for a particular noise level. The top two images show the results obtained using two different

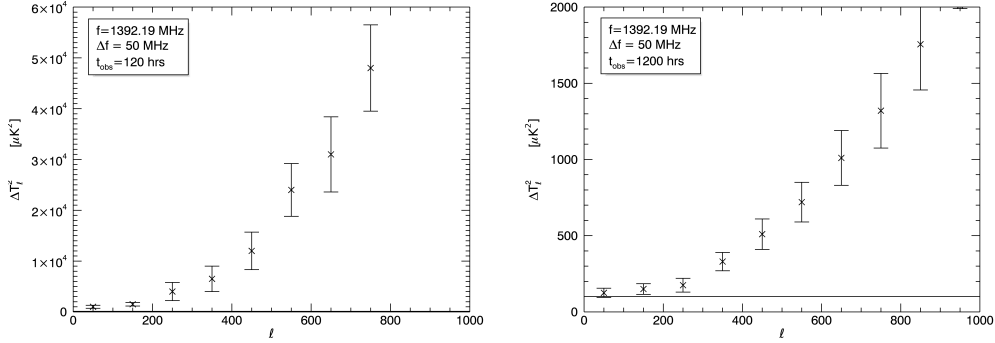


Figure 4.9: Plots showing the power spectra results for a Tianlai-like array configuration for $\ell = 0 - 1000$. Each power spectrum was centred at 1390 MHz using $\Delta f = 5$ MHz. The left plot shows results for an observation time of 120 hrs and the right is for 1200 hrs. In both plots, the solid line shows the power spectrum that is computed when only signal is observed ($T_{sys}^* = 0$ K). The data points in each plot represent the power spectrum of the signal that should be able to be seen once noise has been subtracted and corrections applied.

sample sets of 80 realisations. As noise is random, there is an equal chance of the recovered power spectrum having a bias above or below the input power spectrum. By combining many noise realisations, the overall amplitude of the bias should decrease as positive and negative contributions should cancel out. This is seen in the lower plot where all the realisations have been combined into one set.

Fig. 4.11 shows the results of decreasing the noise levels. The left and right plots used $T_{sys}^* = 0.3$ K and $T_{sys}^* = 0.094$ K respectively. It can be seen clearly that the noise bias has high ℓ has been reduced and is smallest for the observation with the lowest noise.

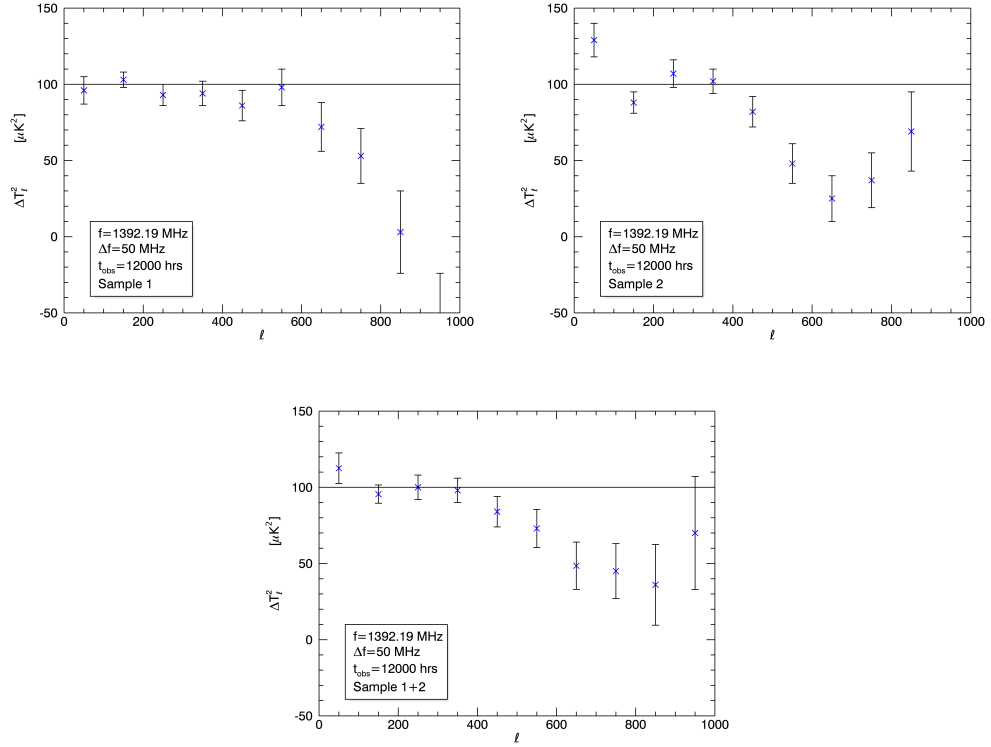


Figure 4.10: *Recovered power spectra for a Tianlai-like array configuration. Each power spectrum was centred at 1390 MHz using $\Delta f = 5$ MHz. Both the top plots show results for an observation time of 12000 hrs with the left and right plots showing results for two separate sample sets. The lower plot shows the results of these two batches combined. In all plots, the solid line shows the power spectrum that is computed when only signal is observed ($T_{\text{sys}}^* = 0$ K). The data points in each plot represent the power spectrum of the signal that should be able to be seen once noise has been subtracted and corrections applied.*

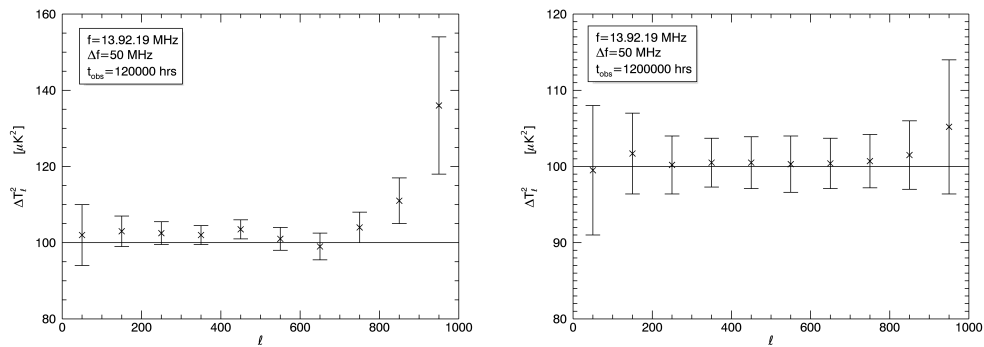


Figure 4.11: *Recovered power spectra for a Tianlai-like array configuration. Each power spectrum was centred at 1390 MHz using $\Delta f = 5$ MHz. The left plot shows results for an observation time of 120000 hrs and the right is for 1200000 hrs. In both plots, the solid line shows the power spectrum that is computed when only signal is observed ($T_{sys}^* = 0$ K). The data points in each plot represent the power spectrum of the signal that should be able to be seen once noise has been subtracted and corrections applied.*

4.5.2 Cross Correlation

Previously, in order to calculate the power spectrum from a set of visibilities the estimator has included a mix of incoherent and coherent binning of visibilities from which a noise estimate was subtracted. This approach is known as autocorrelation. However, it has been shown in Section 4.5.1 that there seems to be some noise bias with this method. This is demonstrated in signal recovery plots where at high ℓ the power spectrum seems to have an upwards trend to it. This is likely to be due to the noise being incorrectly estimated and therefore not subtracted perfectly. The noise estimate is based on simulations so is not exact, leaving some residual noise bias behind. In order to get rid of this a method is needed which doesn't rely on using the simulations to come up with a noise estimate and doesn't rely on subtracting a noise estimate from the signal power spectrum.

One way of getting round this problem is to use cross-correlation rather than autocorrelation. A problem with autocorrelation is that the noise power spectrum tends to add some signal and uncertainty to the overall power spectrum. Cross-correlation solves this problem because the cross-correlation of random noise visibilities averages to zero which leaves only the uncertainty behind. This should eliminate the problem of the noise bias in the power spectrum calculations.

Three different methods of cross correlating visibilities were investigated and then from these three the most successful one was chosen to be used for further work.

The first method is similar to the old method in that initially the visibilities are binned into uv -cells. Instead of then averaging these visibilities within each uv -cell, all the visibilities contributing to a particular uv -cell are cross correlated with each other. Once this has been done, the values of the overall visibility for each uv -cell are then combined in ℓ using the same method as before. The equation

for this can be written as

$$C_\ell = \frac{\sum_{(uv) \in \ell} N_{uv} \left(\frac{\sum_{i \neq j}^{N_{uv}} V_i V_j^*}{N_{uv}^2 - N_{uv}} \right)}{\sum_{(uv) \in \ell} N_{uv}}, \quad (4.5.2)$$

where V_i and V_j are individual visibilities in uv -cells, N_{uv} is the number of visibilities in a uv -cell, the internal sum is over the total number of visibilities in a uv -cell and the outside sum is over uv -cells contributing to each ℓ -bin.

An alternative method is very similar to the original autocorrelation method in that the visibilities are binned and averaged within uv -cells. These averages are then cross correlated with each other within ℓ -modes, which can be written as

$$C_\ell = \frac{\sum_{i \neq j}^N (V_{uv,i} V_{uv,j}^*)}{N^2 - N}, \quad (4.5.3)$$

where V_{uv} is the average visibility within a uv -cell, N is the number of uv -cells in an ℓ -mode and the sum is over the number of uv -cells contributing to a particular ℓ .

The last cross correlation estimator is similar to the incoherent estimator in that the visibilities are not binned in the uv -plane at all, just in ℓ . All the visibilities in each ℓ are then cross correlated with each other giving

$$C_\ell = \frac{\sum_{i \neq j}^{N_\ell} (V_i V_j^*)}{N_\ell^2 - N_\ell}, \quad (4.5.4)$$

where $V_{i,j}$ are individual visibilities in ℓ , N_ℓ is the number of visibilities in each ℓ -mode and the sum is over the total number of visibilities in each ℓ .

Various noise only simulations were investigated using the various cross correlation methods and the results are shown in the following plots.

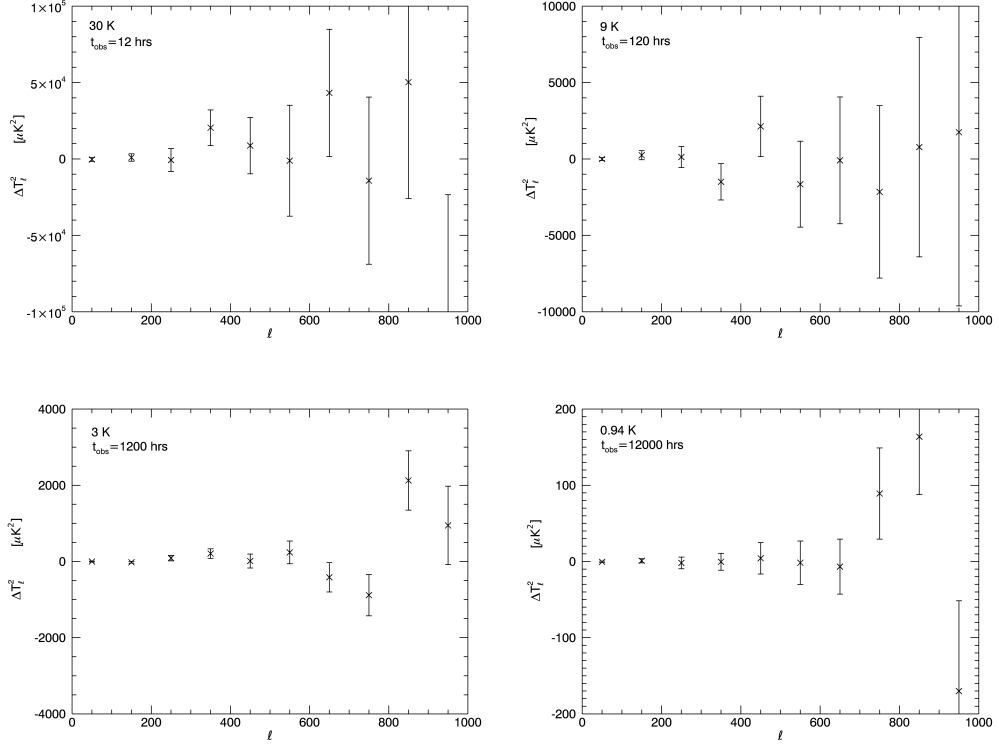


Figure 4.12: Results of cross correlating visibilities within each uv-cell (see eq. 4.5.2) for the following noise levels: 30 K, 9 K, 3 K and 0.94 K. Each power spectrum was calculated using $\Delta f = 5$ MHz at $f = 1390$ MHz.

Figs. 4.12, 4.13 and 4.14 show the recovered power spectra for different levels of noise, using different cross correlation estimators. Cross correlating visibilities before averaging produces final power spectra that are consistent with zero, with data points evenly distributed above and below the zero line which is expected for random noise. The two methods of cross correlation after averaging and within ℓ -bins produces power spectra that appear to suffer from some noise bias at high ℓ . When cross correlation after averaging is used, the effect of the bias is reduced as the noise levels are reduced. Bias appears to be present regardless of noise levels

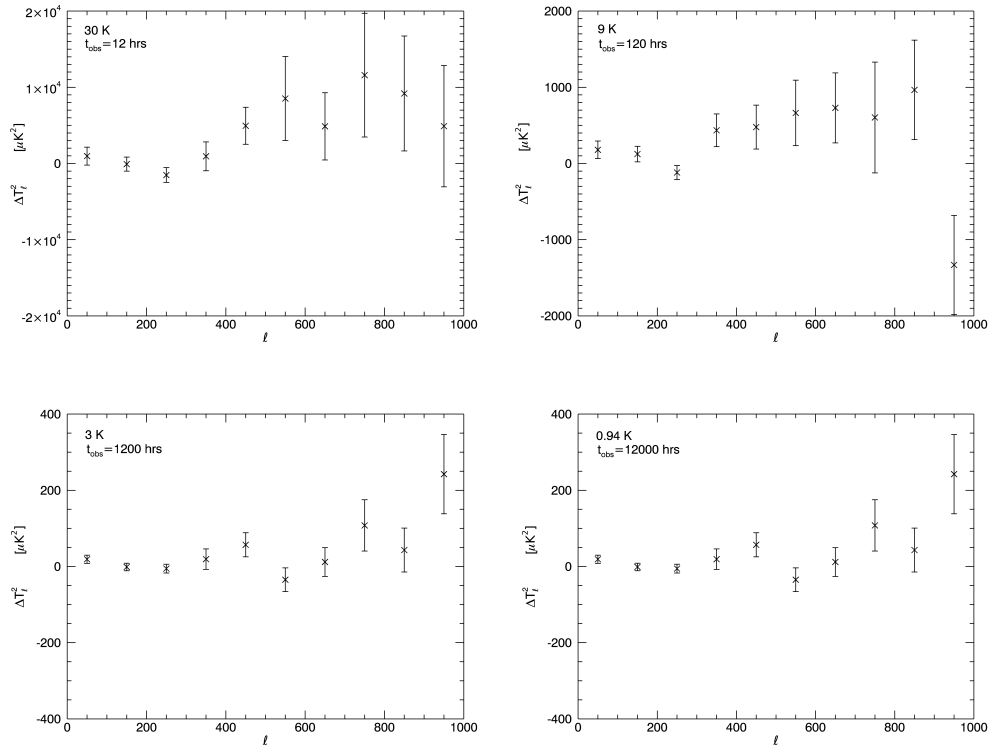


Figure 4.13: Results of cross correlating visibilities after they have been averaged within each uv -cell (see eq. 4.5.3) for the following noise levels: 30 K, 9 K, 3 K and 0.94 K. Each power spectrum was calculated using $\Delta f = 5$ MHz at $f = 1390$ MHz.

for cross correlation within ℓ -bins. It is therefore clear from these three plots that cross correlating visibilities within uv -cells before averaging is the best choice of estimator for noise simulations.

Although cross-correlation before averaging produced the best results for noise only simulations, it is important to understand how the estimators will affect the signal. Ideally, the cross correlation method won't affect the signal so that only the noise is averaged down with no compromise on signal. A constant power spectrum of $T_\ell^2 = 100 \mu\text{K}^2$ will be briefly investigated.

Fig. 4.15 shows the results of the known input power spectrum $T_\ell^2 = 100 \mu\text{K}^2$

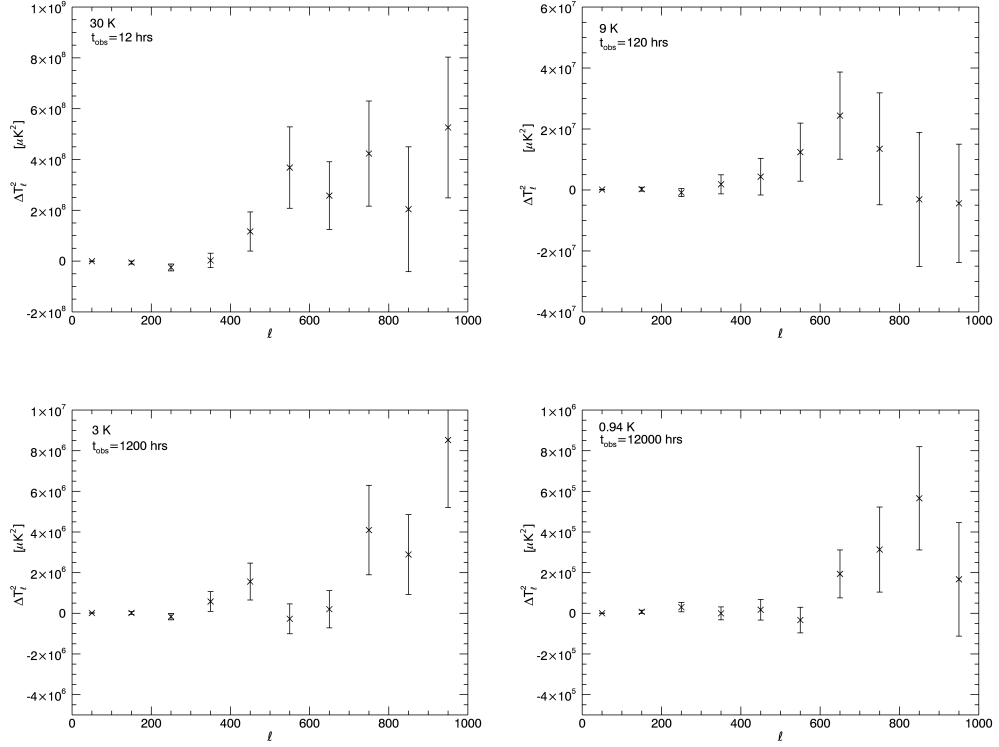


Figure 4.14: Results of cross correlating visibilities within each ℓ bin (see eq. 4.5.4) for the following noise levels: 30 K, 9 K, 3 K and 0.94 K. Each power spectrum was calculated using $\Delta f = 5$ MHz at $f = 1390$ MHz.

computed using different estimators. Estimators using cross correlation before and after averaging have been plotted as well as the old autocorrelation and incoherent method for comparison. The incoherent estimator recovers the input power spectrum most accurately, as expected as it has already been shown that this is the correct method for signal. From the plot it can be seen that the estimators using autocorrelation and cross correlation before averaging (eq. 4.5.2) produce very similar results while cross correlating visibilities after averaging (eq. 4.5.3) results in most of the signal being smoothed out. Although some signal is being averaged down in most methods the estimator using cross correlation before averaging is much better for noise only simulations as it does not suffer from a bias at high

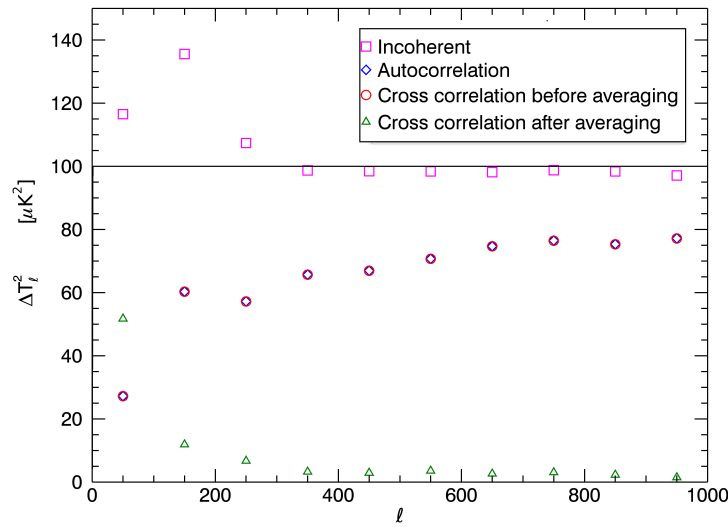


Figure 4.15: Power spectrum computed for $\Delta T_\ell^2 = 100 \mu\text{K}^2$ with no noise using different estimator methods. Each power spectrum was calculated using $\Delta f = 5 \text{ MHz}$ at $f = 1000 \text{ MHz}$.

ℓ . It is therefore clear that for more realistic simulations which will include signal and noise, this cross correlation method is the optimal power spectrum estimator.

Fig. 4.15 can also be used to calculate F_ℓ for a constant input power spectrum using the cross correlation method, using the ratio of the power spectrum calculated using the cross correlation method and the known input power spectrum. The following plots show the results of using F_ℓ to recover the input signal.

Fig. 4.16 shows the results of using F_ℓ to recover the input power spectrum when different levels of noise have been added. Looking at the plots the results for each noise simulation are consistent with the input power spectrum of $100 \mu\text{K}^2$ as the cross correlating of visibilities has averaged down the noise. There is some scatter around the input value which is to be expected with random noise.

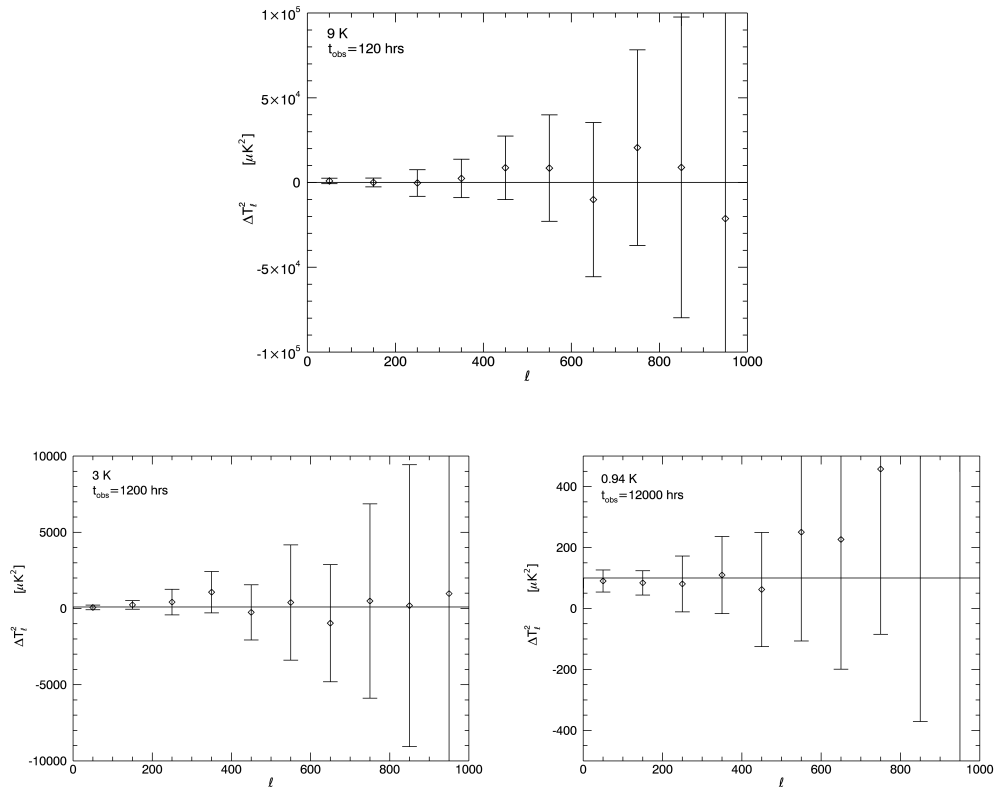


Figure 4.16: Results of cross correlating visibilities within each uv -cell for a known power spectrum $\Delta T_\ell^2 = 100 \mu K^2$ and different levels of noise: 9 K, 3 K and 0.94 K. Each power spectrum was calculated using $\Delta f = 5$ MHz at $f = 1000$ MHz.

Chapter 5

Measuring the HI Power Spectrum

The previous Chapter investigated different C_ℓ estimators, concluding that the best estimator was the cross-correlation of visibilities. This involved binning and averaging visibilities within uv -cells and then cross-correlating the averages with each other within ℓ -bins. A drawback of this method was that it relied on a correction factor F_ℓ being calculated to recover the power spectrum accurately, and this factor depended on the input power spectrum. Despite this, the method was chosen as it eliminated the problem of noise bias which was present with other estimators.

Some initial analysis on the Millennium simulation was undertaken in Chapter 3 to see how each interferometer performed at different frequencies. We would like to use the Millennium simulation again to see how well each interferometer can recover the HI power spectrum, but a problem lies with calculating F_ℓ . The exact power spectrum for the Millennium simulation is unknown meaning that the F_ℓ needed to correct the recovered power spectrum is also unknown. As this correction is an important step in recovering the power spectrum a suitable F_ℓ

needs to be chosen. To get round this we can plot a theoretical HI angular power spectrum and use this to find an F_ℓ that should most closely match that of the Millennium simulation. This Chapter will focus on finding a suitable F_ℓ based on theory, and then using this theoretical power spectrum as in input to compare how well the interferometers can recover the HI power spectrum.

5.1 Input Power Spectrum

To model the 21 cm angular power spectrum we shall use the formula given by Battye et al. (2013)

$$C_\ell = \frac{H_0 b^2}{c} \int E(z) \left[\frac{W(z) \bar{T}(z) D(z)}{r(z)} \right]^2 P_{\text{cdm}} \left(\frac{\ell + \frac{1}{2}}{r(z)} \right) dz, \quad (5.1.1)$$

where $E(z) = H(z)/H_0$, $H(z) = H_0(1+z)\sqrt{1+\Omega_0 z}$ and $D(z)$ is the growth function with $D(0) = 1$. The projection of \bar{T} on the sky is defined by a kernel $W(z)$, which was chosen to be a top-hat in (Battye et al., 2013), giving

$$W(z) = \begin{cases} \frac{1}{z_{\text{max}} - z_{\text{min}}} & \text{if } z_{\text{min}} \leq z \leq z_{\text{max}}, \\ 0 & \text{otherwise.} \end{cases} \quad (5.1.2)$$

The maximum and minimum bin frequencies define the maximum and minimum redshifts of each bin so any weighting function could be used. The observed brightness temperature (\bar{T}) and comoving distance (r) are given by

$$\bar{T}(z) = 44 \mu\text{K} \frac{(1+z)^2}{E(z)}, \quad (5.1.3)$$

$$r(z) = c \int_0^z \frac{dz'}{H(z')}. \quad (5.1.4)$$

Details about the growth function, $D(z)$, and cold dark matter power spectrum,

P_{cdm} , can be found in Appendix B.

As a quick test of the code written to compute the HI angular power spectrum, figures 1 and 2 from Battye et al. (2013) were reproduced and can be seen below.

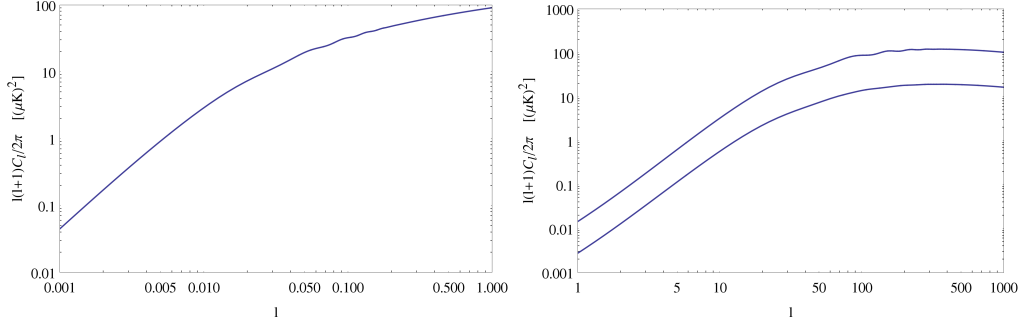


Figure 5.1: *Left: 3D HI power spectrum at $z = 0.28$. Right: HI angular power spectrum for two different frequency ranges 925-975 MHz (upper plot) and 800-1100 MHz (lower plot), centred on the same frequency of 950 MHz.*

The code can now be used to obtain the power spectrum for the frequency range of interest and the F_ℓ can then be deduced.

5.2 Finding F_ℓ for the HI Angular Power Spectrum

The plots in Fig. 5.2 show the power spectra for the central frequencies $f = 1000$ MHz and $f = 800$ MHz, using $\Delta f = 5$ MHz and no noise. In both plots the solid line represents the theoretical power spectrum calculated using (Battye et al., 2013). The data points show the power spectra recovered using several estimators; the incoherent estimator (diamonds) and the cross-correlation estimator (triangles). As we have seen before, it is necessary to find F_ℓ to correct the recovered power spectrum using cross-correlation as this estimator averages down the signal as well as the noise. As before, F_ℓ can be found by dividing the recovered cross-correlation power spectra by the input power spectrum. The results of this are

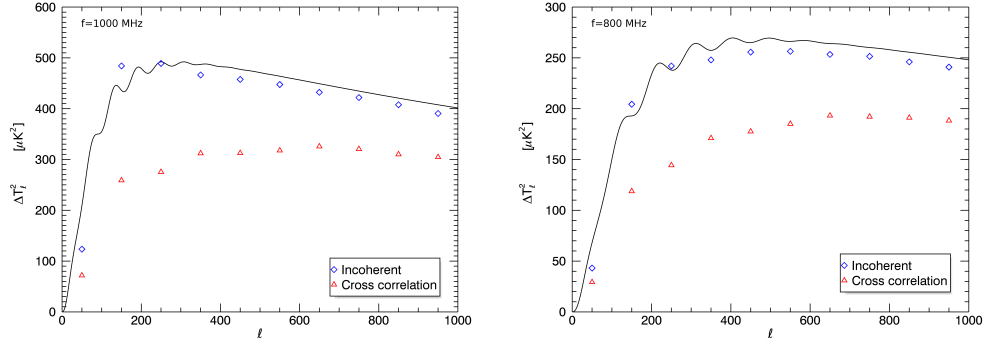


Figure 5.2: HI angular power spectrum for two frequencies; 1000 MHz (left) and 800 MHz (right). In each plot the solid line shows the power spectrum calculated from theory using $\Delta f = 5$ MHz. The data points represent the measured output power spectra using different estimators.

shown in Fig. 5.3.

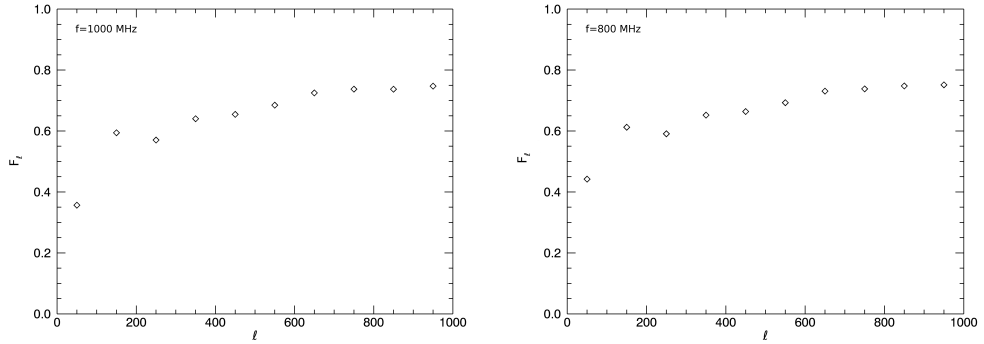


Figure 5.3: F_{ℓ} calculated for the HI power spectrum centred on $f=1000$ MHz (left) and $f=800$ MHz (right) using $\Delta f = 5$ MHz.

The F_{ℓ} for the HI angular power spectra are shown in Fig. 5.3. The general shape of the F_{ℓ} function is the same for both central frequencies. For both cases, as ℓ increases, F_{ℓ} tends to 1 meaning that the recovered power spectra are most similar to the input at high ℓ and that the largest correction is needed at low ℓ .

The HI power spectrum can be plotted for a variety of different 50 MHz bands. The results of this are shown in Fig. 5.4.

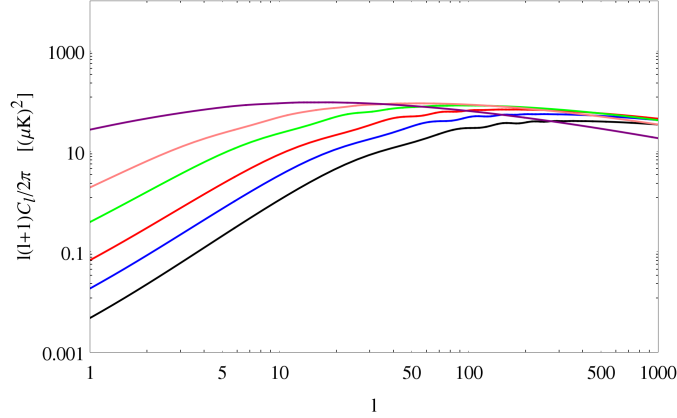


Figure 5.4: *How the HI angular power spectrum changes over a range of frequencies of 50 MHz bins. The frequencies plotted are 925-975, 1050-1100, 1150-1200, 1250-1300, 1310-1360 and 1368-1417 MHz from the lower to upper plots.*

It is clear that the HI power spectrum varies quite a lot over central frequencies ranging from $f = 950$ MHz (lowest power spectrum) to $f = 1392$ MHz (upper power spectrum). Fig. 5.4 highlights the need to find different F_ℓ s depending on the frequency range under consideration.

5.3 Recovering the HI Angular Power Spectrum

The following section will present the results of several simulations using the Battye et al. (2013) power spectrum as the input, with various noise levels for a Tianlai-like array. The cross-correlation estimator along with suitable F_ℓ s were used to recover the power spectrum the results of which can be seen in Fig. 5.5.

Fig. 5.5 demonstrates the reconstruction of the Battye et al. (2013) power spectra using the cross-correlation estimator and the appropriate F_ℓ for these simulations. Two different noise simulations have been done at two different central frequencies. The reconstructed power spectra generally agree with the input, with higher precision achieved with lower noise levels.

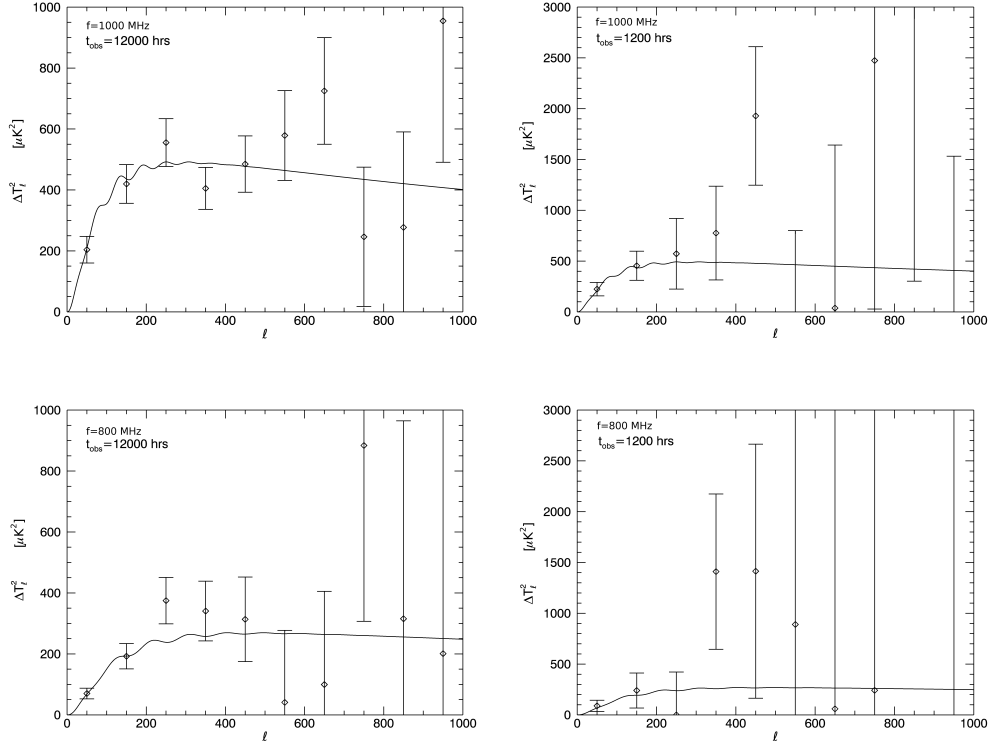


Figure 5.5: Recovered power spectra for a Tianlai-like configuration using Battye *et al.* (2013) power spectrum and cross-correlation estimator, corrected with F_ℓ . The top power spectra are centred on $f = 1000$ MHz while the bottom row are centred on $f = 800$ MHz. The left and right plots show results for $t_{\text{obs}} = 12000$ hrs and 1200 hrs respectively. All power spectra were computed using $\Delta f = 5$ MHz.

Fig. 5.6 confirms that recovered power spectrum agrees with the input, achieving higher precision than before with a longer observation time being used. These results allow us to be confident in the code and method of recovering power spectra.

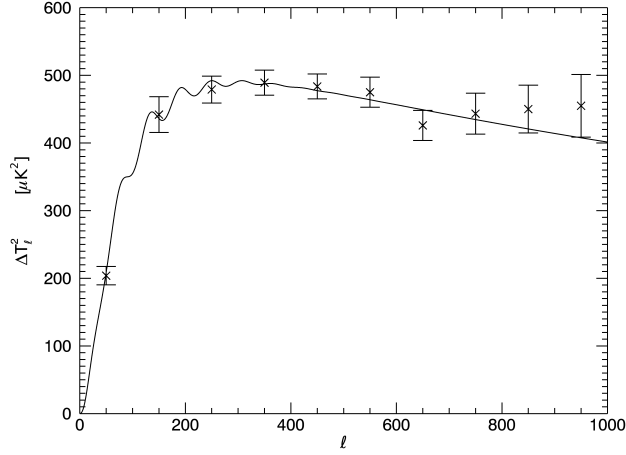


Figure 5.6: *Recovered power spectra for a Tianlai-like configuration using Battye et al. (2013) power spectrum and cross-correlation estimator, corrected with F_ℓ . The power spectrum is centred on $f = 1000$ MHz, showing results for $t_{\text{obs}} = 120000$ hrs using $\Delta f = 5$ MHz.*

5.3.1 Changing Bin Widths

A conclusion of the Battye et al. (2013) paper was that the optimum frequency bandwidth to look at was 50 MHz instead of 4.6875 MHz which was used in the analysis above. It would therefore be interesting to do a similar analysis for a wider frequency bin to see how the results changed.

There are several ways in which a frequency bandwidth of $\Delta f = 50$ MHz can be achieved using the data. The first is to simply change the width of each channel so that one channel is increased from $\Delta f = 5$ MHz to $\Delta f = 50$ MHz. The second involves combining the cross-correlation results of 11 individual channels of width $\Delta f = 5$ MHz. Computationally, the second method would be much quicker. This is because it only requires the cross-correlation of visibilities in $\Delta f = 5$ MHz, rather than cross-correlating all the visibilities in $\Delta f = 50$ MHz. There are fewer visibilities in a smaller channel width and so the cross-correlation step is much quicker in the second method, even though it has to be done for each individual

channel. Both methods, however, should be tested to see what difference they have on the final result, illustrated by Fig. 5.7.

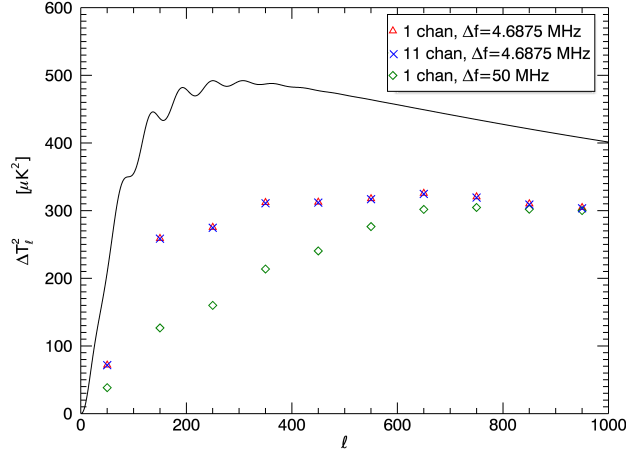


Figure 5.7: Power spectra computed using Battye et al. (2013) power spectrum as input with no noise for different bin widths. Each power spectrum was calculated at $f = 1000$ MHz.

From Fig. 5.7 it is evident that having wider channels results in greater signal loss as ℓ decreases. Combining many smaller channels together produces a result that is similar to the previous single channel case, which was expected. Although the results are different, this can be corrected for with the F_ℓ that is found for each case. It is therefore necessary to test how the two methods compare when trying to recover the power spectrum once noise has been added.

The top two plots in Fig. 5.8 compare two different methods of achieving $\Delta f = 50$ MHz and how well each method recovered the power spectrum. As both cases seem to recover the power spectrum equally well, the method of combining smaller channels and averaging will be used from now on as it is much less time intensive and produces very similar results. The bottom plot of Fig. 5.8 illustrates that as the noise levels are reduced even further, a more precise measurement of the power spectrum is made which agrees well with the input.

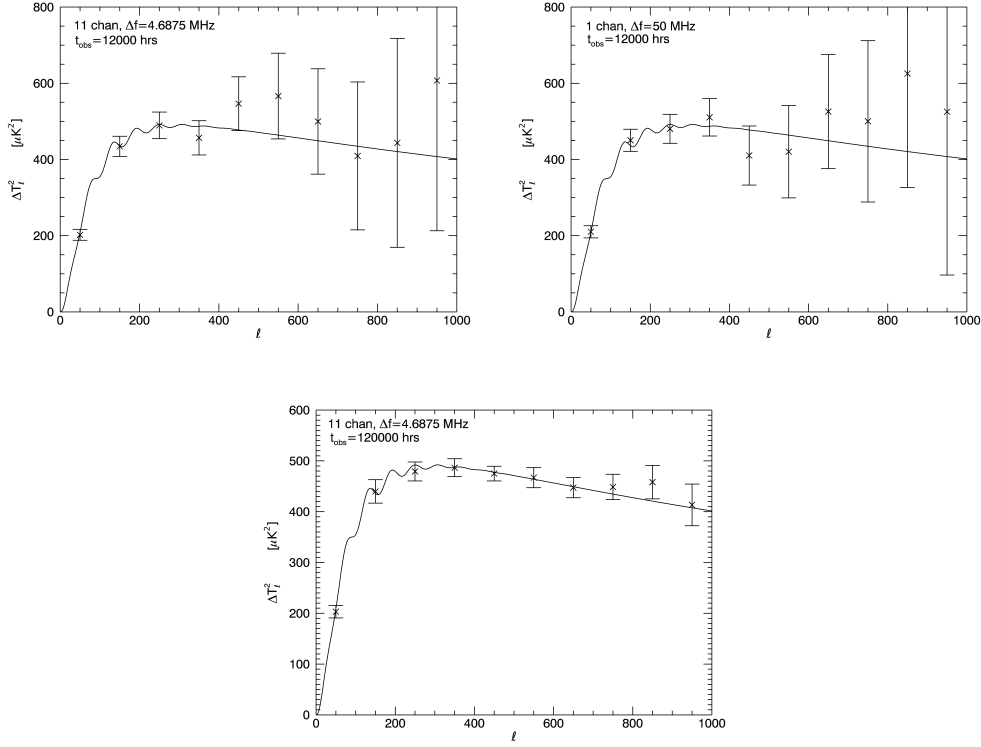


Figure 5.8: Recovered power spectra using Battye et al. (2013) power spectrum with noise and cross correlation estimator, corrected with F_ℓ for $\Delta f = 50$ MHz all centred on $f = 1000$ MHz. Two methods of making $\Delta f = 50$ MHz have been used.

5.3.2 Error Bar Estimation

A final check that the simulations are working correctly is to try and predict the error bars on the simulations using an analytic formula. The uncertainty on each visibility can be found directly from the simulation by fitting a Gaussian to a histogram of visibilities and measuring the width. As only the real parts are being plotted, the width represents $\sigma/\sqrt{2}$ rather than just σ . The uncertainty on the visibilities for ‘Tianlai’ was found to be 9.09×10^{-3} Jy and 2.88×10^{-3} Jy for simulations using $t_{\text{obs}} = 12000$ hrs and $t_{\text{obs}} = 120000$ hrs respectively, and the plots illustrating this are shown in Fig. 5.9.

To be able to fit a formula to the error bars, the error on the visibilities needs

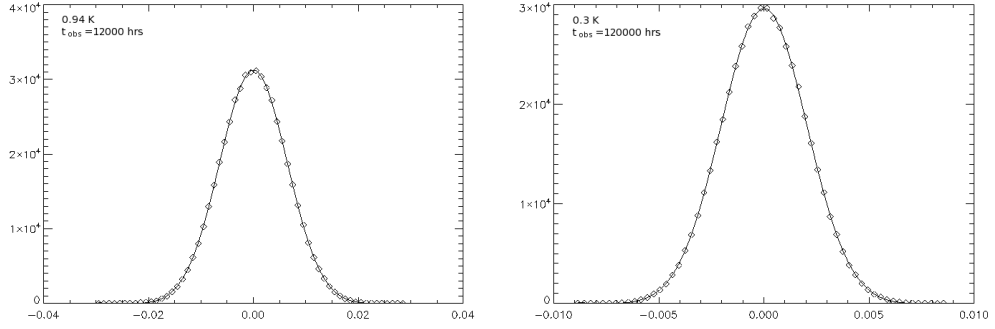


Figure 5.9: Histograms of the real part of the visibilities using the Battye et al. (2013) power spectrum with $t_{\text{obs}} = 12000$ hrs (left plot) and $t_{\text{obs}} = 120000$ hrs (right plot) for Tianlai-like array.

to be predicted accurately rather than obtained from the simulations themselves. Hamilton et al. (2008) state that the error on the power spectrum can be written as

$$\Delta C_\ell = \sqrt{\frac{1}{N_\neq(\ell)} \left(C_\ell + \frac{2\sigma_V^2}{\Omega} \right)}, \quad (5.3.1)$$

where Ω is the solid angle, $N_\neq(\ell)$ is the number of modes in a given ℓ and σ_V is the noise on the visibilities. The first term of equation 5.3.1 is related to the cosmic variance while the second term is linked to the error on the visibilities. Hamilton et al. (2008) define

$$\sigma_V^{HI} = \frac{2\sqrt{2}\text{NET}_{\text{HI}}\Omega}{\sqrt{N_{\text{eq}}}\sqrt{N_t}}, \quad (5.3.2)$$

where NET_{HI} is the noise equivalent temperature, N_{eq} is the number of equivalent baselines and N_t is the number of time samples. This comes from the radiometer equation (see also Section 1.4) and can be used to work out how σ_V^{HI} relates to the width calculated from the histogram of visibilities. It was found that the histogram width and eq. 5.3.2 are related by

$$\sigma = \sqrt{2}\sigma_V^{HI}. \quad (5.3.3)$$

The correct value of σ can be substituted into equation 5.3.1 and the theoretical error bars can be plotted.

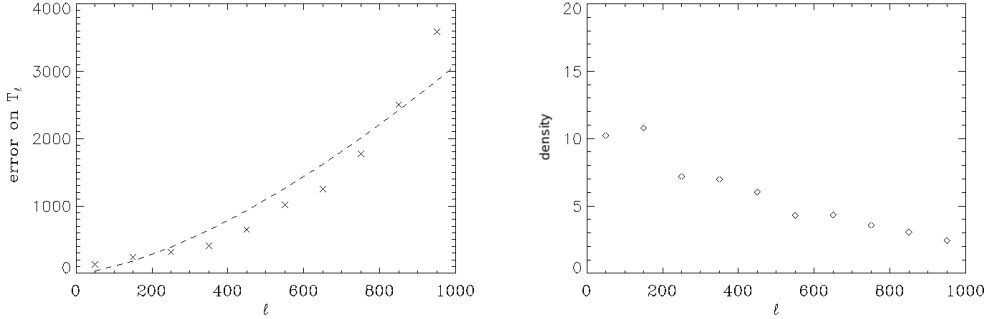


Figure 5.10: *Left: Plot showing theoretical error on power spectrum (dashed line) with the actual values from the simulation (crosses). The power spectrum was computed for $t_{\text{obs}} = 12000$ hrs over 11 channels giving $\Delta f = 50$ MHz, centred on 1000 MHz. Right: Plot showing how the density of visibilities varies over different l -bins. Both plots are for a Tianlai-like configuration.*

Fig. 5.10 shows that the predicted errors on the power spectrum do not agree exactly with the actual errors found from the simulations (left plot). The main cause of this is likely due to the $N_{\neq}(\ell)$ factor in equation 5.3.1. This factor can be thought of as the number of visibilities in a particular ℓ -mode given by (Hamilton et al., 2008)

$$N_{\neq}(\ell) = \ell \Delta \ell f_{\text{sky}}, \quad (5.3.4)$$

where $\Delta \ell$ is the bin width in ℓ and f_{sky} is the fraction of sky looked at. It is clear from the equation that Hamilton et al. (2008) assume a constant density of visibilities in each ℓ -bin. The right hand plot in Fig. 5.10 illustrates how the density of visibilities changes for each ℓ -bin. It is clear that for our simulations the density gradually decreases across the ℓ -bins.

In order to correct this it was first necessary to find out the total number of visibilities in the simulation. It is then possible to work out a density such that the visibilities are spread over the ℓ -bins with density remaining constant. This

constant density can then be compared with the actual density values and a ratio of how much our densities changes compared to a constant value can be found. This ratio can then be used to correct $N_{\neq}(\ell)$ so that it now represents how the density in our simulations changes.

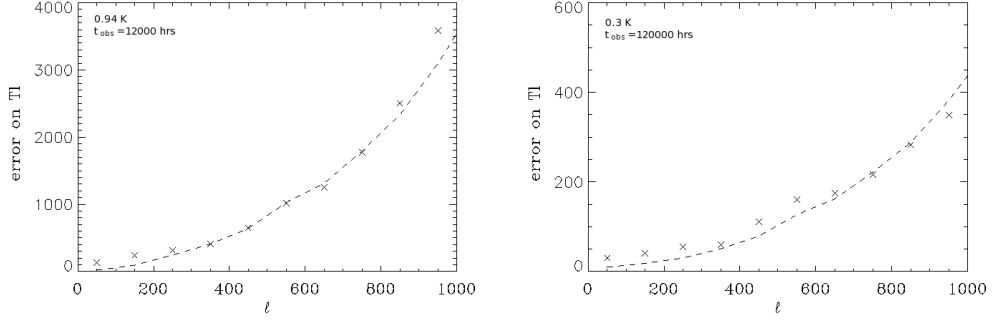


Figure 5.11: *Theoretical errors on the power spectrum (dashed line) corrected using the changing density of visibilities plotted over the values obtained from simulations. The power spectra were computed for $t_{\text{obs}} = 12000$ hrs (left) and $t_{\text{obs}} = 120000$ hrs (right) over 11 channels giving $\Delta f = 50$ MHz, centred on 1000 MHz. Both plots are for a Tianlai-like configuration.*

Fig. 5.11 shows the new theoretical error on the power spectrum plotted over the actual values from the simulations. This was done for two different observation times. From the plot on the left it is clear that the correct $N_{\neq}(\ell)$ has made a difference and the theoretical curve agrees well with the results. The agreement is also good for the other simulation indicating that this formula can be used to predict the error on the power spectrum.

5.4 Results for Tianlai, MeerKAT and ASKAP

Dirty maps of the Battye et al. (2013) power spectrum for each array configuration are shown in Figs. 5.12, 5.13 and 5.14. Each figure contains dirty maps with no noise present, and dirty maps for three different observation times, containing

noise. The different figures are centred on different frequencies so the performance of the interferometers can be compared at different redshifts. At the lowest frequency (Fig. 5.12) the Tianlai-like array is just starting to detect some signal in the maps. After 12000 hours both the Tianlai-like array and ASKAP are detecting some signal. The dirty images for MeerKAT do not indicate much signal is being detected at this redshift ($z \sim 0.8$).

At $z \sim 0.4$ (Fig. 5.13) the maps indicate that both ‘Tianlai’ and ASKAP are able to detect signal after 1200 hrs. The maps suggest that MeerKAT performs the worst of the three interferometers with signal just being detected after 12000 hrs. Again, at $z \sim 0.2$ (Fig. 5.14) the maps show that ‘Tianlai’ performs better than the other two arrays.

The signal-to-noise ratios (SNRs) of each dirty map can be calculated by finding the ratio of the rms signal in the dirty map to the noise. The SNRs should give us an idea of how well each interferometer performs at each frequency and the values can be found in Table 5.1.

	Tianlai			MeerKAT			ASKAP		
	f_1	f_2	f_3	f_1	f_2	f_3	f_1	f_2	f_3
120 hrs	6.4	7.4	7.3	2.3	2.9	3.4	6.2	7.0	6.5
1200 hrs	19.8	21.3	21.6	6.7	9.1	9.7	18.3	20.4	20.8
12000 hrs	63.9	64.6	72.7	22.9	29.9	35.2	54.9	62.3	67.8

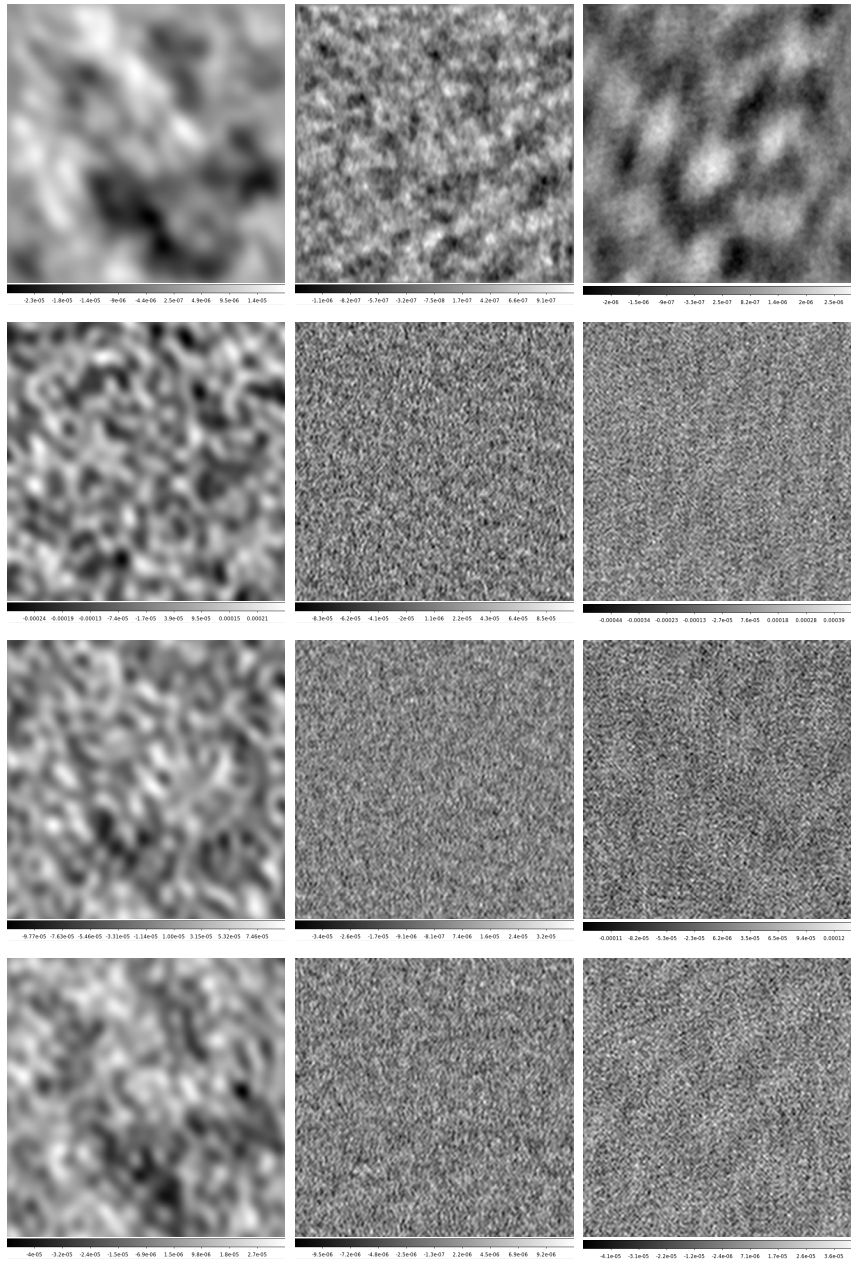
Table 5.1: *SNR values for Battye et al. (2013) dirty maps. $f_1 = 800$ MHz, $f_2 = 1000$ MHz, $f_3 = 1200$ MHz.*

From the SNR values in Table 5.1 and the dirty maps in Figs. 5.12, 5.13 and 5.14 it seems that all three interferometers should be able to detect some HI signal at high frequencies (~ 1200 MHz) in a reasonable amount of time (12000 hrs).

After just 1200 hours, both Tianlai and ASKAP have the potential to detect some integrated HI signal in the maps, especially at high frequencies. To be able to detect signal at the lower frequencies (1000 MHz and 800 MHz) longer observation

times are required but both seem to have the ability to detect signal down to 800 MHz in 12000 hours. MeerKAT seems the least suitable out of the three options, due to few it having few short baselines (see Fig. 3.1) and small field-of-view (FOV). Although ASKAP was designed in a similar way to MeerKAT, it's much larger FOV seems to be advantageous, giving it similar potential to Tianlai, the purposefully designed instrument.

Although the dirty maps give a good general idea of how much signal each interferometer can detect, power spectrum analysis is a cleaner, more powerful method. Since the power spectrum provides us with more information than we can see from the maps we shall concentrate on $f = 800$ MHz and $f = 1000$ MHz, corresponding to $z \sim 0.8$ and $z \sim 0.4$ respectively. This is because the dirty maps at 1200 MHz indicate that all three arrays should be able to detect some sort of signal after 12000 hrs so the power spectrum analysis will be more useful at the lower frequencies where we have less information from the maps.

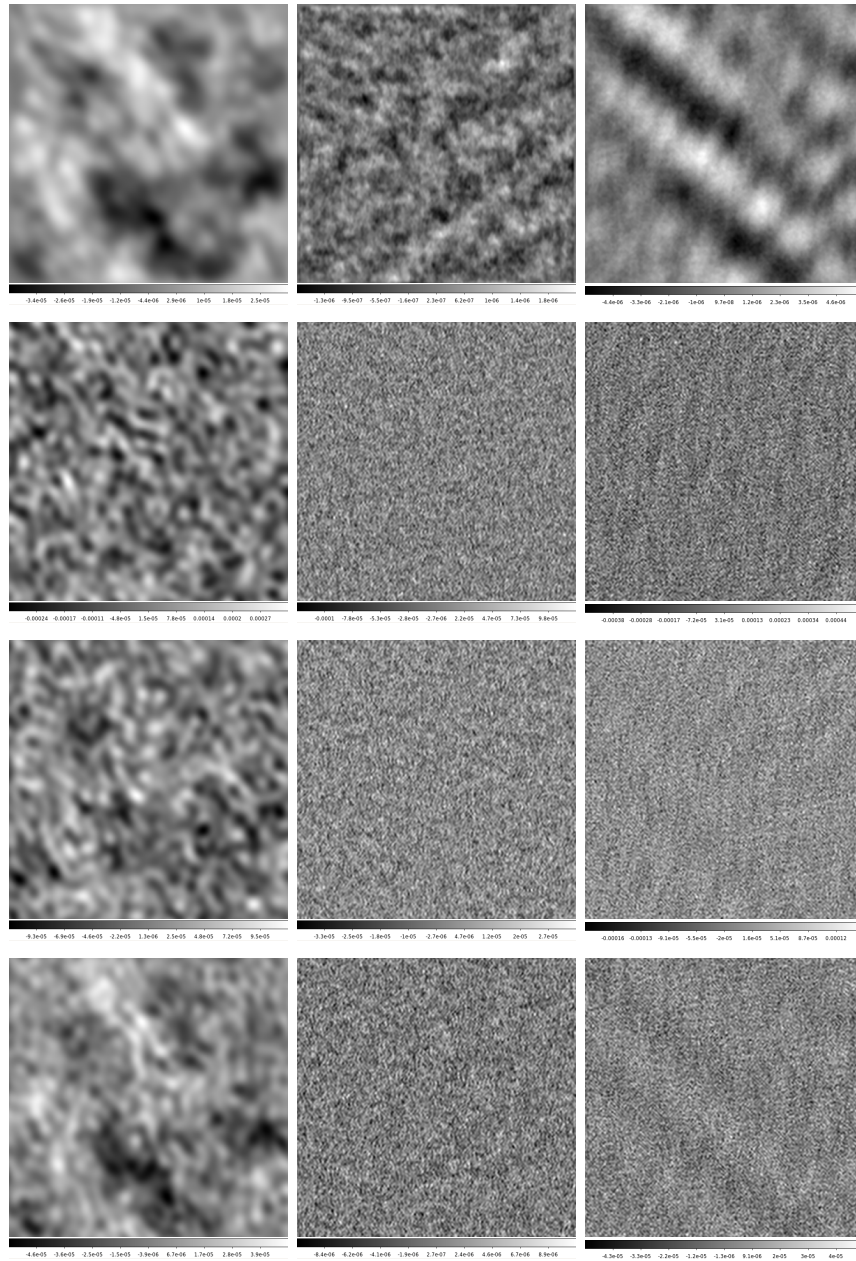


a) Tianlai

b) MeerKAT

c) ASKAP

Figure 5.12: Dirty maps for each array at different observation times. The top row shows dirty maps with no noise while the remaining rows show dirty maps for observation time of 120 hrs, 1200 hrs and 12000 hrs from second to fifth row. All maps are at $f = 800$ MHz ($z \sim 0.8$) using $\Delta f = 5$ MHz, showing an area of 5.5×5.5 deg². The scale is linear, with maximum and minimum values determined by scanning the image, and in units of Jy/pixel.



a) Tianlai

b) MeerKAT

c) ASKAP

Figure 5.13: Dirty maps for each array at different observation times. The top row shows dirty maps with no noise while the remaining rows show dirty maps for observation time of 120 hrs, 1200 hrs and 12000 hrs from second to fifth row. All maps are at $f = 1000$ MHz ($z \sim 0.4$) using $\Delta f = 5$ MHz, showing an area of 5.5×5.5 deg². The scale is linear, with maximum and minimum values determined by scanning the image, and in units of Jy/pixel.

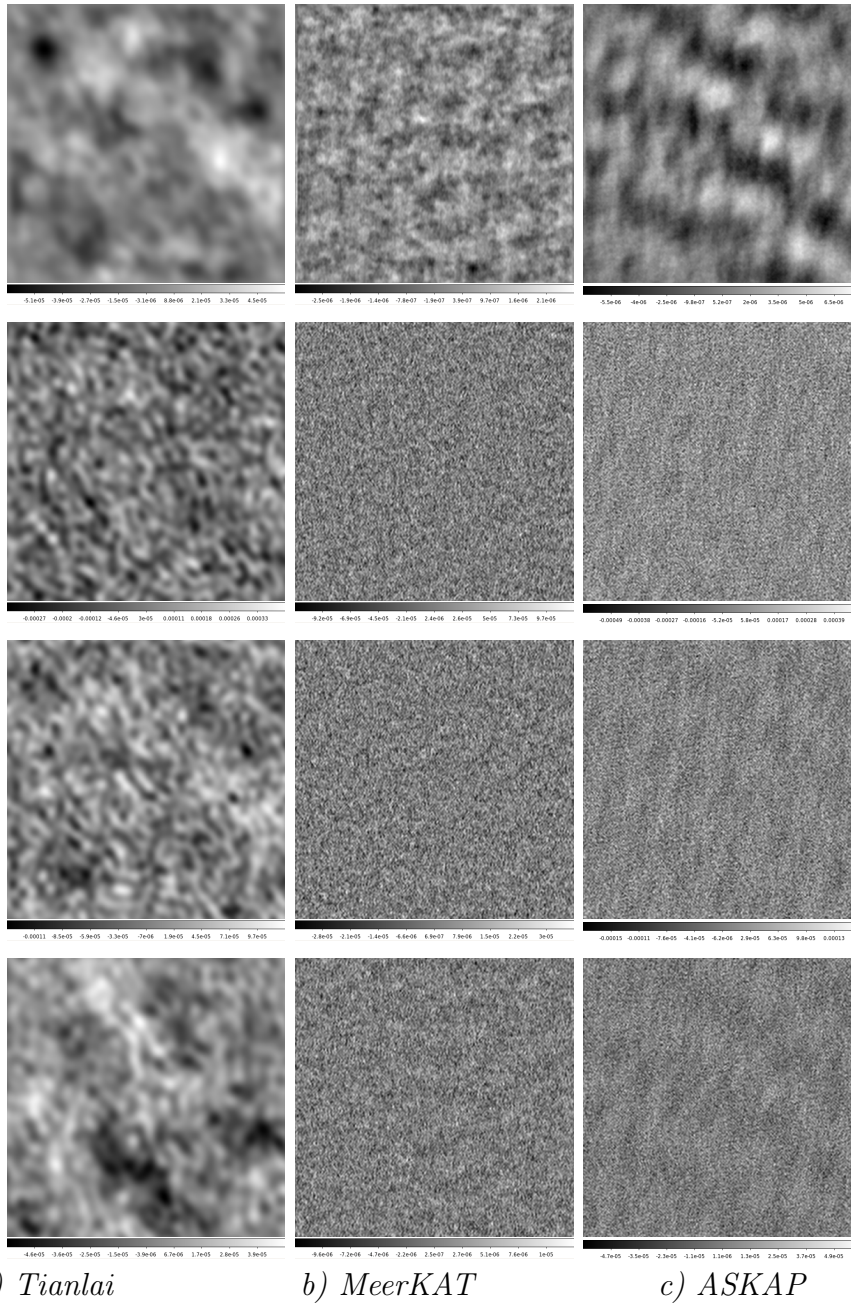


Figure 5.14: *Dirty maps for each array at different observation times. The top row shows dirty maps with no noise while the remaining rows show dirty maps for observation time of 120 hrs, 1200 hrs and 12000 hrs from second to fifth row. All maps are at $f = 1200$ MHz ($z \sim 0.2$) using $\Delta f = 5$ MHz, showing an area of 5.5×5.5 deg². The scale is linear, with maximum and minimum values determined by scanning the image, and in units of Jy/pixel.*

5.4.1 Recovered HI Angular Power Spectrum

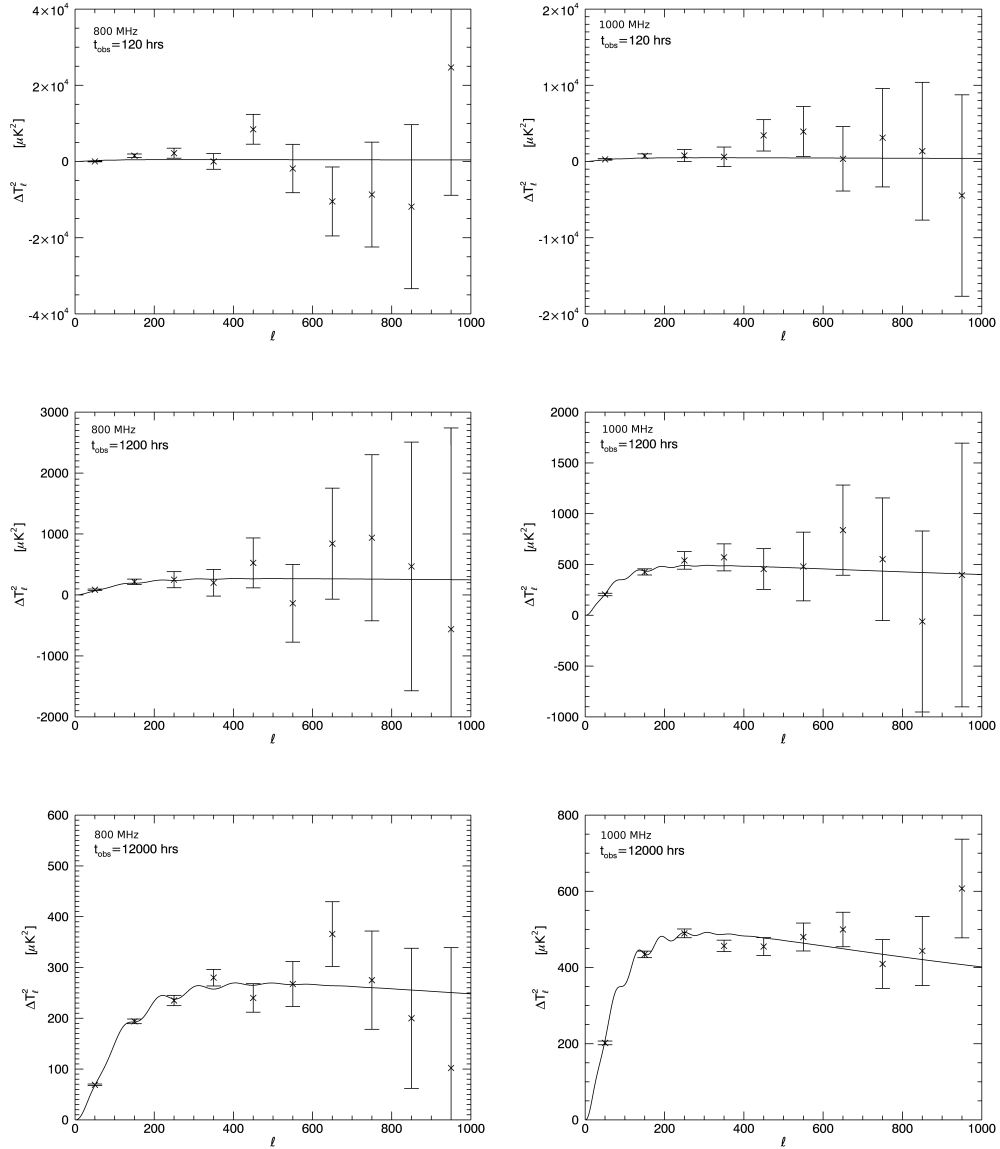


Figure 5.15: Recovered HI angular power spectra using Tianlai for several different observation times: 120 hrs, 1200 hrs and 12000 hrs. The left plots are centred on $f = 800$ MHz and the right plots are centred on $f = 1000$ MHz, all with $\Delta f = 50$ MHz. Error bars represent instrumental noise only (no sample variance). Note the varying vertical axis scale in the plots.

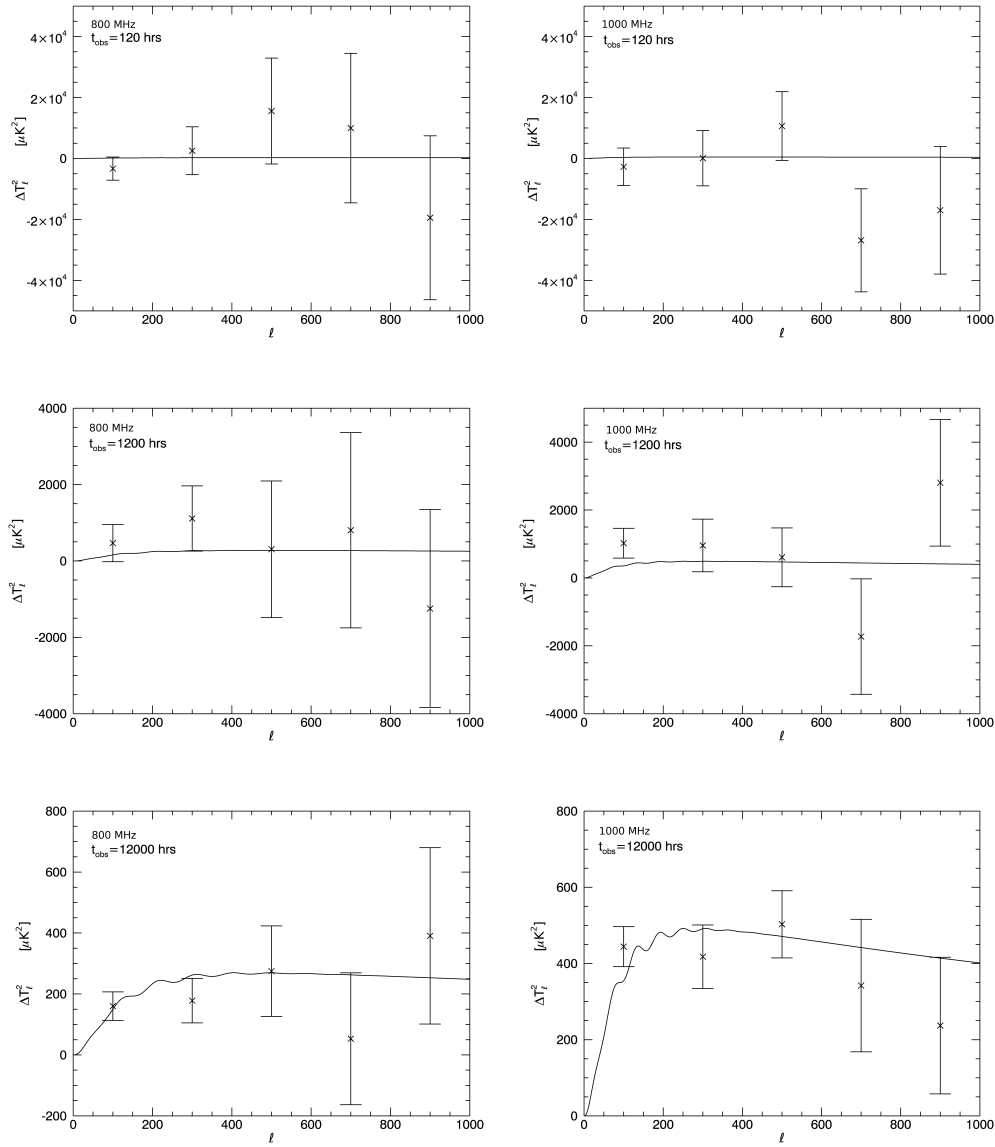


Figure 5.16: Recovered HI angular power spectra using MeerKAT for several different observation times: 120 hrs, 1200 hrs and 12000 hrs. The left plots are centred on $f = 800$ MHz and the right plots are centred on $f = 1000$ MHz, all with $\Delta f = 50$ MHz. Error bars represent instrumental noise only (no sample variance). Note the varying vertical axis scale in the plots.

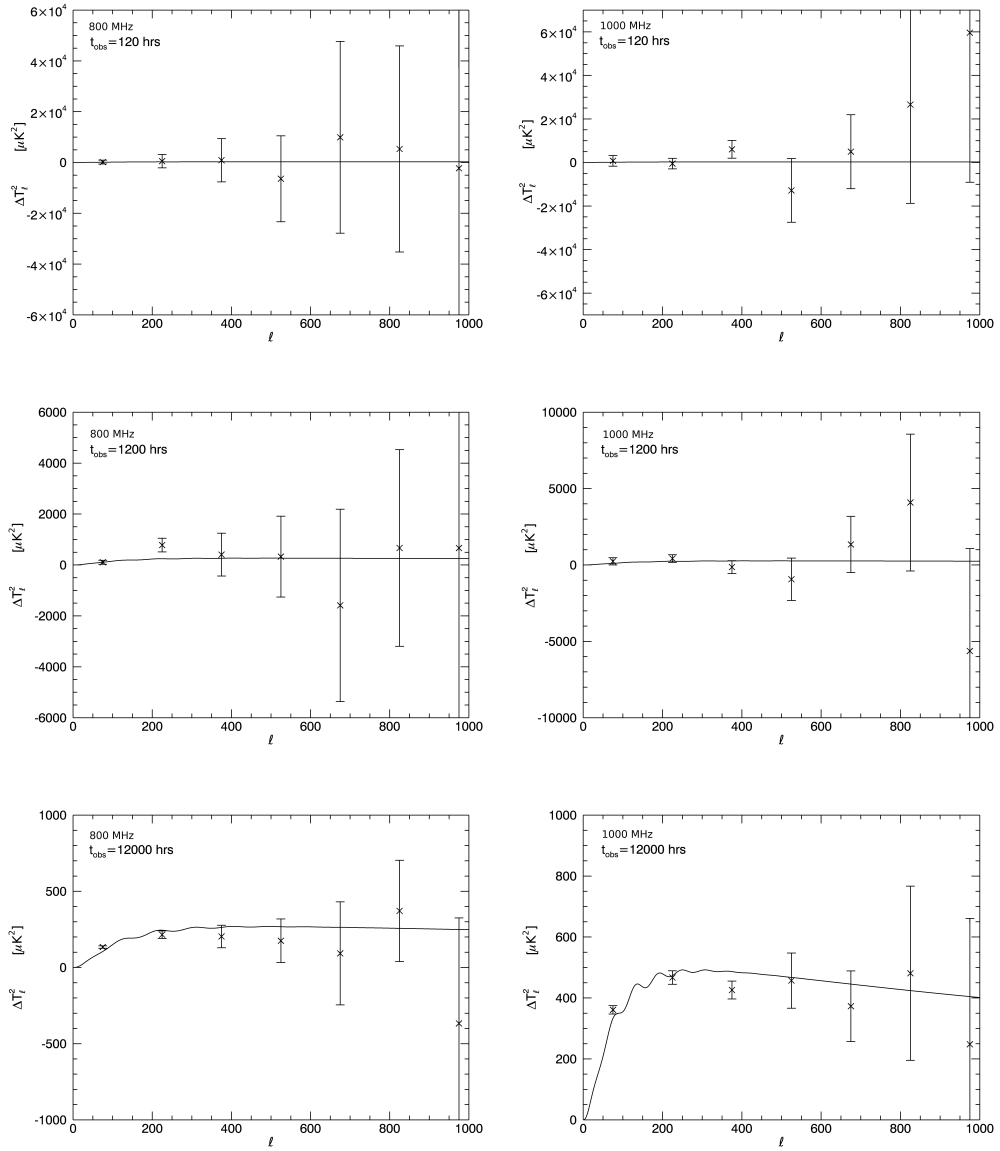


Figure 5.17: Recovered HI angular power spectra using ASKAP for several different observation times: 120 hrs, 1200 hrs and 12000 hrs. The left plots are centred on $f = 800$ MHz and the right plots are centred on $f = 1000$ MHz, all with $\Delta f = 50$ MHz. Error bars represent instrumental noise only (no sample variance). Note the varying vertical axis scale in the plots.

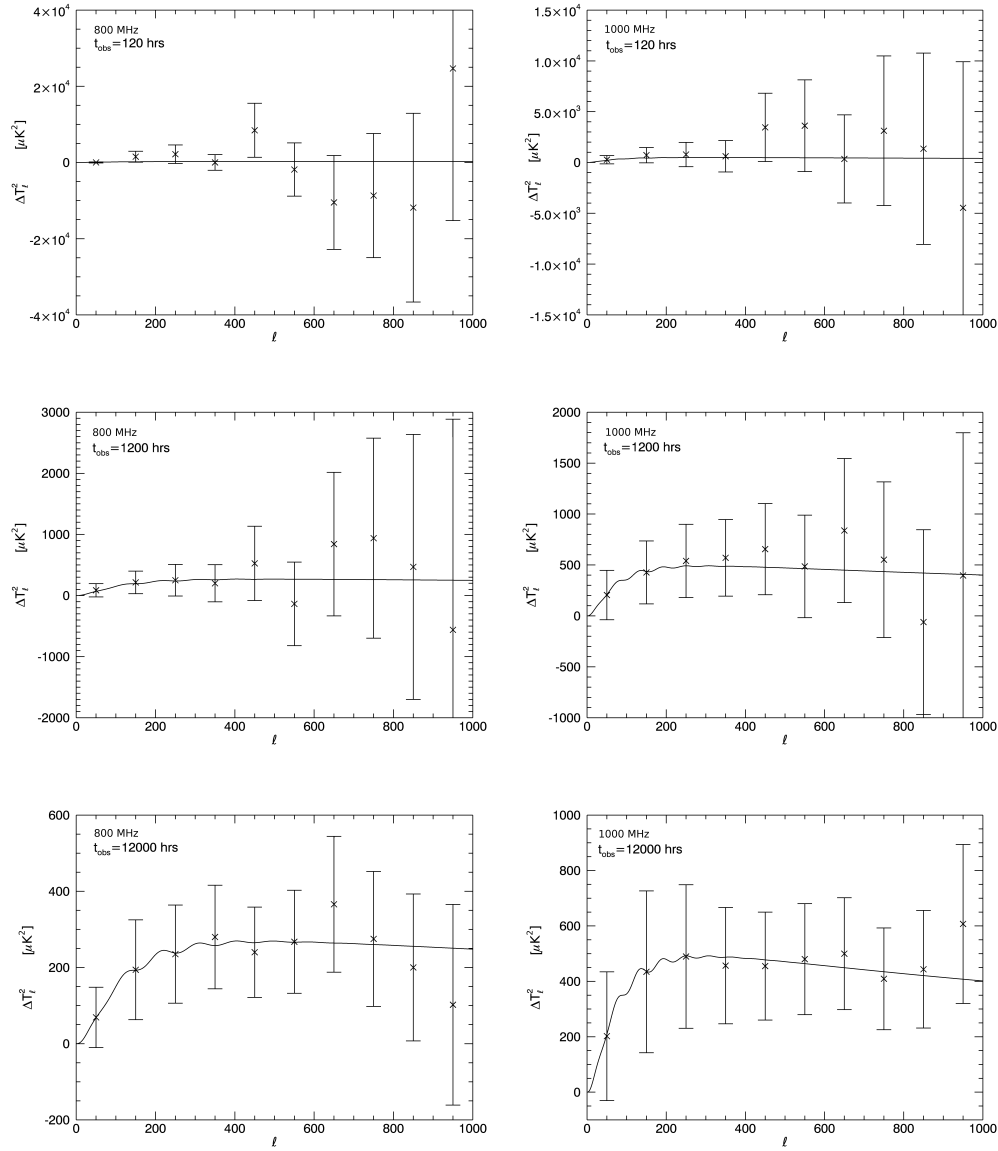


Figure 5.18: Recovered HI angular power spectra using Tianlai for several different observation times: 120 hrs, 1200 hrs and 12000 hrs. The left plots are centred on $f = 800$ MHz and the right plots are centred on $f = 1000$ MHz, all with $\Delta f = 50$ MHz. Error bars represent instrumental noise plus sample variance for one pointing only ($\text{FOV} = 9 \text{ deg}^2$). Note the varying vertical axis scale in the plots.

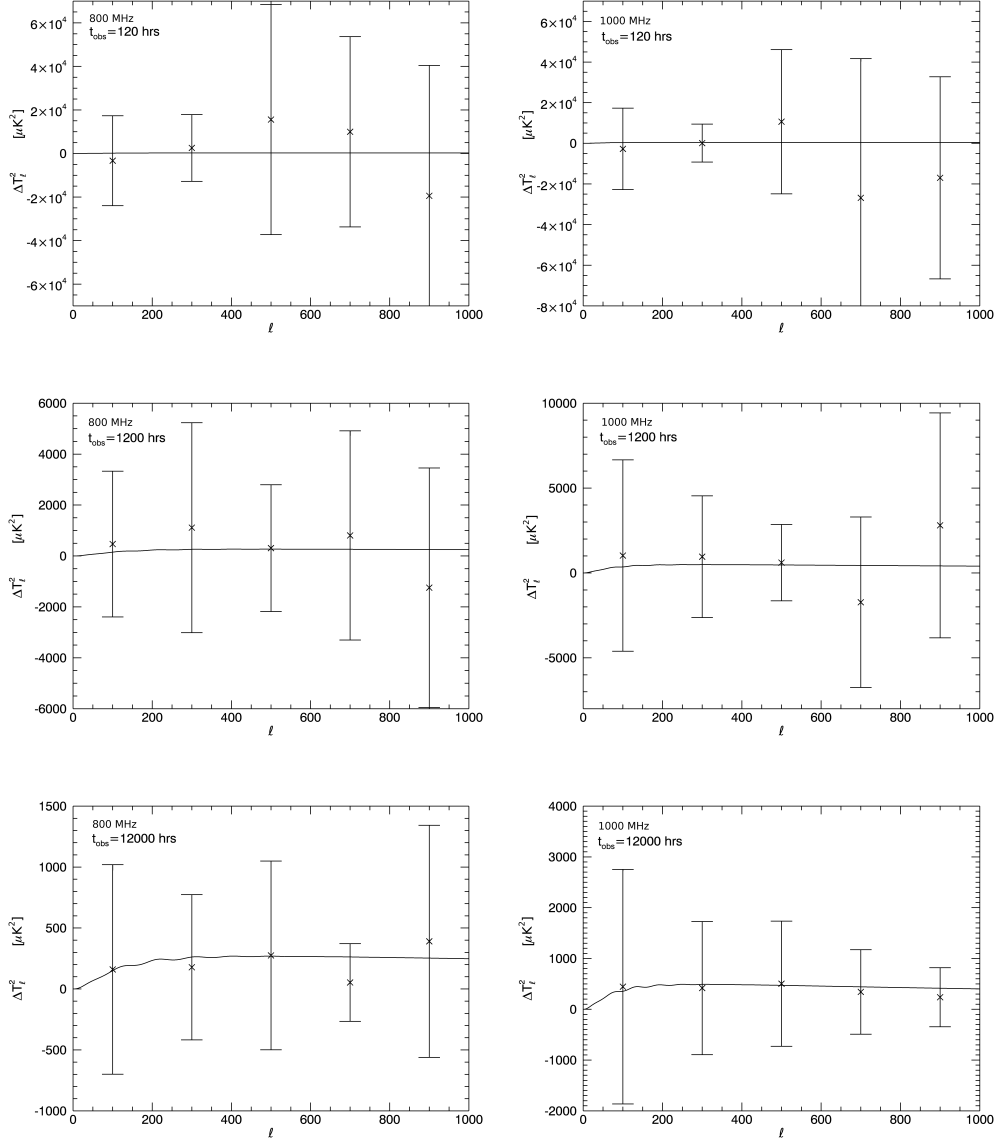


Figure 5.19: Recovered HI angular power spectra using MeerKAT for several different observation times: 120 hrs, 1200 hrs and 12000 hrs. The left plots are centred on $f = 800$ MHz and the right plots are centred on $f = 1000$ MHz, all with $\Delta f = 50$ MHz. Error bars represent instrumental noise plus sample variance for one pointing only ($\text{FOV} = 1 \text{ deg}^2$). Note the varying vertical axis scale in the plots.

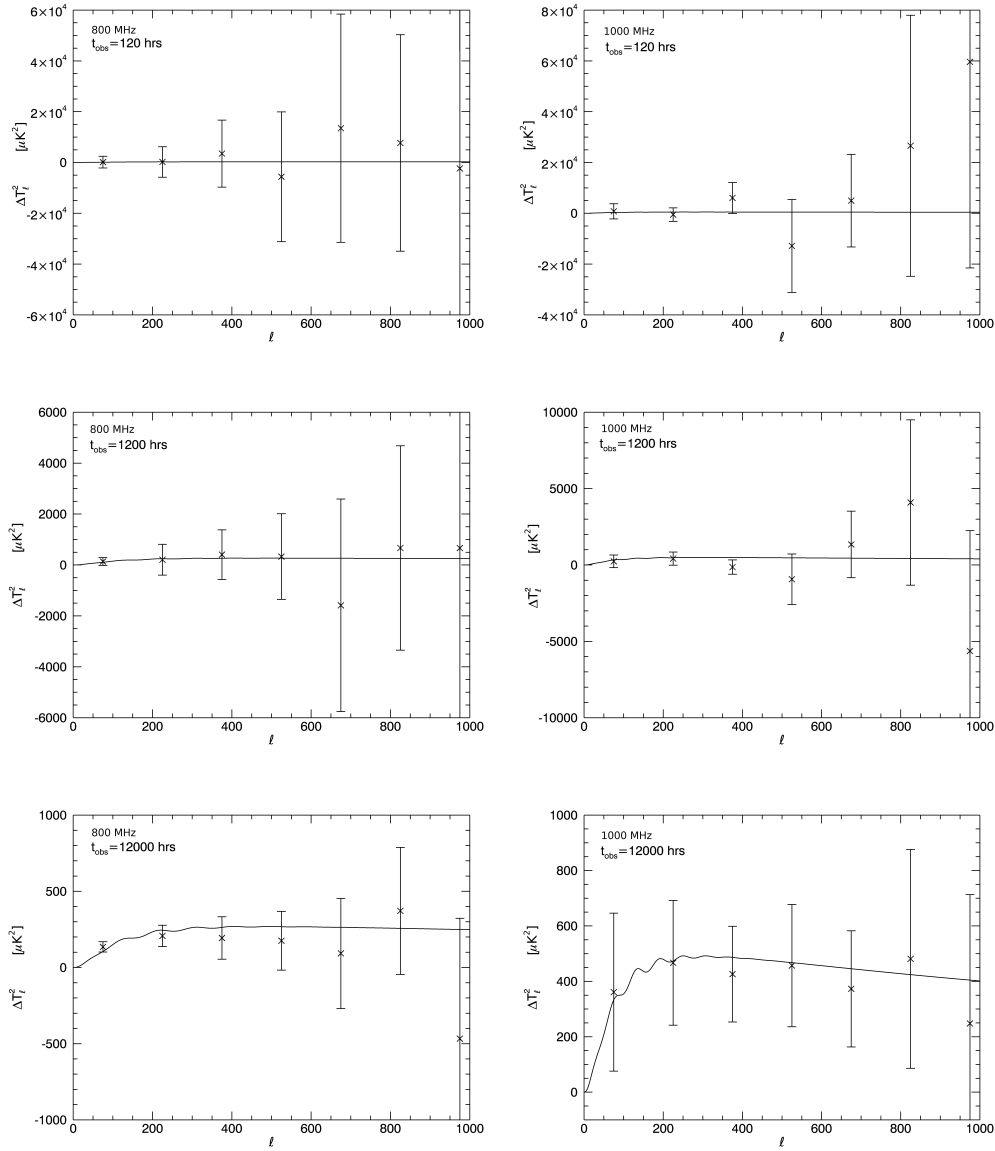


Figure 5.20: Recovered HI angular power spectra using ASKAP for several different observation times: 120 hrs, 1200 hrs and 12000 hrs. The left plots are centred on $f = 800$ MHz and the right plots are centred on $f = 1000$ MHz, all with $\Delta f = 50$ MHz. Error bars represent instrumental noise plus sample variance for one pointing only ($\text{FOV} = 30 \text{ deg}^2$). Note the varying vertical axis scale in the plots.

Figs. 5.15, 5.16 and 5.17 show the results of the power spectrum analysis done on the Battye et al. (2013) input. The analysis was done for each array for several different observation times (120 hours, 1200 hours and 12000 hours, corresponding to 5 days, 50 day and 500 days) and at two different central frequencies (800 MHz and 1000 MHz) but only one pointing. Generally, signal detection in the power spectrum looks better than in the dirty maps as the phase information has been averaged. In these plots only the instrumental noise has been included so they are not a realistic representation of how each interferometer will perform at each frequency.

Figs. 5.18, 5.19 and 5.20 show the recovered HI angular power spectrum with sample variance included. As the simulations were only done for one pointing the sample variance is large making it difficult to make an accurate measurement of the power spectrum. MeerKAT suffers most as it has the smallest field-of-view of the three arrays. ASKAP has the largest field-of-view so it will be least affected by sample variance, which is illustrated in the plots. The dominating sample variance will also mean that, in practice, the signal-to-noise ratios are small. This leads to the question of how many pointings are needed to get a good detection.

A quick method to optimise the survey strategy is to find how many pointings would be needed so that the instrumental noise and sample variance are of a similar size. We saw in Section 5.3.2 that it was possible to fit the instrumental noise successfully with a theoretical formula which depended on quantities that are variables in our simulation. We can therefore modify this error for many pointings to find the optimum number.

As the number of pointings increases the sample variance decreases as a larger portion of the sky is being surveyed. The instrumental noise, however, increases with the number of pointings. This is because in order to keep the total observation time constant (for a fair comparison of results), the time spent on each individual

pointing will be less.

The signal-to-noise ratio (SNR) for the power spectrum is calculated by first calculating the SNR values of each ℓ -bin (which is just the signal over the error bar) and then adding them in quadrature. As the sample variance and instrumental noise change with the number of pointings, the SNR value will change too. It is therefore possible to find the number of pointings which corresponds to the highest SNR.

Fig. 5.21 shows how the signal-to-noise ratio (SNR) changes with the number of pointings for the three arrays at different frequencies. It can be seen from the plots that generally as the observation time increases, the SNR is higher for a certain number of pointings, with the optimal SNR occurring at a slightly higher number of pointings as the observation time is increased. As the number of pointings is initially increased there is a peak in the SNR where the instrumental noise and sample variance are of comparable sizes. Beyond this peak the instrumental noise becomes the dominating error and the SNR decreases.

The top plots in Fig. 5.21 show the optimal number of pointings for ‘Tianlai’ at two frequencies. For observation times of 120 hours, the optimal number of pointings is around 15 for both frequencies, corresponding to a sky survey area of 135 deg^2 . Since this number of pointings also gives good SNR at the longer observation times this would be the best choice as beyond 15 pointings the SNR value drops sharply for 120 hours.

MeerKAT has slightly broader peaks in the SNR compared to ‘Tianlai’ so the optimum number of pointings is less well defined. For 800 MHz and 1000 MHz the optimal number of pointings is around 125 and 140, respectively, which gives a total sky survey area of about 130 deg^2 . This is approximately where the peak SNR lies for 120 hrs observation time and, again, gives good SNR for longer observations.

The lower plots in Fig. 5.21 show that ASKAP follows a similar trend to

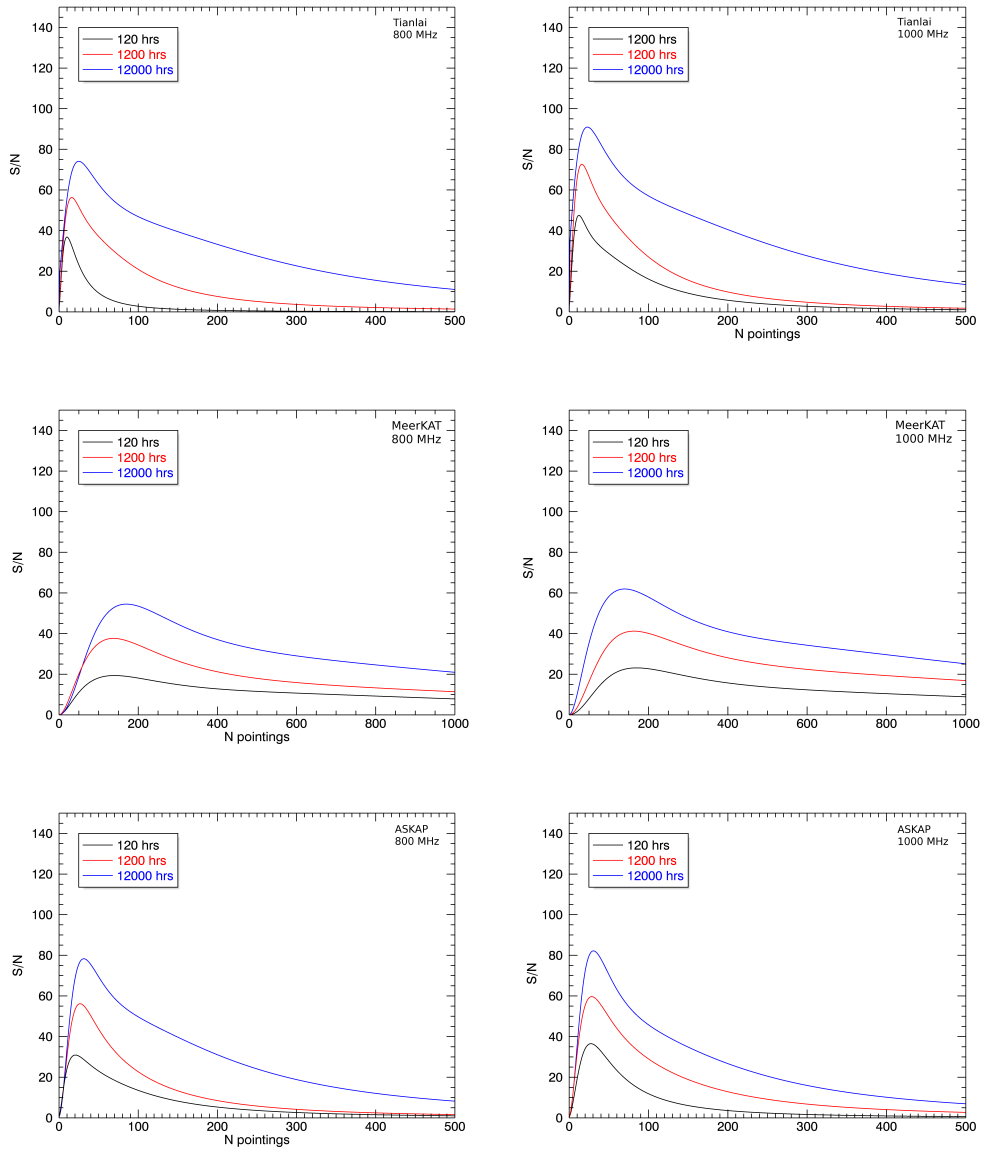


Figure 5.21: Plots illustrating how the SNR changes with number of pointings for ‘Tianlai’ (top plots), MeerKAT (middle plots) and ASKAP (bottom plots) for two frequencies; 800 MHz on the left and 1000 MHz on the right.

‘Tianlai’ and has fairly well defined peaks. The peaks lie fairly close together so we can take the optimum to be where the 120 hours peak lies, which corresponds to 20 and 25 pointings for 800 MHz and 1000 MHz respectively. This would be

the equivalent of a total of around 650 deg².

Table 5.2 summarises the optimal number of pointings for each array at the two different frequencies. We can see that a Tianlai-like configuration requires the fewest number of pointings and MeerKAT the most. It was shown in Chapter 3 that ASKAP had the largest field-of-view (FOV) as a result of the PAFs and MeerKAT had the smallest (see Table 3.1). Although MeerKAT and ASKAP were both designed in a similar way, the larger FOV means fewer pointings are required for a good detection of integrated HI signal, making ASKAP comparable with the bespoke instrument.

	Tianlai	MeerKAT	ASKAP
800 MHz	15	125	20
1000 MHz	15	140	25

Table 5.2: *Approximate optimal number of pointings for Tianlai, MeerKAT and ASKAP.*

	Tianlai		MeerKAT		ASKAP	
	800 MHz	1000 MHz	800 MHz	1000 MHz	800 MHz	1000 MHz
120 hours	36	47	20	23	30	36
1200 hours	55	72	37	40	46	60
12000 hours	75	92	55	62	78	82

Table 5.3: *Approximate peak SNR achievable after optimal number of pointings for Tianlai, MeerKAT and ASKAP.*

Table 5.3 summarises the peak SNR achievable for each array’s optimal number of pointings. It can be seen that as the observation times increases the peak SNR value increases, as expected. ‘Tianlai’ had the highest SNR values out of the three arrays while MeerKAT had the lowest. ASKAP has peak SNR values similar to ‘Tianlai’. The reason for these results is that a Tianlai-like configuration has more short baselines giving it better sensitivity to the scales that are of interest to us. MeerKAT and ASKAP both have lots of long baselines but ASKAP has a large

field-of-view, giving it improved sensitivity over MeerKAT.

Although an instrument specifically designed to detect the HI signal seems to perform best, it would be possible to do an HI intensity mapping experiment with all three interferometers and detect signal in a reasonable amount of time.

Chapter 6

Conclusions and Future Work

This thesis studied the effectiveness of using intensity mapping to measure the HI signal with upcoming interferometer arrays. HI intensity mapping is relatively new, fast method used to detect baryonic acoustic oscillations (BAOs). It uses the idea of detecting the HI signal from the combined emission of galaxies rather than detecting individual galaxies, getting rid of the need for high resolution surveys. Although several HI intensity mapping experiments are already being planned, this thesis focused on comparing a bespoke BAO intensity mapping interferometer ‘Tianlai’, with two interferometers under construction that have not been specifically designed for this purpose, namely MeerKAT and ASKAP.

The HI signal was extracted from the Millennium simulation and then the main task of finding a suitable power spectrum estimator was undertaken. This estimator as then used to recover the HI angular power spectrum with the three interferometers of interest.

Initially an autocorrelation estimator was used to try and recover the power spectrum. This involved a mix of incoherent and coherent binning of visibilities from which a noise estimate was subtracted. This method had a problem at high ℓ with a large noise bias. This was due to the noise power spectrum being

incorrectly estimated from simulations meaning the subtraction left residual noise behind. An estimator was needed that did not rely on simulations to generate the noise estimate or subtracting off the noise. It was found that the most suitable power spectrum estimator used the cross-correlation of visibilities within uv -cells. This was more successful because the cross-correlation of random noise visibilities averages to zero. Although this estimator required a correction factor F_ℓ , it had the lowest noise bias out of the estimators investigated.

Using this estimator the HI angular power spectrum was recovered using the three interferometers. As the input power spectrum of the Millennium simulation was unknown, it was not possible to find an F_ℓ specific to the input. A theoretical HI angular power spectrum was instead used as the input to the simulations to give an idea of how well each interferometer can potentially perform.

The power spectrum analysis was only done for one pointing meaning the sample variance was very large, especially for MeerKAT as a result of its small field-of-view. This meant that it was not clear from the power spectra which interferometer could detect the HI signal most accurately. To solve this problem, an optimal number of pointings was found for each array to give the best signal-to-noise ratio (SNR) in a reasonable observing time.

It was found that a Tianlai-like array required the fewest number of pointings (15 pointings) in order to detect some signal after 120 hours (~ 5 days), and make a good detection after 1200 hours (~ 50 days). This is a result of the instrument having improved sensitivity to the angular scales of interest due to large numbers of short baselines. ASKAP was also able to make a good detection after 120 hours, requiring roughly 20 pointings. Despite ASKAP not having an ideal dish configuration (many more long baselines and not many short ones), the PAFs give a very large field-of-view resulting in ASKAP performing almost as well as ‘Tianlai’. After 1200 hours, the final SNRs achievable with an optimal observing strategy

and ideal instruments are approximately 60, 40 and 55 for ‘Tianlai’, MeerKAT and ASKAP.

It was found that all three interferometers would be able to make a good detection after 1200 hours so it would be possible to design an HI intensity mapping experiment for all three interferometers.

6.1 Future Work

Although it is possible to detect the HI signal within a reasonable amount of time, it was shown in Section 2.3 that foregrounds were going to be the biggest problem as they mask the signal. The foregrounds are expected to be several orders of magnitude greater than the signal, which is illustrated in Fig. 6.1.

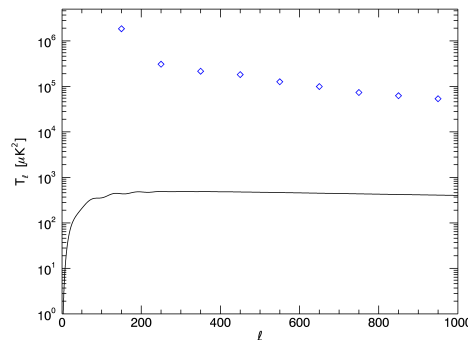


Figure 6.1: *Power spectra for synchrotron emission (diamonds) and HI signal (solid black line), centred on $f=1000$ MHz.*

Suitable foreground removal techniques are needed so that it would then be possible to simulate a more realistic observation. Some initial work was done on synchrotron emission and point sources, so these would be the natural choice of foregrounds to focus on. As the 21 cm signal is uncorrelated in the frequency direction, most foreground removal methods focus on the frequency correlation of foregrounds, exploiting their smooth power spectra. It would be useful to try

a ‘blind’ principle component analysis (PCA) based method on some foreground simulations to show that they can be removed, with signal detected in an ideal case. Once a method has been settled on, more realistic simulations can be done.

Our simulations so far have been for an ideal experiment. In reality there will be systematic errors so this would be another area to investigate. The beam has been modelled as a Gaussian throughout but this is not the case for real experiments. Sidelobes will be present which, if large, can cause interference and unwanted noise. The aim would be to model a more realistic beam shape with the idea of reducing the sidelobes as much as possible. Other beam errors include antenna pointing errors and beam cross polarization. Instrumental errors need to be considered including antenna gain and antenna coupling errors along with calibration errors such as phase and amplitude corrections.

Chapter 3 explained how the ASKAP phased array feeds (PAFs) had been modelled as one large beam, rather than 36 individual beams. We have shown that ASKAP has the potential to be a useful instrument regarding HI intensity mapping so it would be a good idea to make a more accurate simulation using 36 individual beams.

It was concluded in Chapter 5 that a few hundred pointings would be needed to give the best SNR values. It would be interesting to simulate this and see how successful a potential experiment could be at detecting BAOs.

Finally, most of our work was done using a theoretical HI angular power spectrum. Chapter 2 explained how the Millennium simulation was used to create a model of the sky but this was not used for the power spectrum analysis. With suitable corrections applied, doing the power spectrum analysis using the Millennium simulation should give a more realistic simulation than that obtained using a theoretical sky input model.

The overall idea is to come up with a complete end-to-end simulation that

accurately models the complete sky, successfully removes foregrounds and reduces systematics. This thesis has focused on modelling the sky but more work needs to be done regarding foreground removal and systematics.

Appendix A

AIPS Tcl Script

This section contains an example of the Tcl script that was written to simulate interferometric observations. The first part of the script sets the parameters needed for the main body of the script and sets the input/output file names. The sky model and array configuration file are specified in this part. The main body of the code consists of seven main sections which read in the sky model, simulate the visibilities and write out the data as a file and an image.

```
#!/usr/local/bin/tclsh
# Script to run UVCON for HI
# set the output filename
set fileid(OUTPUT) [open OBS.7MC w]

# Set parameters
# Which steps to run (1 = yes, 0 = no)
set do_fitld 1
set do_subim 1
set do_uvcon 1
set do_uvglu 1
set do_imagr 1
set do_clean 0
set do_output_uv 1
set do_output_im 1

# Filenames and in/out names
set infile_cube battyecube-40.fits
set infile_array TIANLAI.UVCON
set outfile_antloc ANTLOC.TXT
set infile_image MODEL
set uv_outname UVDATA
set temp_uv_name TEMPUV
set final_uv_outname FINALUV
set cube_outname CUBE

# Aparam for UVCON
set freqch1 0.3      ;# start freq in GHz
set freqch2 1.5      ;# end freq in GHz
set declination 30.
set min_ha -6.        ;#min hour angle
set max_ha 6.         ;#max hour angle
set min_el 20.
```

```

set int_time 300      ;#integration time per visibility point, sec
set nchan 256        ;#no of freq channels. need to be a value 2**n
set chanwidth [expr (($freqch2 - $freqch1)*1000./$nchan)]

# Primary beam for UVCON
set constant_pbeam 0  ;# 1=yes, 0=no
set pb_ref_freq 1.42
set bmaj 3.0          ;# major axis of beam
set bmin 3.0

# IMAGR parameters
set im_outname "IMAGE"
set cellsize 8        ;# pixel separation in arcsec
set imsize 2048       ;# minimum desired size of the fields
set robust 5          ;# 5=natural weighting
set uvtaper1 0
set uvtaper2 0
set dotv -1
set niter 1000

# Output filenames
set uv_outfile finaluv.fits
set im_outfile finalcube.fits

# #####
#-----MAIN CODE -----

puts $fileid(OUTPUT) "$ This is an AIPS runfile to do spectral line simulations with UVCON"

if {$do_fitld == 1} {
# 1. LOAD IN FULL CUBE TO BEGIN WITH
puts $fileid(OUTPUT) "$ Step 1: Load in FITS cube of the signal (FITLD)..."
puts $fileid(OUTPUT) "restore 0"

```

```

puts $fileid(OUTPUT) "task 'fitld'"
    puts $fileid(OUTPUT) "datain '$infile_cube "
    puts $fileid(OUTPUT) "outna 'INCUBE'"
    puts $fileid(OUTPUT) "go ; wait ; end"
    puts $fileid(OUTPUT) " "
}

# 2. SEPARATE EACH FREQUENCY CHANNEL INTO SEPARATE CHANNEL MAPS
if {$do_subim == 1} {
puts $fileid(OUTPUT) "$ Step 2: Separating cube into channel maps (SUBIM)..."
for {set i 1} {$i <= $nchan} {incr i} {
puts $fileid(OUTPUT) "restore 0"
puts $fileid(OUTPUT) "task 'subim'"
    puts $fileid(OUTPUT) "inna 'INCUBE' "
    puts $fileid(OUTPUT) "outna '$infile_image'"
    puts $fileid(OUTPUT) "blc(3)= $i"    ; # bottom left corner third dim
    puts $fileid(OUTPUT) "trc(3)= $i"    ; # top right corner third dim
    puts $fileid(OUTPUT) "outseq $i"
    puts $fileid(OUTPUT) "go ; wait ; end"
    puts $fileid(OUTPUT) " "
}
}

# 3. DO THE SIMULATION FOR EACH CHANNEL
# Loop over each channel and generate uv data from an array geometry given by INFILE
if {$do_uvcon == 1} {
puts $fileid(OUTPUT) "$ Step 3: Running UVCON for each channel..."
for {set i 1} {$i <= $nchan} {incr i} {
# Set frequency and primary beam
    set freqch [ expr {$freqch1 + (($chanwidth*($i-1.))/1000.)} ] ; #/1000 to get in Mhz
    if {$constant_pbeam == 1} {
set thisbmaj $bmaj
set thisbmin $bmin } else {

```

```

    set thisbmaj [ expr {$bmaj * $pb_ref_freq/$freqch} ]
    set thisbmin [ expr {$bmin * $pb_ref_freq/$freqch} ]
}
puts $fileid(OUTPUT) "restore 0"
puts $fileid(OUTPUT) "task 'uvcon'"
    puts $fileid(OUTPUT) "infi '$infile_array "
    puts $fileid(OUTPUT) "outfi ' ' "
    puts $fileid(OUTPUT) "in2seq $i "
    puts $fileid(OUTPUT) "in2na '$infile_image'"
    puts $fileid(OUTPUT) "outna '$uv_outname'"
puts $fileid(OUTPUT) "outseq $i"
puts $fileid(OUTPUT) "nmaps 0"
    puts $fileid(OUTPUT) "cmodel 'IMAG'"
    puts $fileid(OUTPUT) "cmethod 'DFT'"
    puts $fileid(OUTPUT) "aparm $freqch, 0, $declination, $min_ha, $max_ha, $min_el, $int.
    puts $fileid(OUTPUT) "bparm(6) 4"
    puts $fileid(OUTPUT) "bmaj $thisbmaj"
    puts $fileid(OUTPUT) "bmin $thisbmin"
    puts $fileid(OUTPUT) "go ; wait; end "
puts $fileid(OUTPUT) " "
}
}

# 4. COMBINE UV DATA FOR EACH CHANNEL INTO ONE FILE
if {$do_uvglu == 1} {
puts $fileid(OUTPUT) "$ Step 4: Combining uv data channels into one big uv dataset..."
# Pairs no 1
set outseq 1;
for {set i 1} {$i <= $nchan} {incr i 2} {
    puts $fileid(OUTPUT) "restore 0"
    puts $fileid(OUTPUT) "task 'uvglu'"
        puts $fileid(OUTPUT) "inseq $i "
        puts $fileid(OUTPUT) "inna '$uv_outname'"
}
}

```

```

    puts $fileid(OUTPUT) "in2seq [expr $i+1] "
    puts $fileid(OUTPUT) "in2na '$uv_outname'"
    puts $fileid(OUTPUT) "outna '$temp_uv_name'"
puts $fileid(OUTPUT) "outseq $outseq"
    puts $fileid(OUTPUT) "go ; wait; end "
puts $fileid(OUTPUT) " "
if {$i < [ expr {$nchan -1} ]} { set outseq [incr outseq] }
}
set outseq [incr outseq]
# Additional pairs
set npairs [ expr $nchan/2 -1 ] ;#no pairs left to make after initial pairing
set inseq 1
set thispair 1
set nthispair [expr $nchan/4] ;#number of pairs to make after second pairing
set outseq [ expr $nchan/2 + 1 ] ;#output after pairing the first 2 of the second line
set j $nthispair/2 ;#no pairs should end up with after pairing level together
for {set i 1} {$i <=$npairs} {incr i} {
    puts $fileid(OUTPUT) "restore 0"
    puts $fileid(OUTPUT) "task 'uvglu'"
        puts $fileid(OUTPUT) "inseq $inseq "
        puts $fileid(OUTPUT) "inna '$temp_uv_name'"
        puts $fileid(OUTPUT) "in2seq [expr $inseq+1] "
        puts $fileid(OUTPUT) "in2na '$temp_uv_name'"
    if {$i == $npairs} {puts $fileid(OUTPUT) "outna '$final_uv_outname'"} else {puts $fileid(OUTPUT)
    if {$i == $npairs} {puts $fileid(OUTPUT) "outseq 0"} else {puts $fileid(OUTPUT) "outseq $outseq"}
        puts $fileid(OUTPUT) "go ; wait; end "
puts $fileid(OUTPUT) " "
    set inseq [incr inseq 2]
    set outseq [incr outseq]
    set thispair [incr thispair]
    if {$thispair == $nthispair} {
set j [ expr $j/2]
set thispair 0

```

```

set nthispair [ expr {$nthispair/2} ]
    }
}
}

# 5. Make maps (not CLEANed)
if {$do_imagr == 1} {
puts $fileid(OUTPUT) "$ Step 5: Make maps from the uv dataset (IMAGR)..."
    puts $fileid(OUTPUT) "restore 0"
    puts $fileid(OUTPUT) "task 'imagr'"
        puts $fileid(OUTPUT) "inna '$final_uv_outname'"
        puts $fileid(OUTPUT) "outna '$im_outname'"
        puts $fileid(OUTPUT) "cellsize $cellsize $cellsize"
        puts $fileid(OUTPUT) "imsize $imsize $imsize"
        puts $fileid(OUTPUT) "robust $robust"
        puts $fileid(OUTPUT) "uvtaper $uvtaper1 $uvtaper2"
        puts $fileid(OUTPUT) "imsize $imsize $imsize"
        puts $fileid(OUTPUT) "dotv $dotv"
        if {$do_clean == 1} {           puts $fileid(OUTPUT) "niter $niter" } else {           puts $fi
    puts $fileid(OUTPUT) "go ; wait; end "
    puts $fileid(OUTPUT) " "
}

# 6. Output UV dataset
if {$do_output_uv == 1} {
puts $fileid(OUTPUT) "$ Step 6: Output UV dataset (FITP)...."
    puts $fileid(OUTPUT) "restore 0"
    puts $fileid(OUTPUT) "task 'fittp'"
        puts $fileid(OUTPUT) "inna '$final_uv_outname'"
        puts $fileid(OUTPUT) "incl 'UVGLU'"
        puts $fileid(OUTPUT) "dataout '$uv_outfile"
    puts $fileid(OUTPUT) "go ; wait; end "
    puts $fileid(OUTPUT) " "
}

```

```
}

# 7. Output image cube dataset
if {$do_output_im == 1} {
puts $fileid(OUTPUT) "$ Step 6: Output Image cube dataset (FITTP)..."
  puts $fileid(OUTPUT) "restore 0"
  puts $fileid(OUTPUT) "task 'fittp'"
    puts $fileid(OUTPUT) "inna '$im_outname'"
    if {$do_clean == 1} {      puts $fileid(OUTPUT) "incl 'ICL001'" } else {      puts $fileid(OU
      puts $fileid(OUTPUT) "dataout '$im_outfile"
puts $fileid(OUTPUT) "go ; wait; end "
puts $fileid(OUTPUT) " "
}
```

Appendix B

21 cm Angular Power Spectrum

This section defines the growth function, $D(z)$, and cold dark matter power spectrum, P_{cdm} , used to calculate the 21 cm angular power spectrum from Battye et al. (2013).

The growth function $D(z)$ is given by (see Carroll and Press (1992), Eisenstein and Hu (1988))

$$D(z) = \frac{1}{1+z} \left(\frac{5}{2} \Omega(z) \right) \left(\Omega(z)^{4/7} - \Omega_\Lambda(z) + \left(1 + \frac{\Omega(z)}{2} \right) \left(1 + \frac{\Omega_\Lambda(z)}{70} \right) \right)^{-1}, \quad (\text{B.0.1})$$

where

$$\begin{aligned} \Omega(z) &= \frac{\Omega_0(1+z)^3}{\Omega_\Lambda + \Omega_k(1+z)^2 + \Omega_0(1+z)^3} \\ \Omega_\Lambda(z) &= \frac{\Omega_\Lambda}{\Omega_\Lambda + \Omega_k(1+z)^2 + \Omega_0(1+z)^3}. \end{aligned} \quad (\text{B.0.2})$$

The matter power spectrum $P_{\text{cdm}}(k)$ today ($z = 0$) can be calculated using

$$P_{\text{cdm}}(k) = Ak^{n_s} T^2(k), \quad (\text{B.0.3})$$

where the power spectrum amplitude (A) is given by Bunn and White (1997)

$$A = 2\pi^2 \delta_H^2 \left(\frac{c}{H_0} \right)^{3+n_s}. \quad (\text{B.0.4})$$

The density perturbation at horizon crossing, δ_H , is related to the inflationary amplitude of scalar perturbations and is given by

$$\delta_H = 1.94 \times 10^{-5} \Omega_0^{(-0.785 - 0.05 \ln \Omega_0)} e^{-0.95(n_s - 1) - 0.169(n_s - 1)^2}. \quad (\text{B.0.5})$$

The transfer function describes the process of initial fluctuations and is found using a fitting formula in (Eisenstein and Hu, 1988). It can be written as a sum of the baryon and cold dark matter contributions at the drag epoch

$$T(k) = \frac{\Omega_b}{\Omega_0} T_b(k) + \frac{\Omega_c}{\Omega_0} T_c(k). \quad (\text{B.0.6})$$

The transfer function can be solved analytically for both large and small scales. The horizon at matter-radiation equality and the sound horizon at the drag epoch define the transition between these two extreme scales. The fitting formula for the transfer function therefore needs to approximate the full transfer function at all scales because structure formation is studied at scales that lie within the transition region.

In the absence of cold dark matter, the transfer function resembles a series of declining peaks as a result of acoustic oscillations. These peaks can be written as a product including a declining oscillatory term and an exponential Silk damping term giving the overall baryonic transfer function as

$$T_b(k) = \left[\frac{\tilde{T}_0(k, 1, 1)}{1 + (ks/5.2)^2} + \frac{\alpha_b}{1 + (\beta_b/ks)^3} e^{-(k/k_{\text{Silk}})^{1.4}} \right] j_0(k\tilde{s}), \quad (\text{B.0.7})$$

where the spherical Bessel function $j_0(k\tilde{s}) = (\sin x)/x$ approaches unity above the sound horizon and oscillates below it. Other terms in the equation are defined as

$$k_{\text{Silk}} = 1.6(\Omega_0 h^2)^{0.52}(\Omega_0 h^2)^{0.73}[1 + (10.4\Omega_0 h^2) - 0.95] \text{ Mpc}^{-1}, \quad (\text{B.0.8})$$

$$\beta_b = 0.5 + \frac{\Omega_b}{\Omega_0} + \left(3 - 2\frac{\Omega_b}{\Omega_0}\right) \sqrt{(17.2\Omega_0 h^2)^2 + 1}, \quad (\text{B.0.9})$$

$$\tilde{s}(k) = \frac{s}{[1 + (\beta_{\text{node}}/ks)^3]^{1/3}}, \quad (\text{B.0.10})$$

$$\beta_{\text{node}} = 8.41(\Omega_0 h^2)^{0.435}. \quad (\text{B.0.11})$$

The sound horizon is defined as the distance a wave can travel prior to the drag epoch (z_d)

$$s = \frac{2}{3k_{\text{eq}}} \sqrt{\frac{6}{R_{\text{eq}}}} \ln \frac{\sqrt{1 + R_d} + \sqrt{R_d + R_{\text{eq}}}}{1 + \sqrt{R_{\text{eq}}}} \text{ Mpc}. \quad (\text{B.0.12})$$

The ratio of baryon to photon momentum density is given by

$$R = 31.5 \times 10^3 \Omega_b h^2 \Theta_{2.7}^{-4} (1 + z)^{-1}, \quad (\text{B.0.13})$$

so we have that $R_{\text{eq}} = R(z_{\text{eq}})$ and $R_d = R(z_d)$ are the values of R at the matter-radiation and drag epoch. The redshifts of these two epochs are

$$z_{\text{eq}} = 2.5 \times 10^4 \Omega_0 h^2 \Theta_{2.7}^{-4}, \quad (\text{B.0.14})$$

$$z_d = 1291 \frac{(\Omega_0 h^2)^{0.251}}{1 + 0.659(\Omega_0 h^2)^{0.828}} [1 + b_1(\Omega_b h^2)^{b_2}], \quad (\text{B.0.15})$$

where

$$b_1 = 0.313(\Omega_0 h^2)^{-0.419} [1 + 0.607(\Omega_0 h^2)^{0.974}],$$

$$b_2 = 0.238(\Omega_0 h^2)^{0.223}.$$

The scale of the particle horizon (k_{eq}) at matter-radiation equality is

$$k_{\text{eq}} = 7.46 \times 10^{-2} \Omega_0 h^2 \Theta_{2.7}^{-2}. \quad (\text{B.0.16})$$

Finally,

$$\alpha_b = 2.07 k_{\text{eq}} s (1 + R_d)^{-3/4} G \left(\frac{1 + z_{\text{eq}}}{1 + z_d} \right), \quad (\text{B.0.17})$$

where

$$G(y) = y \left[-6\sqrt{1+y} + (2+3y) \ln \left(\frac{\sqrt{1+y}+1}{\sqrt{1+y}-1} \right) \right]. \quad (\text{B.0.18})$$

For cold dark matter we can write

$$T_c(k) = f \tilde{T}_0(k, 1, \beta_c) + (1-f) \tilde{T}_0(k, \alpha_c, \beta_c), \quad (\text{B.0.19})$$

where the functions used in the above equation are fit using the formulae

$$f = \frac{1}{1 + (ks/5.4)^4}, \quad (\text{B.0.20})$$

$$\tilde{T}_0(k, \alpha_c, \beta_c) = \frac{\ln(e + 1.8\beta_c q)}{\ln(e + 1.8\beta_c q) + Cq^2}, \quad (\text{B.0.21})$$

$$C = \frac{14.2}{\alpha_c} + \frac{386}{1 + 69.9q^{1.08}}, \quad (\text{B.0.22})$$

$$q = \frac{k}{13.41 k_{\text{eq}}}, \quad (\text{B.0.23})$$

$$\alpha_c = a_1^{-\Omega_b/\Omega_0} a_2^{-(\Omega_b/\Omega_0)^3}, \quad (\text{B.0.24})$$

$$a_1 = (46.9 \Omega_0 h^2)^{0.670} [1 + (32.1 \Omega_0 h^2)^{-0.532}],$$

$$a_2 = (12.0 \Omega_0 h^2)^{0.424} [1 + (45.0 \Omega_0 h^2)^{-0.582}],$$

$$\beta^{-1} = 1 + b_1 [(\Omega_c/\Omega_0)^{b_2} - 1], \quad (\text{B.0.25})$$

$$b_1 = 0.944 [1 + (458 \Omega_0 h^2)^{-0.708}]^{-1},$$

$$b_2 = (0.395 \Omega_0 h^2)^{-0.0266}.$$

A list of other variables and their corresponding values used in the above fit are shown in Table B.1.

Symbol	Value
Ω_0	0.27
Ω_Λ	$1 - \Omega_0$
Ω_k	0
$f_{\text{baryon}} = \frac{\Omega_b}{\Omega_0}$	0.16
h	0.71
T_{cmb}	2.728
$\Theta_{2.7}$	$T_{\text{cmb}}/2.7$
n_s	0.96
c	2.99×10^6
H_0	71
b	1

Table B.1: *List of variables and values taken used in above equations.*

Bibliography

- Abdalla, F. B., Blake, C., and Rawlings, S. (2009). Forecasts for dark energy measurements with future surveys. *MNRAS*, 401(2):743–758.
- Ansari, R., Campagne, J. E., Colom, P., Le Goff, J. M., Magneville, C., Martin, J. M., Moniez, M., Rich, J., and Yèche, C. (2011). 21 cm observation of lss at $z \sim 1$; instrument sensitivity and foreground subtraction. *arXiv:1108.1474*.
- Ansari, R., Le Goff, J.-M., Magneville, C., Moniez, M., Palanque-Delabrouille, N., J., R., Ruhlmann-Kleider, V., and Yèche, C. (2008). Reconstruction of hi power spectra with radio-interferometers to study dark energy. *arXiv:0807.3614*.
- Bandura, K., Addison, G. E., Amiri, M., Bond, J. R., and et. al. (2014). Canadian hydrogen intensity mapping experiment (chime) pathfinder. *arxiv:1406.2288*.
- Barkana, R. and Loeb, A. (2007). The physics and early history of the intergalactic medium. *Reports on Progress in Physics*, 70(4):627–657.
- Battye, R. A., Browne, I. W. A., Dickinson, C., and et. al. (2013). Hi intensity mapping: a single dish approach. *MNRAS*, 434:1239–1256.
- Battye, R. A., Davies, R. D., and Weller, J. (2004). Neutral hydrogen surveys for high-redshift galaxy clusters and protoclusters. *MNRAS*, 355:1339–1347.

- Bennett, C. L., Larson, D., Wieland, J. L., Jorosik, N., and et. al. (2013). Nine-year wilkinson microwave anisotropy probe (wmap) observations: Final maps and results. *ApJ*, 208.
- Bondi, M., Ciliegi, P., Zamorani, G., Gregorini, L., and et. al. (2003). The vla-vmos deep field i. radio observations probing the microjy source population. *A&A*.
- Bunn, E. F. and White, M. (1997). The 4 year coBE normalization and large-scale structure. *ApJ*, 480.
- Caldwell, R. R., Dave, R., and Steinhardt, P. J. (1998). Cosmological imprint of an energy component with general equation of state. *Phys. Rev. Lett.*, 80(8):1582–1585.
- Carroll, S. M. and Press, W. H. (1992). The cosmological constant. *Annu. Rev. Astron. Astrophys.*, 30:499–542.
- Chang, T.-C., Pen, U.-L., Bandura, K., and Peterson, J. B. (2010). An intensity map of hydrogen 21-cm emissions at redshift $z \approx 0.8$. *Nature*, 466.
- Chang, T.-C., Pen, U.-L., Peterson, J. B., and McDonald, P. (2008). Baryon acoustic oscillation intensity mapping as a test of dark energy. *Phys. Rev. Lett.*, 100:091303.
- Chapman, E., Abdalla, F. B., Bobin, J., Starck, J.-L., Harker, G., and et. al. (2013). The scale of the problem: recovering images of images of reionization with generalized morphological component analysis. *MNRAS*, 429:165–176.
- Chapman, E., Abdalla, F. B., Harker, G., Jelić, V., and et. al. (2012). Foreground removal using fastica: a showcase of lofar-eor. *MNRAS*, 423:2518–2532.

- Chen, X. (2012). The tianlai project: A 21 cm cosmology experiment. *International Journal of Modern Physics: Conference Series*, 12:256–263.
- Cho, J., Lazarian, A., and Timbie, P. T. (2012). A technique for foreground subtraction in redshifted 21 cm observations. *ApJ*, 749.
- Cole, S., Percival, W. J., Peacock, J. A., Norberg, P., and et. al. (2005). The 2df galaxy redshift survey: power-spectrum analysis of the final dataset and cosmological implications. *MNRAS*, 362:505–534.
- Delabrouille, J., Betoule, M., Melin, J.-B., and et. al. (2012). The pre-launch planck sky model: a model of sky emission at submillimetre to centimetre wavelengths. *Astronomy and Astrophysics*.
- Di Matteo, T., Ciardi, B., and Miniati, F. (2004). The 21 cm emission from the reionization epoch: extended and point source foregrounds. *MNRAS*, 355:1053–1065.
- Dickinson, C. (2012). Cmb interferometry. *arXiv:1212.1729*.
- Eisenstein, D. J. and Hu, W. (1988). Baryonic features in the matter transfer function. *ApJ*, 496:605.
- Eisenstein, D. J., Seo, H.-J., and White, M. (2007). On the robustness of the acoustic scale in the low-redshift clustering of matter. *ApJ*, 664:660–674.
- Eisenstein, D. J., Zehavi, I., Hogg, D. W., and et. al. (2005). Detection of the baryon acoustic peak in the large-scale correlation function of sdss luminous red galaxies. *ApJ*, 633:560–574.
- Emerson, D. (2002). Why single dish? *Single-Dish Radio Astronomy: Techniques and Applications, ASP Conference Proceedings*, 278:27–43.

- Ferreira, P. G. and Joyce, M. (1998). Cosmology with primordial scaling field. *Phys. Rev. D*, 58(2).
- Fomalont, E. B., Kellermann, K. I., Partridge, R. B., Windhorst, R. A., and Richards, E. A. (2002). The microjansky sky at 8.4 ghz. *The Astronomical Journal*, 123:2402–2416.
- Frieman, J., Turner, M., and Huterer, D. (2008). Dark energy and the accelerating universe. *Ann. Rev. Astron. Astrophys*, 46:385–432.
- Gaensler, B. M., Dickey, J. M., McClure-Griffiths, N. M., and et. al. (2001). Radio polarization from the inner galaxy at arcminute resolution. *ApJ*, 549(2):959–978.
- Gawiser, E. and Silk, J. (2000). The cosmic microwave background radiation. *Phys. Rept.*, 333:245–267.
- Gervasi, M., Tartari, A., Zannoni, M., Boella, G., and Sironi, G. (2008). The contribution of the unresolved extragalactic radio sources to the brightness temperature of the sky. *ApJ*, 682:223–230.
- Giardino, G., Banday, A. J., Górski, K. M., Bennett, K., Jonas, J. L., and Tauber, J. (2002). Towards a model of full-sky galactic synchrotron intensity and linear polarisation: a re-analysis of the parkes data. *Astronomy & Astrophysics*.
- Górski, K. M., Hivon, E., Banday, A. J., and et. al. (2005). Healpix: A framework for high-resolution discretization and fast analysis of data distributed on the sphere. *ApJ*, 622:759–771.
- Gu, J., Xu, H., Wang, J., An, T., and Chen, W. (2013). The application of continuous wavelet transform based foreground subtraction method in 21 cm sky surveys. *ApJ*, 773.

- Hamilton, J.-C., R., C., and an et. al., C. C. (2008). Sensitivity of a bolometric interferometer to the cmb power spectrum. *A&A*, 491:923–927.
- Harker, G., Zaroubi, S., Bernardi, G., Brentjens, M. A., and et. al. (2009). Non-parametric foreground subtraction for 21-cm epoch of reionization experiments. *MNRAS*, 397:1138–1152.
- Haslam, C. G. T., Salter, C. J., Stoffel, H., and Wilson, W. E. (1982). The 408 mhz all-sky survey. *A & A*, 500(1):245–246.
- Hicken, M., Wood-Vasey, W. M., Blondin, S., Challis, P., Jha, S., Kelly, P. L., Rest, A., and Kirshner, R. P. (2009). Improved dark energy constraints from 100 new cfa supernova type 1a light curves. *ApJ*, 700:1097–1140.
- Hobson, M. P., Lasenby, A. N., and Jones, M. (1995). A baysian method for analysing interferometer observations of cosmic microwave background fluctuations. *Mon. Not. R. Astron. Soc.*, 275(863).
- Hopkins, A. M., Afonso, J., Chan, B., Cram, L. E., and et. al. (2003). The phoenix deep survey: The 1.4ghz microjansky catalog. *The Astronomical Journal*, 125:465–477.
- Huetsi, G. (2006). Acoustic oscillations in the sdss dr4 luminous red galaxy sample power spectrum. *A&A*, 449:891–902.
- Huterer, D. and Turner, M. S. (1999). Prospects for probing the dark energy via supernova distance measurements. *Phys. Rev. D*60.
- Katgert, P., Oort, M. J. A., and Windhorst, R. A. (1988). The wrst 1.4 ghz amalgamated source counts. *A&A*, 195:21–24.

- Kowalski, M., Rubin, D., Aldering, G., Agostinho, R. J., and et al. (2008). Improved cosmological constraints from new, old and combined supernova data sets. *ApJ*, 686:749–778.
- Landon, J., Elmer, M., Waldron, J., Jones, D., and et. al. (2009). Phased array feed calibration, beamforming and imaging. *The Astronomical Journal*, 139.
- Liu, A. and Tegmark, M. (2011). A method for 21 cm power spectrum estimation in the presence of foregrounds. *arXiv:1103.0281v2*.
- Loeb, A. and Wyithe, J. S. B. (2008). Possibility of precise measurement of the cosmological power spectrum with a dedicated 21cm survey after reionization. *Phys. Rev. Lett.*, 100:161301.
- Mao, X.-C. (2012). Subtracting foregrounds from interferometric measurements of the redshifted 21 cm emission. *ApJ*, 744.
- Masui, K. W., Switzer, E. R., Banavar, N., Bandura, K., and et. al. (2013). Measurement of 21cm brightness fluctuations at $z \sim 0.8$ in cross-correlation. *Astrophysical Journal Letters*, 763.
- McQuinn, M., Zahn, O., Zaldarriaga, M., Hernquist, L., and Furlanetto, S. R. (2006). Cosmological parameter estimation using 21 cm radiation from the epoch of reionization. *arXiv:astro-ph/0512263v3*.
- Miville-Deschênes, M.-A., Lagache, G., Boulanger, F., and Puget, J.-L. (2007). Statistical properties of dust far-infrared emission. *A&A*, 469:595–605.
- Obreschkow, D., Klöckner, H.-R., Heywood, I., Levrier, F., and Rawlings, S. (2009). A virtual sky with extragalactic hi and co lines for the ska and alma. *ApJ*, 703:1890–1903.

- Oztas, A. M. and Smith, M. L. (2006). A model of light from ancient blue emissions. *International Journal of Theoretical Physics*, 45(5):908–923.
- Perlmutter, S. (2003). Supernovae, dark energy, and the accelerating universe. *Physics Today*, 53.
- Perlmutter, S., Aldering, G., Goldhaber, G., and et. al. (1999). Measurements of ω and λ from 42 high-redshift supernovae. *The Astrophysical Journal*, 517:565.
- Peterson, J. B., Bandura, K., and Pen, U. L. (2006). The hubble sphere hydrogen survey. *arXiv:astro-ph/0606104*.
- Prandoni, I., Parma, P., Wieringa, M. H. de Ruiter, H. R., and et. al. (2006). The atesp 5 ghz radio survey. i. source counts and spectral index properties of the faint radio population. *A&A*, 457(2).
- Pritchard, J. R. and Loeb, A. (2008). Evolution of the 21cm signal throughout cosmic history. *Physical Review D*, 78(10).
- Pritchard, J. R. and Loeb, A. (2011). 21-cm cosmology. *arXiv:1109.6012*.
- Riess, A. G., Filippenko, A. V., Challis, P., and et. al. (1998). Observational evidence from supernovae for an accelerating universe and a cosmological constant. *The Astronomical Journal*, 116.
- Santos, M. G., Cooray, A., and Knox, L. (2005). Multifrequency analysis of 21 centimetre fluctuations from the era of reionization. *ApJ*, 625:575–587.
- Scott, D., Srednicki, M., and White, M. (1994). Sample variance in small scale cosmic microwave background anisotropy experiments. *ApJ*, 421:L5–L7.

- Seo, H.-J., Dodleson, S., Marriner, J., McGinnis, D., Stebbins, A., Stoughton, C., and Vallinotto, A. (2010). A ground-based 21-cm baryon acoustic oscillation survey. *ApJ*, 721(1):64.
- Steinhardt, P. J., Wang, L., and Zlatev, I. (1999). Cosmological tracking solutions. *Phys. Rev. D*, 59(12).
- Switzer, E. R., Masui, K. W., Bandura, K., and et. al. (2013). Determination of $z \sim 0.8$ neutral hydrogen fluctuations using the 21 cm intensity mapping auto-correlation. *arXiv:1304.3712*.
- Thompson, A. R., Moran, J. M., and Swenson, G. W. (1986). Interferometry and synthesis in radio astronomy. *New York: Wiley*.
- Trott, C. M., Wayth, R. B., and Tingay, S. J. (2012). the impact of point source subtraction residuals on 21 cm epoch of reionization estimation. *arXiv:1208.0646v1*.
- Turner, M. S. and Huterer, D. (2007). Cosmic acceleration, dark energy, and fundamental physics. *J. Phys. Soc. Jpn.*, 76.
- Vernstrom, T., Scott, D., and Wall, J. V. (2011). Contribution to the diffuse radio background from extragalactic radio sources. *MNRAS*, 415:3641–3648.
- Vikhlinin, A., Kravtsov, A. V., Burenin, R. A., Ebeling, H., and et al. (2009). Chandra cluster cosmology project iii: Cosmological parameter constraints. *ApJ*, 629(2):1060–1074.
- Wang, J., Xu, H., Gu, J., An, T., Cui, H., and et. al. (2010). How to identify and separate bright galaxy cluster from the low-frequency radio sky? *arXiv:1008.3391v1*.

- Wang, X., Tegmark, M., Santos, M. G., and Knox, L. (2006). 21 cm tomography with foregrounds. *ApJ*, 650:529–537.
- Wetterich, C. (1988). Cosmology and the fate of dilation symmetry. *Nuclear Physics B*, 302(4):668–696.
- White, M., Carlstrom, J., Dragovan, M., and Hoolzapfel, W. (1998). Interferometric observation of cmb background anisotropies. *ApJ*, 514:12–24.
- Wolz, L., Abdalla, F. B., Blake, C., Shaw, J. R., and et. al. (2013). The effect of foreground subtraction on cosmological measurements from intensity mapping. *arXiv:1310.8144*.
- Wyithe, J. S. B., Loeb, A., and Geil, P. M. (2007). Baryonic acoustic oscillations in 21cm emission: a probe of dark energy out to high redshifts. *arXiv:0709.2955*.
- Zaldarriaga, M., Furlanetto, S. R., and Hernquist, L. (2004). 21 centimetre fluctuations from cosmic gas at high redshifts. *ApJ*, 608:622–635.